ROBUST RECEIVER DESIGN FOR RF COMMUNICATION AND UNDERWATER ACOUSTIC COMMUNICATION

A Dissertation presented to

the Faculty of the Graduate School

University of Missouri

In Partial Fulfillment

Of the Requirements for the Degree

Doctor of Philosophy

---

by

JUN TAO

Dr. Chengshan Xiao, Dissertation Supervisor

JULY 2010

The undersigned, appointed by the Dean of the Graduate School, have examined the dissertation entitled:

ROBUST RECEIVER DESIGN FOR RF COMMUNICATION AND UNDERWATER ACOUSTIC COMMUNICATION

presented by Jun Tao

a candidate for the degree of Doctor of Philosophy

and hereby certify that in their opinion it is worthy of acceptance.

Dr. Chengshan Xiao

Dr. Dominic K. C. Ho

Dr. Zhihai He

Dr. Wenjun Zeng

To my mother, Xiufeng Gao, and to my father, Buchao Tao.

ACKNOWLEDGMENTS

I would like to acknowledge all the people who have been important to this dissertation work here and now.

First of all, I am in great debt to my advisor Dr. Chengshan Xiao, who has supported me in many ways during the past four years. He has introduced me to the wholly new area of underwater acoustic communication, has provided numerous valuable suggestions and discussions to make this dissertation possible, and has cultivated my capability of independent research. His great enthusiasm and meticulous attitude towards research, have inspired me to work for excellence.

I'm especially thankful to Dr. Jingxian Wu, who has been of great assistance on academic writing in the last few years. Our in depth discussions have inspired many interesting ideas in several research topics.

I would also thank Dr. Yahong Rosa Zheng for helping on academic writing, and for providing me the chance to give presentations during my stay at the Missouri University of Science and Technology.

I would extend my gratitude to my dissertation committee members, Dr. Dominic Ho, Dr. Zhihai He, and Dr. Wenjun Zeng, for spending their valuable time serving in my dissertation committee, and for providing constructive suggestions and insightful criticisms to help improve the quality of the dissertation.

I'm grateful to Dr. Christian Sgraja of Qualcomm CDMA Technologies GmbH, Germany. Our work together has helped me to have a better understanding of "discrete-time channel modeling".

I would also acknowledge Dr. T. C. Yang of Naval Research Laboratory and Dr. Wen-Bin Yang of National Institute of Standards and Technology, for their valuable comments and suggestions on my research work on underwater acoustic communications. The teams from Office of Naval Research and Woods Hole Oceanographic Institution (WHOI) also

deserve my gratitude for conducting the underwater experiments and providing valuable field trial data, which greatly help my research on underwater acoustic communications.

Mr. Michael Lee Walker, who I got to know through Dr. Jingxian Wu, has worked closely with me on "turbo equalization". The curiosity we share have spawned many interesting discussions.

An important source of inspiration has been the Communication and Signal Processing Lab at the University of Missouri. I would like to thank my labmates: Mr. Le Yang, Mr. Ming Sun, Mr. Zhenghua Ma, Dr. Luis M. Vicente, Dr. Xiaoning Lu, for their help in different ways and their priceless friendship. I would also like to thank all other friends at Columbia, Missouri, who have enriched my life on the greater scale. I would also acknowledge the support from my group members at the Missouri University of Science and Technology: Mr. Jian Zhang, Ms. Tiange Shao, Mr. Fei Ren, Mr. Huang Lou, Mr. Weiliang Zeng, Mr. Mingxi Wang, Mr. Longbao Wang, Mr. Zengli Yang, Mr. Tuo Zhao, Mr. Amirhossein Rafati, Mr. Kajbaf Hamed and Ms. Chaitri Aroskar.

Last, but certainly not the least, my utmost gratitude goes to my family for their support and sacrifice.

TABLE OF CONTENTS

ACKNOWLEDGEMENTS ii

LIST OF TABLES viii

LIST OF FIGURES x

ABSTRACT xiii

CHAPTER

1 Introduction 1

1.1 Background 1

1.2 Objective 2

1.2.1 Design Goals for Wireless RF Communication 2

1.2.2 Design Goals for Wireless UWA Communication 3

1.3 Outline 4

2 On Discrete-Time Modeling of Time-Varying WSSUS Fading Channels 7

2.1 Introduction 7

2.2 Serial Concatenation of Linear Time-Varying Systems 8

2.3 Discrete-Time Modeling of Linear Time-Varying WSSUS Channels 10

2.4 Numerical Simulations 14

2.5 Conclusion 19

3 Doppler Spread Estimation for Wireless OFDM Systems **20**

3.1 Introduction 20

3.2 System Model and Assumptions 22

3.3 Algorithm Development Based on Time-Domain Signal Statistics 25

3.3.1 Statistics of Received Signals 25

3.3.2 Doppler Spread Estimation 29

3.4 A Practical Doppler Estimation Algorithm 31

3.5 Simulation 33

3.6 Conclusion 37

4 Channel Estimation for OFDM Systems with CFO and Phase Noise **39**

4.1 Introduction 39

4.2 System Model 42

4.3 Development of Estimation Algorithm 44

4.3.1 CFO Estimation in The Presence of Fading and Phase Noise 44

4.3.2 Joint Phase Noise and CTF Estimation 47

4.4 CRLB for OFDM Channel Estimation 50

4.5 Simulation 51

4.6 Conclusion 56

5 Enhanced MIMO LMMSE Turbo Equalization **58**

5.1 Introduction 58

5.2 Conventional MIMO LMMSE Turbo Equalization 60

5.3 Enhanced MIMO LMMSE Turbo Equalization 64

5.3.1 SIC Using *a posteriori* Soft Decisions 64

5.3.2 Reliability-based Detection Ordering 66

5.3.3 Low-Complexity Enhanced MIMO LMMSE Turbo Equalization . . 67

5.4 Simulation Results 68

5.5 Conclusion 70

6 MIMO Turbo Block Decision Feedback Equalization 71

6.1 Introduction . . . 71

6.2 System Description . . . 73

6.3 MIMO Turbo BDFE with Reliability-based SSIC . . . 76

6.3.1 Reliability-based SSIC . . . 76

6.3.2 Calculation of $\mathbf{C}_g$ and $\mathbf{D}_g$ . . . 80

6.3.3 Calculation of Extrinsic LLR Based on Equalized Symbols . . . 81

6.4 Low Complexity MIMO Turbo BDFE . . . 82

6.4.1 Complexity Comparison with MIMO Turbo LE . . . 84

6.5 Simulation Results . . . 86

6.6 Conclusion . . . 91

7 Channel Equalization for MIMO Underwater Acoustic Communications 92

7.1 Introduction . . . 92

7.2 MIMO UWA System Model . . . 95

7.3 Channel Estimation for MIMO UWA Communications . . . 96

7.4 New Equalization Scheme for MIMO UWA Communication . . . 98

7.4.1 MIMO Equalization for Space-Time Interference Cancelation . . . 98

7.4.2 Group-wise Phase Estimation and Compensation . . . 101

7.4.3 Layered Space-Time Processing . . . 102

7.5 Experimental Results . . . 104

7.5.1 Results of Makai05 Experiment . . . 104

7.5.2 Results of Unet06 Experiment . . . 112

7.6 Conclusion . . . 118

8 Turbo Detection for MIMO Underwater Acoustic Communications 119

8.1 Introduction . . . 119

8.2 Transmitter Design and Data Structure . . . 121

8.3 MIMO Receiver Architecture . . . 122

8.4 Experimental Results 124
8.4.1 Results of SPACE08 Experiment 124
8.4.2 Results of GOMEX08 Experiment 130
8.4.3 Comparison with Existing Approach 131
8.4.4 Complexity Discussion 133
8.5 Conclusion 135

9 Conclusion **136**
9.1 Contribution 136
9.2 Future Works 138

APPENDIX **139**

A Proof of (3.8) **and** (3.9) **139**

B Calculation of MIMO LE Matrix **140**

BIBLIOGRAPHY **142**

VITA **152**

LIST OF TABLES

Table **page**

2.1 Normalized Doppler spread: $\hat{B}_d$ 16

6.1 Low-complexity MIMO turbo BDFE algorithm 85

7.1 BER of LB 2×8 MIMO with BPSK modulation 113

7.2 BER of LB 2×8 MIMO with QPSK modulation 113

7.3 BER of LB 2×8 MIMO with 8PSK modulation 113

7.4 BER of HB 2×8 MIMO with BPSK modulation 113

7.5 Doppler shift estimation in moving-source transmission (Hz) 115

7.6 Average uncoded BER for Unet06 experiment 117

8.1 Description on hydrophone arrays 125

8.2 Results of 2×12 MIMO (200 m) 128

8.3 Results of 2×12 MIMO (1000 m) 129

8.4 BER of 2×12 MIMO (1000 m, 16QAM) 129

8.5 BER of 3×12 MIMO (1000 m, QPSK) 129

8.6 BER of 4×12 MIMO (1000 m, QPSK) 130

8.7 BER of 2×12 MIMO with horizontal hydrophone array (60 m, QPSK) . . 130

8.8 Num. of iter. for achieving zero BER (2×8, QPSK, packet size = 2048) . 132

8.9 Num. of iter. for achieving zero BER (2×8, QPSK, packet size = 4096) . 132

8.10 Results for 2×6 and 2×4 MIMO (200 m, QPSK) 134

8.11 Results for 2×6 MIMO (1000 m, QPSK) 134
8.12 BER of 4×6 MIMO (1000 m, QPSK) 134

LIST OF FIGURES

Figure **page**

2.1 Serial concatenation of two LTV systems. 8

2.2 Transmission model. 10

2.3 Approximated and actual autocorrelations: $l_1 = 1, l_2 = 0$ 16

2.4 Normalized absolute error of autocorrelation: $l_1 = 1, l_2 = 0$ 17

2.5 Mean and STD of normalized absolute error: $l_1 = 1, l_2 = 0$ 18

2.6 Mean and STD of normalized absolute error: $l_1 = 0, l_2 = 0$ 18

3.1 OFDM system model (only $y^{(i)}(n)$ is used during Doppler estimation). . . 22

3.2 Doppler spread estimation (Rayleigh fading, 64QAM modulation). 34

3.3 Doppler spread estimation (Rayleigh fading, 8PSK modulation). 35

3.4 STD v.s. number of frames (Rayleigh fading, 64QAM modulation). 36

3.5 Doppler spread estimation (Rician fading, 64QAM modulation). 37

3.6 Standard deviation v.s. Rice factor K (8PSK modulation). 38

4.1 CFO estimation error ($\epsilon_0 \in (-1, 1), z \in [-14, 14]$, QPSK). 52

4.2 Average $|\Delta\epsilon|$ versus SNR ($\epsilon_0 \in (-1, 1), z \in [-14, 14]$, QPSK). 53

4.3 CTF estimation MSE versus SNR (QPSK, $\epsilon_0 \in (-1, 1), z = 0$). 55

4.4 CIR estimation MSE versus SNR (QPSK, $\epsilon_0 \in (-1, 1), z = 0$). 55

4.5 CIR estimation MSE versus SNR (QPSK, $\epsilon_0 \in (-1, 1), z \in [-4, 4]$). 56

4.6 BER versus SNR ($\epsilon_0 \in (-1, 1), z = 0$, QPSK). 57

5.1 A MIMO transmission system 60
5.2 Tapped delay line structure for MIMO equalization 62
5.3 Enhanced MIMO LMMSE turbo equalizer structure. 64
5.4 BER comparison between conventional and proposed equalization schemes 69
5.5 BER performance of the low-complexity turbo equalization 69

6.1 A MIMO communication system with turbo detection. 74
6.2 Soft-decision MIMO BDFE (when $x_{\langle O_g \rangle}$ is equalized). 79
6.3 BER comparison between fixed and reliability-based SSIC (complex channel) 88
6.4 BER comparison between fixed and reliability-based SSIC (real channel) . 88
6.5 2×2 MIMO: BER comparison for LE and BDFE (8PSK) 89
6.6 BER comparison among LE, BDFE and MAP equalization (BPSK) 90

7.1 Layered MIMO receiver architecture adopting the proposed equalization. . 103
7.2 Signalling at the transmitter in Makai05 experiment. 105
7.3 MIMO packet structure in Makai05 experiment. 105
7.4 An example of normalized LFM correlation. 106
7.5 Estimated channel impulse responses for 2×8 MIMO with BPSK modulation. 107
7.6 Estimated channel impulse responses for 2×8 MIMO with QPSK modulation. 108
7.7 Partition of the transmitted data payload for block detection at the receiver. 109
7.8 Demonstration of channel variation within one packet. 110
7.9 Received baseband signal, equalized and phase-corrected BPSK symbols . . 111
7.10 Equalized and phase-corrected QPSK and 8PSK symbols 112
7.11 SIMO packet structure in Unet06 experiment. 114
7.12 Channel scattering functions. 115
7.13 Partition of the transmitted data payload for block detection at the receiver. 116
7.14 Equalized QPSK symbols using eight channels in Unet06 experiment. . . . 116
7.15 Phase-corrected QPSK symbols using eight channels in Unet06 experiment. 116

8.1 Transmit signalling for the n-th transducer. 121
8.2 The burst structure of the n-th transmit branch in SPACE08 experiment. . 121
8.3 MIMO receiver using turbo BDFE. 123
8.4 The partition structure of the transmitted data payload. 124
8.5 An example of received passband signal. 126
8.6 Power spectrum density of received signal. 126
8.7 LFM correlation example. 127
8.8 Estimated channel. 127
8.9 Demonstration of turbo equalization over iterations (8PSK modulation) . . 127
8.10 Demonstration of turbo equalization over iterations (16QAM modulation) . 127
8.11 Estimated channel impulse responses for GOMEX08 experiment. 131
8.12 Simulation result comparison. 133
8.13 Experimental result comparison 133

ROBUST RECEIVER DESIGN FOR RF COMMUNICATION AND UNDERWATER ACOUSTIC COMMUNICATION

Jun Tao

Dr. Chengshan Xiao, Dissertation Supervisor

ABSTRACT

This dissertation includes two parts: robust receiver design for wireless radio frequency (RF) communication, and robust receiver design for underwater acoustic (UWA) communication. In the first part, four aspects including fading channel modeling, Doppler spread estimation, channel estimation, and (turbo) equalization, are investigated for a common digital receiver. The general methodology of study is theoretical analysis and numerical simulation. In the second part, different receiver designs are proposed for underwater acoustic communication, with their robustness tested by experimental data collected at several undersea field trials.

An equivalent discrete-time channel model is the basis for robust receiver design in any digital communication system. The work on channel modeling highlights the loss of *separability property* of the discrete-time channel scattering function, a result that is commonly overlooked. The conditions for the validity of the separability property is provided, under which efficient channel simulators can be used.

Doppler spread contains information about fading channels, thus is an important system parameter guiding robust receive design. A Doppler spread estimation algorithm is proposed, for the prevailing orthogonal frequency division multiplexing (OFDM) systems undergoing Rayleigh or Rician fading. The estimator belongs to the class of "method of moment", and it estimates the Doppler spread with the auto-covariance function of the received signal power.

Channel estimation is critical for equalization and detection. A pilot-aided channel estimation algorithm is presented for OFDM systems with non-ideal effects including both carrier frequency offset (CFO) and phase noise. It estimates and compensates the CFO first, and then performs joint channel estimation and phase noise suppression with the maximum *a posteriori* (MAP) criterion. The CFO compensation and phase noise suppression improves the channel estimation accuracy.

The work on equalization focuses on turbo (iterative) equalization, and discusses two turbo equalization schemes for multiple-input, multiple-output (MIMO) systems. The first scheme enhances existing linear minimum mean square error (LMMSE) turbo equalizer, by utilizing not only the *a priori* information at the input of the equalizer but also the *a posteriori* information obtained when the equalization progresses. With the new equalization mechanism, the detection ordering matters as to the equalization performance, and has been exploited to further enhance the detection performance. The second scheme develops a non-linear block decision-feedback equalizer (BDFE) with *reliability-based* successive soft interference cancelation (SSIC). The symbol reliability information is calculated directly with the *a priori* input, incurring minimum extra cost.

UWA communication is much more challenging than RF communication due to its limited available bandwidth, long delay spread, fast temporal variation and significant Doppler effect. Signal detection under such scenarios, is thus very difficult. The remaining part of the dissertation discusses robust receiver design for UWA communication. Two design schemes have been proposed. The first scheme adopts MIMO linear equalizer (LE) working with a group-wise phase compensator. It was tested with experimental data collected at Kauai, Hawaii, in September 2005, and Saint Margarets Bay, Nova Scotia, Canada, in May 2006. Experimental results shew that it was robust under different communication environments. The second scheme adopts the developed MIMO turbo BDFE mentioned above, with its robustness and performance tested by experimental data collected at the coast of Martha's Vineyard, Edgartown, MA, in October 2008, and Gulf of Mexico in July 2008, respectively.

Chapter 1

Introduction

1.1 Background

Future wireless communication applications feature high transmission rate, high spectral efficiency and high mobility, which can be achieved with Multiple-Input Multiple-Output (MIMO) technology and Orthogonal Frequency Division Multiplexing (OFDM) technology. For instance, in the forthcoming Third Generation Partnership Project (3GPP) Long Term Evolution (LTE), downlink and uplink data rates are expected up to 300 mega bits per second (Mbps) and 75 Mbps with a bandwidth of 20 mega hertz (MHz), at speeds of 350 kilometers per hour (km/h) or even up to 500 km/h.

MIMO technology greatly improves channel capacity, which is proportional to the number of transmit antennas over a flat Rayleigh-fading channel. However, it also makes signal detection on the receiver side much more difficult than Single-Input Single-Output (SISO) systems, due to extra spatial interference among concurrent transmission streams. OFDM technology is advantageous in improving spectral efficiency and combating inter-symbol interference (ISI). It is, however, very sensitive to timing offset, carrier frequency offset (CFO), and phase noise, which destroy the orthogonality among subcarriers and cause inter-carrier interference (ICI). Furthermore, it leads to high peak to average ratio (PAR) imposing critical requirement on power amplifier. MIMO-OFDM technology is expected to be a good candidate for fourth-generation (4G) wireless communication, and is attracting vast research interests.

Parallel to the advance in wireless radio-frequency (RF) communication, underwater acoustic (UWA) communication also witnesses its rapid progress in the past decade. While coherent modulations had been believed infeasible in UWA communications until early 1990's, MIMO and OFDM technologies originating in RF communications, have been timely introduced to UWA communications. Compared to RF communication, UWA communication is much more challenging due to the harsh UWA channel conditions: first, the available channel bandwidth is very limited due to the frequency-dependent attenuation; second, the channel delay spread is excessively long due to the rich scattering environment; third, the Doppler effect is significantly large due to the low propagation speed of sound (about 1500 m/s in water); finally, the temporal variation of the UWA channel is very fast due to the dynamics of the water mass. As a result, deployment of new technologies in UWA communications is at the stage of field trial, and robust detection algorithms is still highly desirable before practical real-time hardware systems can be implemented.

1.2 Objective

Based on the background introduced above, this dissertation aims to study robust receiver designs for future wireless RF communication and wireless UWA communication. For wireless RF communication, the basic objective is to address open *physical-layer* challenges and develop new algorithms relating to robust signal detection. For wireless UWA communication, the main objective is to propose robust receiver structures incorporating new technologies, and test them with undersea trial data. The two objectives are elaborated in the following.

1.2.1 Design Goals for Wireless RF Communication

- The difficulty in communications is ultimately caused by the underlying *physical channel*, which distorts the transmitted signal in a random manner thus demands proper signal detection at the receiver side. Therefore, I have started with the topic of channel modeling for this dissertation work. The primary goal is to provide a

general methodology for discrete-time channel modeling of digital systems.

- For wireless mobile communications, the physical channel is modeled as Rayleigh or Rician fading processes, which are characterized by channel *scattering function*. In scattering function, *Doppler spread* is an important figure of merit, which contains information about channel *coherence time* and *mobile speed* thus directly assists receiver design. This dissertation aims to develop a Doppler spread estimator for mobile OFDM systems, under practical channel conditions.

- The third problem raised is channel estimation, which is critical for the success of signal detection. This work addresses robust channel estimation problem for OFDM systems in the presence of both carrier frequency offset and phase noise.

- The last topic deals with channel equalization, particularly, turbo equalization. The primary goal is to design low-complexity, high-performance iterative equalization algorithms targeting MIMO communication systems.

1.2.2 Design Goals for Wireless UWA Communication

- Due to the harsh condition of UWA channel, time-varying phase distortion is introduced for transmitted signals in addition to symbol interference. The equalized symbols produced by conventional equalizer, thus suffer undesirable phase rotation and can not be reliably detected in coherent systems. One of the goals in this part is therefore to propose robust receiver structure, which handles phase rotation and provides robust symbol detection. The designed receiver structure is expected to work robustly under different UWA environments.

- The advent of turbo decoding and turbo equalization technologies enables powerful receiver design, which via iterative operations, significantly outperforms conventional non-iterative receiver. The second goal in this part is to develop robust turbo receiver structure for UWA communications.

1.3 Outline

Chapter 2: In this chapter, an important issue on the modeling of equivalent discrete-time fading channel, is discussed. The equivalent discrete-time channel incorporating transmit filter, physical fading channel and receive filter, usually loses not only uncorrelated scattering (US) property but also separability property. The lost of separability property has commonly been overlooked in existing literature. This chapter provides theoretical analysis and numerical simulations on the conditions under which the separability property of the composite channel is approximately valid, so that efficient channel simulators can be used.

Chapter 3: In this chapter, a Doppler estimation algorithm for wireless mobile OFDM systems undergoing Rayleigh or Rician fading channel, is proposed. The new method estimates Doppler spread based on the autocovariance of received signal power, which is fundamentally different from existing Doppler estimations relying on either pilot symbols or special structure of OFDM symbol. It provides robust Doppler estimations over a large range of practical Doppler, even with very low signal-to-noise ratio (SNR). .

Chapter 4: In this chapter, channel estimation for OFDM systems in the presence of both CFO and phase noise is studied. The estimation is performed in two steps. In the first step, the CFO is estimated by utilizing time-frequency property of OFDM symbols. Both integer and fractional CFO are estimated. In the second step, the estimated CFO is compensated in the received signal before channel estimation starts. The channel estimation and phase noise suppression are jointly done with the maximum *a posteriori* (MAP) criterion. Simulations show that the designed channel estimator achieves near-CRLB performance.

Chapter 5: In this chapter, an enhanced linear minimum mean square error (LMMSE) turbo equalizer is proposed for MIMO systems with frequency-selective fading. Based on the fact that the *a posteriori* soft information at the output of the equalizer is more reliable than the *a priori* information at the input of the equalizer, the enhanced equalizer incorpo-

rates the *a posteriori* soft information into the soft interference cancelation (SIC) operation during each iteration of the turbo equalization. Specifically, once a symbol is equalized, the obtained *a posteriori* information updates its *a priori* information, so that those unequalized symbols will benefit from that updating. A *reliability-based* ordering scheme is also provided under the new equalization framework, so that the system performance can be further improved. The symbol reliability is measured by using the symbol *a priori* probability, which is a unique byproduct of turbo detection. Therefore, the reliability-based detection achieves extra performance gain with minimum overhead.

Chapter 6: In this chapter, a turbo block decision-feedback equalizer (BDFE) is proposed for MIMO systems. The designed MIMO BDFE performs successive soft interference cancelation (SSIC) on both inter-symbol interference (ISI) in the time domain and multiplexing interference (MI) in the space domain. As in Chapter 5, a *reliability-based* group-wise detection ordering scheme, is also proposed, to minimize the negative impacts of error propagation that plagues conventional successive interference cancellation systems. A low-complexity implementation of the proposed MIMO turbo BDFE is further proposed, which takes advantage of fast matrix inversion algorithms.

Chapter 7: In this chapter, a new equalization scheme for high-rate single carrier MIMO UWA channels, is discussed. Different from existing methods employing joint equalization and symbol-wise phase tracking technology, the proposed scheme decouples the interference-cancelation (IC) operation and the phase-compensation operation, leading to a generalized equalizer structure combining an IC equalizer with a phase compensator. The decoupling of the two functionalities guarantees robust signal detection, which is most desirable in practical UWA applications. MIMO linear equalizer (LE) is adopted to remove space-time interference, and a group-wise phase estimation and correction method is used to compensate the phase rotation. In addition, the layered space-time processing technology is adopted to enhance the equalization performance attributing to the space freedom in MIMO systems. The proposed equalization scheme is tested to be very robust with extensive experimental data collected at Kauai, Hawaii, in September 2005, and Saint

Margaret's Bay, Nova Scotia, Canada, in May 2006.

Chapter 8: The developed MIMO turbo BDFE in *Chapter 6* is tailored to enable a robust receiver design for high data rate single-carrier MIMO UWA communications. With inter-block interference (IBI) properly removed, the MIMO BDFE is performed with overlapped information blocks without guard intervals, thus a high transmission data efficiency is guaranteed and the performance degradation at the tail of each block is prevented. The MIMO channel is treated as time invariant over each small block, and is estimated either with pilot symbols in the training mode or with previously-detected symbols in the decision-directed (DD) mode. The proposed receiver scheme has been tested by extensive experimental data and proved to be robust in different transmission environments. The results for the SPACE08 experiment conducted near Martha's Vineyard and the GOMEX08 experiment conducted at the Gulf of Mexico, are both reported.

Chapter 9: The final chapter summarizes the contribution of this dissertation, and discusses the future works.

Chapter 2

On Discrete-Time Modeling of Time-Varying WSSUS Fading Channels

2.1 Introduction

Many mobile radio communication channels can be modeled as wide-sense stationary uncorrelated scattering (WSSUS) channels [1], [2], which are fully described by a two-dimensional Doppler-delay scattering function [3]. In rich scattering environments without line of sight, the uncorrelated paths are usually modeled as Rayleigh processes with a Doppler spectrum according to Clarke's two-dimensional isotropic scattering model [4]. For an efficient simulation of Clarke's reference model, various methods have been proposed in the literature, which are either based on filtered white noise or the sum-of-sinusoids principle (see [5–7] and the references therein).

Digital transmissions over linear time-varying (LTV) WSSUS channels may be compactly represented and efficiently simulated using a fully discrete-time channel model that integrates transmitter and receiver filtering together with the LTV channel into an equivalent discrete-time channel impulse response [8], [9]. However, this discrete-time analog normally loses the uncorrelated scattering property [8] while preserving the wide-sense stationary (WSS) property. For accuracy reasons, the path correlations should be taken into account in a simulation model, or when designing a channel estimator that relies on proper second-order statistics. Moreover, the scattering function of an LTV channel is usually

factorized into Doppler spectrum and power delay profile. Like the uncorrelated scattering (US) property, this separability property is also not preserved in the discrete-time model, as it is shown in this chapter.

We first consider the overall response of a serial concatenation of two general LTV systems and then precisely analyze the discrete-time model of a digital transmission over an LTV channel. We further demonstrate with both theoretical analysis and numerical simulations that the separability property is approximately preserved in most practical cases.

2.2 Serial Concatenation of Linear Time-Varying Systems

The serial concatenation of two LTV systems $a(t,\tau)$ and $b(t,\tau)$ is shown in Fig. 2.1, where $f(t,\tau)$ is the output of the system f at time t to a delta pulse at time $t-\tau$.

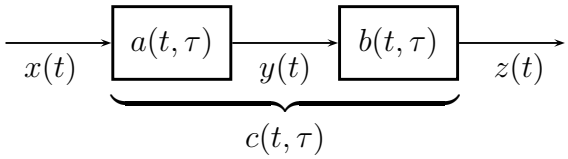

Figure 2.1: Serial concatenation of two LTV systems.

Let $c(t,\tau)$ be the response of the concatenation of $a(t,\tau)$ and $b(t,\tau)$, such that

$$z(t) = \int_{\tau} c(t,\tau)x(t-\tau)\,d\tau. \tag{2.1}$$

We also have

$$y(t) = \int_{\alpha} a(t,\alpha)x(t-\alpha)\,d\alpha, \tag{2.2}$$

$$z(t) = \int_{\beta} b(t,\beta)y(t-\beta)\,d\beta. \tag{2.3}$$

Combining (2.2), (2.3) and substituting $\alpha+\beta \rightarrow \tau$ gives

$$z(t) = \int_{\tau}\int_{\beta} b(t,\beta)a(t-\beta,\tau-\beta)\,d\beta\,x(t-\tau)\,d\tau. \tag{2.4}$$

By comparing (2.1) and (2.4), the response of the overall LTV system $c(t,\tau)$ comprising the two LTV systems $a(t,\tau)$ and $b(t,\tau)$, where $a(t,\tau)$ is followed by $b(t,\tau)$, is obtained as

$$c(t,\tau) \triangleq a(t,\tau) \circledast b(t,\tau) = \int_{\beta} b(t,\beta) a(t-\beta, \tau-\beta)\, d\beta. \tag{2.5}$$

In (2.5), we have introduced the directional convolution operator "$\circledast$" which denotes the serial concatenation of two LTV systems. In contrast to time-invariant systems, the order of arrangement matters if at least one of the systems a and b is time-varying. In such a case, the convolution "$\circledast$" is not commutative anymore, *i.e.*,

$$a(t,\tau) \circledast b(t,\tau) \neq b(t,\tau) \circledast a(t,\tau) \tag{2.6}$$

in general. To verify (2.6), we write down

$$c'(t,\tau) \triangleq b(t,\tau) \circledast a(t,\tau) = \int_{\beta'} a(t,\beta') b(t-\beta', \tau-\beta')\, d\beta'. \tag{2.7}$$

Substituting $\tau - \beta \to \beta'$ in (2.5) leads to

$$c(t,\tau) = \int_{\beta'} a(t-\tau+\beta', \beta') b(t, \tau-\beta')\, d\beta'. \tag{2.8}$$

By comparison, (2.8) and (2.7) differ in general.

In [10], the conception of "jointly underspread" of two LTV systems is introduced relying on the *delay-Doppler spreading function*, $S_g(\nu,\tau)$, of a LTV system $g(t,\tau)$, defined as

$$S_g(\nu,\tau) = \int_t g(t,\tau) e^{-j2\pi\nu t} dt. \tag{2.9}$$

The (absolute) moments $m_g^{(k,l)}$ of the spreading function is further defined as

$$m_g^{(k,l)} \triangleq \frac{1}{\|S_g\|_1} \int_\tau \int_\nu |\tau|^k |\nu|^l |S_g(\tau,\nu)| d\tau d\nu \tag{2.10}$$

where $k, l \in \mathcal{N}_0$, and the L_1-norm is given by $\|f\|_1 \triangleq \int \cdots \int |f(x_1, \cdots, x_n)| dx_1 \cdots dx_n$.

Approximation: The two LTV systems $a(t,\tau)$ and $b(t,\tau)$ are called "jointly underspread", when $m_a^{(0,1)} m_b^{(1,0)}$ and $m_a^{(1,0)} m_b^{(0,1)}$ are both small. Further, the two LTV systems are approximately commuting, i.e., $a(t,\tau) \circledast b(t,\tau) \approx b(t,\tau) \circledast a(t,\tau)$.

2.3 Discrete-Time Modeling of Linear Time-Varying WSSUS Channels

We now apply the previous findings to determine the correlation properties of an equivalent discrete-time channel model that complies with the transmission model shown in Fig. 2.2.

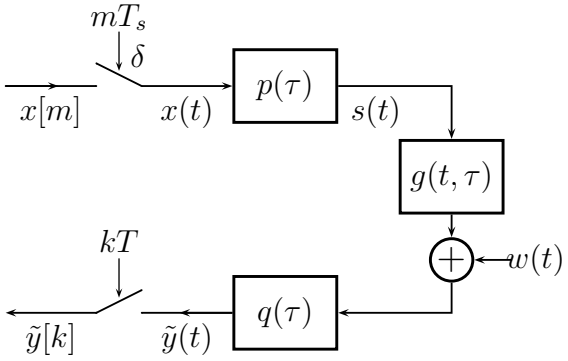

Figure 2.2: Transmission model.

Throughout this chapter we make use of the complex baseband equivalent notation. After weighting the data sequence $x[m]$ with the transmit pulse $p(\tau)$ periodically at a symbol rate of $1/T_s$, the resultant signal $s(t)$ is transmitted over the LTV physical channel $g(t,\tau)$ and white noise $w(t)$ is added. $g(t,\tau)$ is assumed to be a WSSUS Rayleigh fading channel according to Clarke's isotropic scattering model [4]. The autocorrelation R_{gg} of $g(t,\tau)$ is separable and given by

$$\begin{aligned} R_{gg}(t, t-\Delta t; \tau, \tau') &\triangleq \mathrm{E}\{g(t,\tau)g^*(t-\Delta t, \tau')\} \\ &= \psi(\Delta t) \cdot \phi(\tau)\delta(\tau - \tau') \end{aligned} \tag{2.11}$$

where $\psi(\Delta t) = J_0(2\pi B_d \Delta t)$ is the time correlation function for Clarke's model with B_d being the maximum Doppler spread of the channel. $\phi(\tau)$ denotes the power delay profile (PDP) with support T_g, i. e., $\phi(\tau) = 0$ for $\tau < 0$ and $\tau > T_g$.

After filtering with $q(\tau)$, the received signal $\tilde{y}(t)$ is sampled at a rate of $1/T$ to yield the receive sequence $\tilde{y}[k]$. The sampling rate is either chosen equal to the symbol rate or as an integer multiple $\eta \geq 1$ of this ($T_s = \eta T$ with oversampling factor η) to account for the

bandwidth spread that is introduced by the channel [11]. The receive filter $q(\tau)$ may either be a simple matched filter that is matched to the transmit pulse only, $q(\tau) = p^*(-\tau)$, or a more sophisticated pulse that maximizes the signal to noise ratio (SNR) at the sampling instant for every channel realization or in a statistical sense.

In our model, the data bearing impulse signal

$$x(t) = \sum_{m=-\infty}^{\infty} x[m]\delta(t - mT_s) \tag{2.12}$$

is transmitted over an effective overall channel $h(t, \tau)$ that comprises the transmit filter $p(\tau)$, the LTV channel $g(t, \tau)$, and the receive filter $q(\tau)$

$$\begin{aligned} h(t, \tau) &= p(\tau) \circledast g(t, \tau) \circledast q(\tau) \\ &= \int_{\beta} \int_{\alpha} q(\beta) g(t - \beta, \alpha) p(\tau - \beta - \alpha)\, d\alpha\, d\beta \end{aligned} \tag{2.13}$$

where (2.13) follows from applying (2.5) twice. As the channel $g(t, \tau)$ is a time-varying system, the order of arrangement is of importance and, therefore, affects the overall response $h(t, \tau)$ along with its correlation properties.

Based on $h(t, \tau)$, we can now describe the input-output relationship of our transmission model (see Fig. 2.2) in the discrete-time domain as follows:

$$\tilde{y}[k] = \sum_{l=-L_1}^{L_2} h[k, l]x[k - l] + n[k] \tag{2.14}$$

where $h[k, l] = h(kT, lT)$ is the discrete-time response at time k to an impulse with lag l. $n[k] = \int q(\tau) w(kT - \tau)\, d\tau$ is a colored noise sequence in general. In (2.14), the transmit sequence $x[l]$ is an oversampled version of $x[m]$ in order to allow for different rates at transmitter and receiver

$$x[l] = \begin{cases} x[m], & \text{if } l = \eta m, \\ 0, & \text{otherwise.} \end{cases} \tag{2.15}$$

Although the support of $g(t, \tau)$ was assumed to be finite and causal, $h(t, \tau)$ is of infinite duration in the strict sense, because $p(\tau)$ and $q(\tau)$ are usually band-limited filters. However, the effective support of $h(t, \tau)$ and, therefore, $h[k, l]$ is virtually finite, and denoted by the range $[-L_1, L_2]$, where L_1 and L_2 are non-negative integers.

To assure that the discrete-time model (2.14) is equivalent to its continuous-time counterpart, the statistical properties of the former should reflect those of the latter. Since the considered transmission model is linear and $g(t,\tau)$ is a Rayleigh process, also $h[k,l]$ will be a (now discrete-time) Rayleigh process. As already pointed out, $h[k,l]$ may however be lacking some of the specific correlation properties of $g(t,\tau)$, which was assumed to be WSSUS with separable scattering function. Using (2.13) and (2.11), the autocorrelation of the sampled overall response $h[k,l]$ is deduced as

$$\begin{aligned} R_{hh}[k_1,k_2;l_1,l_2] &\triangleq \mathrm{E}\{h[k_1,l_1]h^*[k_2,l_2]\} \\ &= \int_0^{T_g} \phi(\tau) \int_{\beta_1}\int_{\beta_2} \psi([k_1-k_2]T-(\beta_1-\beta_2))\, q(\beta_1)q^*(\beta_2) \\ &\quad \cdot p(l_1T-\tau-\beta_1)p^*(l_2T-\tau-\beta_2)\, d\beta_2\, d\beta_1\, d\tau. \end{aligned} \tag{2.16}$$

Since its autocorrelation depends on the difference k_1-k_2 only, the discrete-time Rayleigh process $h[k,l]$ is still WSS. However, both the uncorrelated scattering and the separability property are lost and the above correlation function is an unpleasant expression mixing time and delay correlations. Especially, the lack of separability prohibits the use of efficient channel simulators for Clarke's reference model (like [6]) as the time correlation function is different from $\psi([k_1-k_2]T) = J_0(2\pi B_d[k_1-k_2]T)$. However, as we will see soon, when specific condition is met, the following approximation holds

$$R_{hh}[k_1,k_2;l_1,l_2] \approx \psi([k_1-k_2]T)\cdot\varphi[l_1,l_2] \tag{2.17}$$

where

$$\varphi[l_1,l_2] = \int_0^{T_g} \phi(\tau) r(l_1T-\tau) r^*(l_2T-\tau)\, d\tau \tag{2.18}$$

with $r(\tau) = \int q(\alpha)p(\tau-\alpha)\, d\alpha$ being the convolution of $p(\tau)$ and $q(\tau)$.

To derive the condition under which (2.17) holds, we first study the right hand side (RHS) of (2.17), which actually belongs to a notional transmission model that arranges $g(t,\tau)$ and the receive filter $q(\tau)$ in reversed order. The overall impulse response $\tilde{h}(t,\tau) \triangleq p(\tau) \circledast q(\tau) \circledast g(t,\tau)$ of such a configuration is given by

$$\tilde{h}(t,\tau) = \int_\beta \int_\alpha g(t,\alpha) q(\beta) p(\tau-\beta-\alpha)\, d\alpha\, d\beta. \tag{2.19}$$

In (2.19), the absolute time t in $g(t,\tau)$ is not being delayed [compare (2.13)], since the time-varying channel is now the last system in the sequence. Using (2.19), it is easily verified that the autocorrelation of the sampled response $\tilde{h}[k,l] = \tilde{h}(kT, lT)$ is given by (2.17). Following this argument, we resort to the conception of "jointly underspread" stated in Section 2.2, to find out the condition for the validness of (2.17). In this case, the receiver filter $q(\tau)$ and time-variant physical channel $g(t;\tau)$ are "jointly underspread", thus approximately commutative, i.e. $g(t;\tau) \circledast q(\tau) \approx q(\tau) \circledast g(t;\tau)$, when

$$\bar{\tau}_q^{(1)} \bar{\nu}_g^{(1)} \ll 1 \tag{2.20}$$

where $\bar{\tau}_q^{(1)}$ and $\bar{\nu}_g^{(1)}$ are the *mean duration* of the receiver filter and the *mean Doppler spread* of the LTV physical channel defined, respectively, as

$$\bar{\tau}_q^{(1)} \triangleq \frac{\int_\tau |\tau||q(\tau)|d\tau}{\|q\|_1} \tag{2.21}$$

and

$$\bar{\nu}_g^{(1)} \triangleq \frac{\int_\tau \int_\nu |\nu||S_g(\nu,\tau)|d\nu d\tau}{\|S_g\|_1} \tag{2.22}$$

From (2.21), the $\bar{\tau}_q^{(1)}$ relates to the duration of receiver filter T_q, thus $1/B_q$, by some constant c_1 depending on the specific filter employed, where B_q is the bandwidth of receive filter $q(\tau)$. Similarly, from (2.22), $\bar{\nu}_g^{(1)}$ relates to maximum Doppler shift B_d by some constant c_2. We thus obtain the equivalent "jointly underspread" condition for (2.20) as

$$B_d/B_q \ll 1 \tag{2.23}$$

Approximation: If the Doppler spread B_d of the linear time-varying channel $g(t,\tau)$ is small compared to the bandwidth B_q of the receive filter $q(\tau)$, i. e., if $B_d/B_q \ll 1$, then the autocorrelation of the discrete-time response $h[k,l]$ is approximately separable, and has the form given by (2.17).

The requirement $B_d/B_q \ll 1$ is well fulfilled in most practical applications. Take the UMTS standard [12] as an example. The standard specifies a square-root raised cosine

transmit filter with roll-off factor 0.22 and a symbol period of $T_s = 260.42\,\text{ns}$. At a carrier frequency of 2 GHz, for a mobile velocity of 200 km/h, and assuming a receive filter that is equal to the transmit filter, we have $B_d/B_q < 10^{-4}$.

Since the scattering function of the discrete-time channel $h[k,l]$ is approximately separable for practical communication scenarios, every path $h[k,\cdot]$ of the discrete-time model (2.14) is a Rayleigh process with a Doppler spectrum according to Clarke's reference model. We may, therefore, use efficient sum-of-sinusoids simulators that have been designed for this model. If such a simulator is able to produce uncorrelated path processes $h[k,\cdot]$ (as the one proposed in [6]), then the path correlations according to (2.17)–(2.18) can be introduced by treating the impulse response $h[\cdot,l]$, $-L_1 \leq l \leq L_2$ as a vector and multiplying this vector with a correlation matrix whose entries are given by (2.18). More on this issue together with an extension to MIMO systems can be found in [9].

2.4 Numerical Simulations

In this section, we study the effect of Doppler spread B_d on the approximating accuracy of channel autocorrelation given by (2.17) to the actual autocorrelation given by (2.16), with numerical simulations.

Remark: From the right hand side of (2.17), it is easy to see that the term $\varphi[l_1,l_2]$ is independent of Doppler spread B_d, and becomes a constant once the channel tap pair $\{l_1,l_2\}$ is fixed. The other term, $\psi([k_1-k_2]T) = J_0(2\pi B_d[k_1-k_2]T)$, however, is a function of Doppler spread B_d and time difference $\Delta t = [k_1-k_2]T$. As a result, the approximating autocorrelation boils down to a scaled zero-order Bessel function of the first kind, $K \cdot J_0(x)$, with $x = 2\pi B_d[k_1-k_2]T$ and $K = \varphi[l_1,l_2]$ being the inter-tap correlation between the l_1-th and the l_2-th taps.

Based on above remark, for a fixed channel tap pair $\{l_1,l_2\}$ and a set of pre-determined discrete points $\{x_i\}_{i=1}^N$, an approximation autocorrelation curve can be obtained, which is denoted as $\tilde{R}_{hh}[i] = K \cdot J_0(x_i)$ for $1 \leq i \leq N$. Similarly, for a given Doppler spread B_d,

the corresponding actual autocorrelation curve can be evaluated according to (2.16), with numerical integration. Herein, the actual autocorrelation curve is denoted by $R_{hh}[i]$ for $1 \leq i \leq N$. The *normalized absolute error* between $R_{hh}[i]$ and $\tilde{R}_{hh}[i]$ is measured as

$$e[i] = \frac{\left| R_{hh}[i] - \tilde{R}_{hh}[i] \right|}{K} \tag{2.24}$$

where the normalization to K takes fading channel power into account. Further, we can define the mean and standard deviation of the error sequence $\{e[i]\}_{i=1}^{N}$, respectively, as

$$m_e = \frac{1}{N} \sum_{i=1}^{N} e[i], \tag{2.25}$$

and

$$\sigma_e = \sqrt{\frac{1}{N} \sum_{i=1}^{N} (e[i] - m_e)^2}. \tag{2.26}$$

Based on the theoretical analysis in Section 2.3, smaller B_d/B_q means better approximation in (2.17) thus smaller approximation error $e[i]$ (m_e and σ_e), which will be evident soon in the simulation results.

The system parameters in [9], is adopted for the simulation. The power delay profile (PDP) $\phi(\tau)$ of the Rayleigh fading channel is a reduced six-path typical urban (TU) profile. The transmit filter is a linearized Gaussian filter with a time-bandwidth product of 0.3, and the receive filter is a square root raised cosine (SRC) filter with a roll-off factor $r = 0.3$ The sampling period at the receiver side is the same as the symbol period at the transmitter side, that is $T = T_s = 3.69\mu s$. For such a system configuration, the tap index l of $h[k, l]$ is in the range of $[-L_1, L_2]$ with $L_1 = 1, L_2 = 3$. Alternative to B_d/B_q, *normalized Doppler spread* defined as, $\hat{B}_d = B_d T$, is used in the simulation noticing that B_q relates to T by $B_q = (1 + r)/T$. The approximating accuracy is investigated at seven different normalized Doppler spreads $\hat{B}_d$, which are listed (together the Doppler to receive filter bandwidth ratio B_d/B_q) in Table 2.1. To evaluate the correlation curve, $N = 100$ equally-spaced points are chosen with the starting point $x_1 = 0$ and the interval $\Delta x \triangleq x_{i+1} - x_i = 0.1$. It is noted that once the points have been fixed, the lag Δt varies with Doppler spread B_d. Simulation results are presented through Fig. 2.3 to Fig. 2.6.

Table 2.1: Normalized Doppler spread: $\hat{B}_d$

$\hat{B}_d$	5.0×10^{-1}	1.0×10^{-1}	1.0×10^{-2}	1.0×10^{-3}	1.0×10^{-4}	1.0×10^{-5}
B_d/B_q	3.8×10^{-1}	7.7×10^{-2}	7.7×10^{-3}	7.7×10^{-4}	7.7×10^{-5}	7.7×10^{-6}

First, we study the channel autocorrelation of $h[k,l]$ with $l_1 = 1, l_2 = 0$. The scale factor K is computed as $K = \varphi[1,0] = 0.329$. In Fig. 2.3, the approximation autocorrelation curve and four actual autocorrelation curves with different normalized Doppler values, are plotted. Obviously, the approximation autocorrelation gradually deviates the actual one

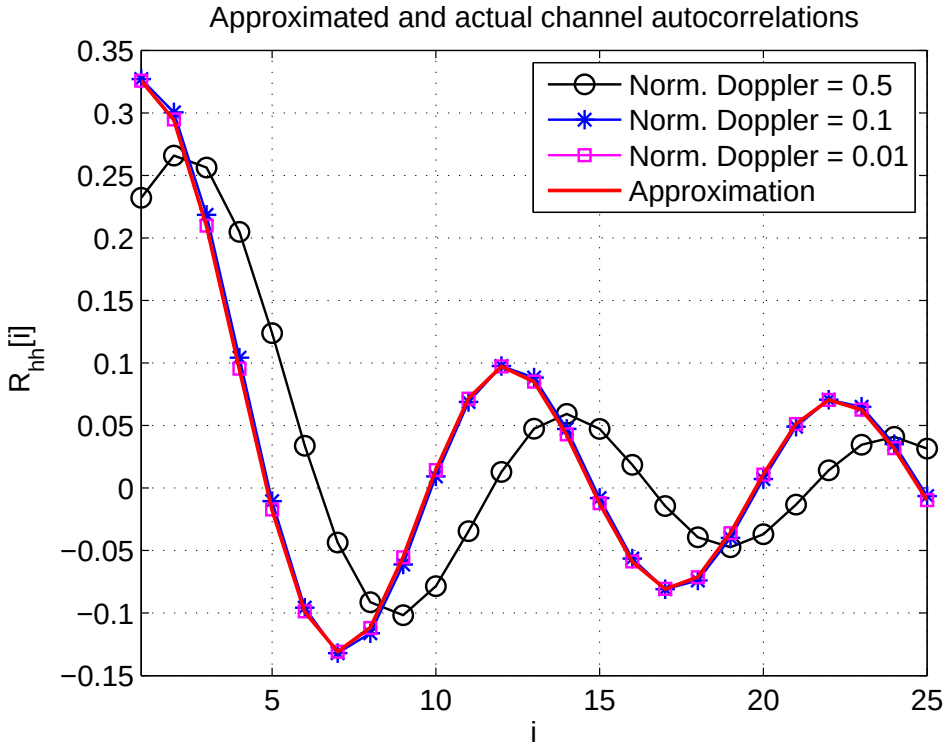

Figure 2.3: Approximated and actual autocorrelations: $l_1 = 1, l_2 = 0$

when the Doppler spread gets large. When $\hat{B}_d = 0.5$, that is the Doppler spread B_d is comparable to system bandwidth B_q, the approximation does not make sense anymore.

The normalized approximation error $e[i]$ is shown in Fig. 2.4. From the figure, the approximation error is negligible (or the approximation accuracy is high), when $\hat{B}_d$ is in the order of 10^{-2}. Fig. 2.5 demonstrates the mean, m_e, and standard deviation, σ_e, of normalized absolute error, $e[i]$, at different normalized Doppler spreads. It is obvious that

both mean and standard deviation of approximation error are close to zero when $\hat{B}_d$ is in the order of 10^{-2} or smaller.

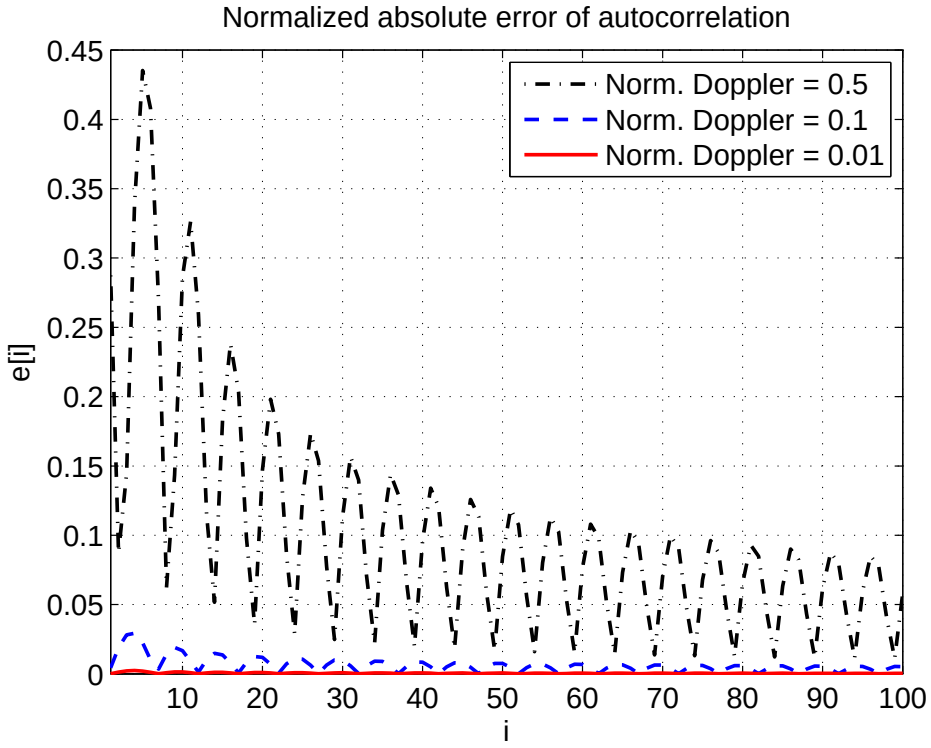

Figure 2.4: Normalized absolute error of autocorrelation: $l_1 = 1, l_2 = 0$

The results demonstrated through Fig. 2.3 to Fig. 2.5 for $l_1 = 1, l_2 = 0$, are also observed with other choices of l_1, l_2. For example, when $l_1 = 0, l_2 = 0$ where $K = \varphi[0, 0] = 0.738$, the mean and standard deviation of the approximation error is shown in Fig. 2.6, which provides similar observation to Fig. 2.5.

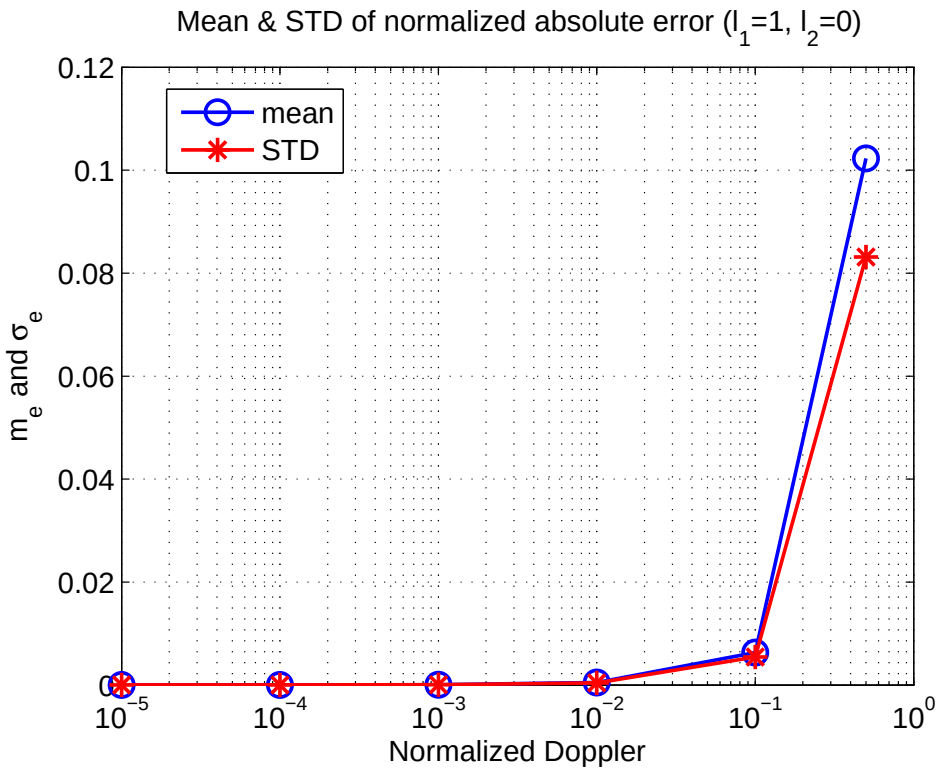

Figure 2.5: Mean and STD of normalized absolute error: $l_1 = 1, l_2 = 0$

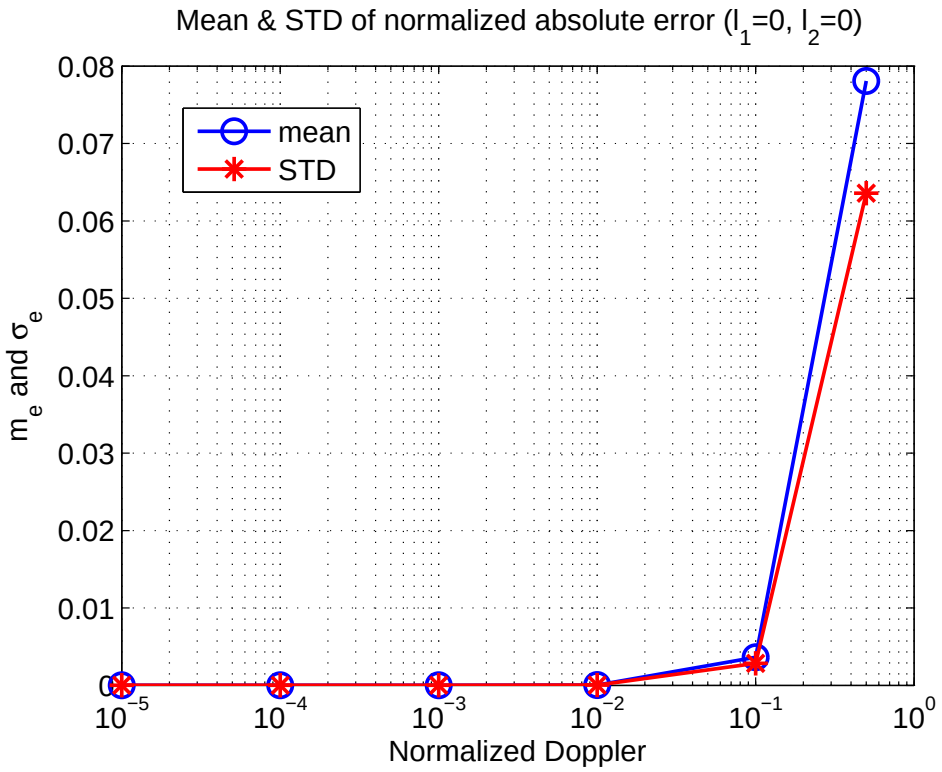

Figure 2.6: Mean and STD of normalized absolute error: $l_1 = 0, l_2 = 0$

So far, numerical simulations have verified the theoretical findings in Section 2.3. The condition $B_d/B_q \ll 1$ is well fulfilled in nearly all practical systems. In multi-carrier systems like OFDM, however, the channel Doppler spread is not always negligibly small relative to the subcarrier bandwidth. To give an example, mobile reception of Digital Video Broadcasting Terrestrial (DVB-T) may cause Doppler spreads up to $\hat{B}_d = 0.05$ at high velocities. For OFDM in matched-filter bank representation, where the receiver is using integrate-and-dump, this number then determines the approximation accuracy. In simulation and practical implementation, DFT processing together with a wideband transmit pulse commonly replaces the analog filter bank. At the receiver, this has the same effect as oversampling, as it reduces the ratio B_d/B_q by a factor equal to the number of OFDM subcarriers.

2.5 Conclusion

Unlike time-invariant systems, LTV systems are not commutative in general. As it was shown and discussed in this chapter, the attribute of non-commutativity may affect the discrete-time representation of a digital transmission over WSSUS channels including transmit and receive filtering. For the composite discrete-time channel, the WSS property is preserved, but in general both the uncorrelated scattering and separability properties are lost. In this chapter, we have provided the true and approximate representation of the overall discrete-time channel response and have analyzed and compared their correlation functions in detail. The approximate discrete-time channel correlation function decomposes into independent parts and preserves the original property of the WSSUS channel. The approximation, which is valid if the channel Doppler spread is small relative to the bandwidth of the receive filter, reflects the composite response of a virtual transmission model that interchanges the order of receive filter and LTV physical channel. Under this simplification, WSSUS channels retain a convenient representation in the discrete-time domain and facilitate the use of efficient channel simulators for Rayleigh and Rician channels.

Chapter 3

Doppler Spread Estimation for Wireless OFDM Systems

3.1 Introduction

OFDM has become the dominant information transmission technique for a number of current and future wireless communication systems [13] – [19]. OFDM is designed primarily for system with quasi-static fading, *i.e.*, the channel keeps constant during at least one symbol duration. To meet the ever increasing demand for broadband pervasive communication, OFDM systems designed for future wireless communications are expected to operate in an environment with high data transmission rate, high mobility, and high carrier frequency. High speed broadband communication dictates an operating environment of fast time-varying and frequency-selective fading. Fast time-varying fading introduces Doppler spread, which destroys the orthogonality among subcarriers in OFDM and causes inter-carrier interference (ICI), which is one of the main performance degrading factors for OFDM systems [20] – [22].

On the other hand, Doppler spread contains information about the key statistics of the wireless channel, and it provides important guidance for system design. Doppler spread has been utilized in single carrier systems for adaptive handoff algorithm [23], energy-efficient routing for mobile ad hoc networks [24], mobility and resource management for wireless multimedia networks [25], trajectory prediction for wireless networks with mobile base stations [26]. It has also been used in OFDM-based communication systems for adaptive

channel estimation [27], [28], adaptive power control [29], and adaptive modulation and coding (ACM) [30]. Therefore, a good estimation of the Doppler spread is important for the design and implementation of practical wireless communication systems.

Doppler spread estimation has received extensive attentions for single carrier communication systems [31] – [40]. However, there are very limited works on Doppler spread estimation for OFDM systems [41] – [44]. Auto-correlation functions of frequency domain signal [41] and time domain signal [42] are evaluated at pilot tones and used to estimate Doppler spread. Since pilot tones only account for a small percentage of transmitted signals, a large number of OFDM blocks are required to extract the necessary channel statistics in the methods proposed in [41] and [42]. The algorithms in [41] and [42] require the knowledge of the channel state information, which is usually difficult to extract, especially at high Doppler spread and low signal-to-noise ratio (SNR). In addition, the performance of the algorithm in [41] is negatively affected by ICI due to its frequency domain operation. In [43], Doppler spread is estimated by extracting the correlation between cyclic prefix (CP) and its data counterpart within one OFDM symbol. Only the portion of the CP that has not been corrupted can be used for estimation, which limit the applicability of this method in practical systems. All of these works assume a simplified discrete-time tapped-delay-line channel model with uncorrelated channel coefficients. It has been shown in [9] and [45] (also Chapter 2) that the channel taps of equivalent discrete-time representation of the fading channel are actually correlated due to the time span of transmit filter and receive filter, and this correlation information is important for system design and evaluation. Furthermore, to the best of our knowledge, all existing algorithms are designed primarily for Rayleigh fading channels and they are unable to provide satisfactory Doppler estimation results for frequency-selective Rician fading channel.

In this chapter, a new Doppler spread estimation algorithm that does not suffer from any of the aforementioned limitations is proposed for broadband OFDM systems operating under doubly-selective (time-selective and frequency-selective) Rayleigh and Rician fading channels. The estimation is performed by collecting statistics from all the received time

domain signals. Unlike previous methods, the new algorithm doesn't require pilot symbols, and can operate at the presence of both unknown channel coefficients and unknown data symbols. It is robust to ICI and additive noise, and can provide accurate estimation of the Doppler spread even when the SNR is as low as 0 dB. In addition, the channel tap correlation of the equivalent discrete-time system representation is considered during the development of the algorithm. Simulation results show that the new algorithm provides accurate and high-efficiency estimation of the Doppler spread over a wide range of system configurations.

3.2 System Model and Assumptions

Consider an OFDM system with block diagram shown in Fig. 3.1.

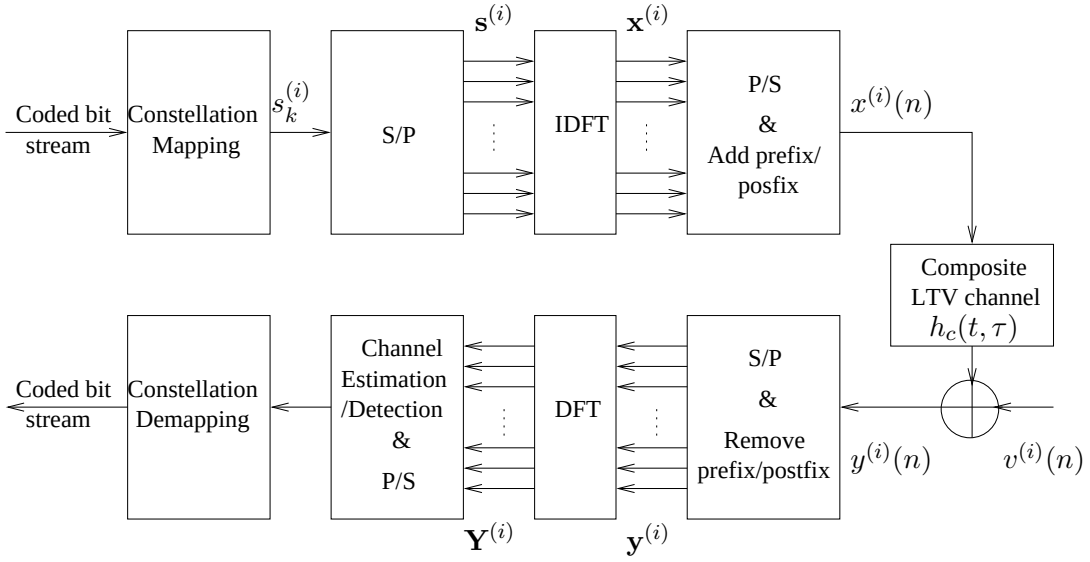

Figure 3.1: OFDM system model (only $y^{(i)}(n)$ is used during Doppler estimation).

For the ith ($i \in \mathbb{Z}^+$) OFDM symbol, a set of N modulation symbols, $\{s_k^{(i)}\}_{k=0}^{N-1}$, are multiplexed onto N orthonormal subcarriers, and the obtained time-domain samples, $x^{(i)}(n)$, can be expressed as

$$x^{(i)}(n) = \frac{1}{\sqrt{N}} \sum_{k=0}^{N-1} s_k^{(i)} e^{j\frac{2\pi}{N}kn}, -N_p \leq n < N + N_q \tag{3.1}$$

where $s_k^{(i)} \in \mathcal{S}$ with $\mathcal{S}$ being the modulation alphabet set, N_p and N_q are the lengths of

cyclic prefix and cyclic postfix, respectively. Cyclic prefix and postfix are used to remove ISI introduced by the causal part and non-causal part of the equivalent channel [9].

The modulation symbols, $s_k^{(i)}$, are assumed to be zero-mean complex random variables, and the cross-correlation between two modulation symbols is

$$\mathbb{E}\left\{s_{k_1}^{(i)}\left[s_{k_2}^{(j)}\right]^*\right\} = \delta(k_1 - k_2)\delta(i - j), \tag{3.2}$$

where $\mathbb{E}(\cdot)$ represents the operation of mathematical expectation, $\delta(\cdot)$ is the Kronecker delta function, and $(\cdot)^*$ stands for complex conjugate. The assumption is valid for a wide range of modulation schemes such as M-ary phase shift keying (MPSK), M-ary quadrature amplitude modulation (MQAM), etc.

Throughout this chapter, the complex baseband transmission is considered. The time-domain samples, $x^{(i)}(n)$, are passed through a transmit filter, $p_{_T}(\tau)$, and then transmitted over the wireless physical channel, $g_c(t,\tau)$. At the receiver, the received time domain signal is passed through a receive filter, $p_{_R}(\tau)$. Define the continuous-time composite impulse response of the channel as

$$h_c(t,\tau) = p_{_T}(\tau) \otimes g_c(t,\tau) \otimes p_{_R}(\tau), \tag{3.3}$$

where $a(\tau) \otimes b(t,\tau) = \int b(t,\alpha)a(\tau-\alpha)d\alpha$ represents convolution of time varying signals. For system experiencing Rician fading, $g_c(t,\tau)$ can be modeled as [46]

$$g_c(t,\tau) = \frac{g(t,\tau)}{\sqrt{1+K}} + \sqrt{\frac{K}{1+K}}h_{_{LOS}}(t)\delta(\tau) \tag{3.4}$$

where K is the Rice factor, $g(t,\tau)$ is wide-sense stationary uncorrelated scattering (WSSUS) [3] Rayleigh fading component with normalized unit energy, and the line-of-sight (LOS) component is assumed to be $h_{_{LOS}}(t) = \exp(j2\pi f_d t\cos\theta_0 + j\phi_0)$, with f_d being the maximum Doppler spread, θ_0 and ϕ_0 the angle of arrival (AOA) and the initial phase, respectively. It's assumed that θ_0 and ϕ_0 are uniformly distributed over $(-\pi,\pi]$.

At the receiver, the output of the receive filter is sampled at a rate of $1/T_s$. After the removal of cyclic prefix and cyclic postfix, the received time domain samples can be

represented as [9]

$$y^{(i)}(n) = \frac{1}{\sqrt{1+K}} \sum_{l=-L_1}^{L_2} h^{(i)}(n,l)x^{(i)}(n-l) + \sqrt{\frac{K}{1+K}} h^{(i)}_{LOS}(n) \sum_{p=-P_1}^{P_2} \rho_p x^{(i)}(n-p) + v^{(i)}(n),$$
$$\text{for } n = 0, 1, \cdots, N-1 \tag{3.5}$$

where $y^{(i)}(n) \triangleq y((iN_s + n)T_s)$ is the nth sample of the ith received OFDM symbol, with $N_s = N_p + N + N_q$ being the number of samples within one OFDM symbol including prefix and postfix, and $v^{(i)}(n)$ is the additive white Gaussian noise (AWGN) sample with mean zero and variance σ^2. The coefficients of the non-line-of-sight (NLOS) component, $h^{(i)}(n,l) \triangleq h((iN_s + n)T_s, lT_s)$, for $l = -L_1, \cdots, L_2$, are the discrete-time version of the continuous-time CIR, $h(t,\tau) = p_{_R}(\tau) \otimes g(t,\tau) \otimes p_{_T}(\tau)$, with the non-negative integers, L_1 and L_2, determined by the transmit filter, receive filter, and channel power delay profile [9]. The discrete-time version of the LOS component is $h^{(i)}_{_{LOS}}(n) = h_{_{LOS}}((iN_s + n)T_s)$. The effects of the transmit filter and receive filter on the LOS component is summarized in the coefficient, $\rho_p = \int_{-\infty}^{\infty} p_{_T}(s)p_{_R}(pT_s - s)ds$, for $p = -P_1, \cdots, P_2$, with the non-negative integers P_1 and P_2 determined by the transmit and receive filters. For energy normalized transmit and receive filters, we have $\sum_{p=-P_1}^{P_2} \rho_p^2 = 1$. Specifically, $\rho_p = \delta(p)$ for filters satisfying Nyquist criterion. It should be noted that, with the insertion of cyclic prefix and postfix, the signal sample, $y^{(i)}(n)$, contains information contributed only from the ith transmitted OFDM symbol, $x^{(i)}(n)$.

Due to the time span of the transmit filter and receive filter, the discrete-time NLOS channel coefficient, $h^{(i)}(n,l)$, is generally non-causal and mutually correlated across the delay domain l, even though the underlying physical channel is causal and experiences uncorrelated scattering. The NLOS coefficients form a wide-sense stationary zero mean complex Gaussian random process with auto-correlation given by [9]

$$\mathbb{E}\left\{h^{(i_1)}(n_1,l_1)\left[h^{(i_2)*}(n_2,l_2)\right]^*\right\} = C_{l_1,l_2} J_0\left\{2\pi f_d\left[(i_1 - i_2)N_s + (n_1 - n_2)\right]T_s\right\} \tag{3.6}$$

where C_{l_1,l_2} is the inter-tap correlation, $J_0(\cdot)$ is the zero-order Bessel function of the first kind, and f_d is the maximum Doppler spread. The value of C_{l_1,l_2} is determined by transmit

filter, channel power delay profile, and receive filter. For energy normalized composite channel, we have $\sum_{l=-L_1}^{L_2} C_{l,l} = 1$.

3.3 Algorithm Development Based on Time-Domain Signal Statistics

In this section, theoretical analysis is performed to investigate the key second-order and fourth-order statistics of the received time-domain samples, $y^{(i)}(n)$, and the results are used to facilitate the development of the Doppler spread estimation algorithm.

3.3.1 Statistics of Received Signals

Define the auto-correlation of the received time domain signal, $y^{(i)}(n)$, and the auto-correlation of received signal power, $|y^{(i)}(n)|^2$, as

$$R_{yy}(s,u,n,m) \triangleq \mathbb{E}\left\{y^{(s)}(n+m)\left[y^{(u)}(n)\right]^*\right\} \tag{3.7a}$$

$$R_{|y|^2|y|^2}(s,u,n,m) \triangleq \mathbb{E}\left\{|y^{(s)}(n+m)|^2|y^{(u)}(n)|^2\right\} \tag{3.7b}$$

where $s, u \in \mathbb{Z}^+$ are OFDM symbol indices, and n and m are time instant and time lag in samples, respectively.

Substituting (3.1) and (3.5) into (3.7), we have the auto-correlations expressed in (3.8) and (3.9), where the identities, $J_0\left\{2\pi f_d\left[(s-u)N_s+m\right]T_s\right\}\delta(s-u) = J_0(2\pi f_d m T_s)\delta(s-u)$, and $\cos\left\{2\pi f_d\left[(s-u)N_s+m\right]\ T_s\cos\theta_0\right\}\delta(s-u) = \cos(2\pi f_d m T_s\cos\theta_0)\delta(s-u)$, are used in the derivation of (3.8) and (3.9). The proofs for (3.8) and (3.9) are delegated to the Appendix A. Observing (3.8) and (3.9) reveals that both $y(n)$ and $|y(n)|^2$ are wide-sense stationary since they are functions of symbol index difference $s-u$ and time difference m, while independent of the starting symbol index s and starting time instant n. Therefore, we denote $R_{yy}(s,u,n,m) \triangleq R_{yy}(s-u,m)$ and $R_{|y|^2|y|^2}(s,u,n,m) \triangleq R_{|y|^2|y|^2}(s-u,m)$ in

the sequel unless specified otherwise.

$$R_{yy}(s,u,n,m) = \left[\frac{1}{N(1+K)}\sum_{l_1=-L_1}^{L_2}\sum_{l_2=-L_1}^{L_2}\sum_{k=0}^{N-1} C_{l_1,l_2}J_0(2\pi f_d m T_s)e^{j\frac{2\pi(l_2-l_1+m)k}{N}} + \right.$$
$$\left.\frac{K}{N(1+K)}\sum_{p_1=-P_1}^{P_2}\sum_{p_2=-P_1}^{P_2}\sum_{k=0}^{N-1}\rho_{p_1}\rho_{p_2}^{*}e^{j2\pi f_d m T_s\cos\theta_0}e^{j\frac{2\pi(p_2-p_1+m)k}{N}} + \sigma^2\delta(m)\right]\delta(s-u) \quad (3.8)$$

$$R_{|y|^2|y|^2}(s,u,n,m) =$$
$$1+2\sigma^2+\sigma^4+2\sigma^2\delta(m)\delta(s-u)+\sigma^4\delta(m)\delta(s-u)$$
$$+\frac{J_0^2\left\{2\pi f_d\left[(s-u)N_s+m\right]T_s\right\}}{(1+K)^2}\sum_{l_1=-L_1}^{L_2}\sum_{l_2=-L_1}^{L_2}|C_{l_1,l_2}|^2$$
$$+\frac{2KJ_0\left\{2\pi f_d\left[(s-u)N_s+m\right]T_s\right\}\cos\left\{2\pi f_d\left[(s-u)N_s+m\right]T_s\cos\theta_0\right\}}{(1+K)^2}\times$$
$$\sum_{l_1=-L_1}^{L_2}\sum_{\substack{l_2=-L_1\\ l_1=p_1,l_2=p_2}}^{L_2}\sum_{p_1=-P_1}^{P_2}\sum_{p_2=-P_1}^{P_2}C_{l_1,l_2}\rho_{p_1}^{*}\rho_{p_2}$$
$$+\frac{1}{(1+K)^2N^2}\sum_{l_1=-L_1}^{L_2}\sum_{l_2=-L_1}^{L_2}\sum_{l_3=-L_1}^{L_2}\sum_{l_4=-L_1}^{L_2}\sum_{\substack{k_1=0\\ k_1\neq k_2}}^{N-1}\sum_{k_2=0}^{N-1}\left[C_{l_1,l_2}C_{l_3,l_4}+C_{l_1,l_4}C_{l_2,l_3}^{*}J_0^2(2\pi f_d m T_s)\right]\times$$
$$e^{j\frac{2\pi[k_1(m+l_4-l_1)-k_2(m+l_3-l_2)]}{N}}\delta(s-u)$$
$$+\frac{K}{(1+K)^2N^2}\sum_{l_1=-L_1}^{L_2}\sum_{l_2=-L_1}^{L_2}\sum_{p_1=-P_1}^{P_2}\sum_{p_2=-P_1}^{P_2}\sum_{\substack{k_1=0\\ k_1\neq k_2}}^{N-1}\sum_{k_2=0}^{N-1}C_{l_1,l_2}\rho_{p_1}\rho_{p_2}^{*}\times$$
$$\left[e^{j\frac{2\pi[k_1(m-l_1+p_2)-k_2(m-l_2+p_1)]}{N}}+e^{j\frac{2\pi[k_1(m-p_1+l_2)-k_2(m-p_2+l_1)]}{N}}\right]\delta(s-u)$$
$$+\frac{2KJ_0(2\pi f_d m T_s)\cos(2\pi f_d m T_s\cos\theta_0)}{(1+K)^2N^2}\sum_{l_1=-L_1}^{L_2}\sum_{l_2=-L_1}^{L_2}\sum_{p_1=-P_1}^{P_2}\sum_{p_2=-P_1}^{P_2}\sum_{\substack{k_1=0\\ k_1\neq k_2}}^{N-1}\sum_{k_2=0}^{N-1}C_{l_1,l_2}\rho_{p_1}^{*}\rho_{p_2}\times$$
$$e^{j\frac{2\pi[k_1(m+l_2-l_1)-k_2(m+p_2-p_1)]}{N}}\delta(s-u)$$
$$+\frac{K^2}{(1+K)^2N^2}\sum_{p_1=-P_1}^{P_2}\sum_{p_2=-P_1}^{P_2}\sum_{p_3=-P_1}^{P_2}\sum_{p_4=-P_1}^{P_2}\sum_{\substack{k_1=0\\ k_1\neq k_2}}^{N-1}\sum_{k_2=0}^{N-1}\rho_{p_1}\rho_{p_2}^{*}\rho_{p_3}\rho_{p_4}^{*}\times$$
$$e^{j\frac{2\pi[k_1(m+p_4-p_1)-k_2(m+p_3-p_2)]}{N}}\delta(s-u) \quad (3.9)$$

Setting $s-u=0, m=0$ in (3.8), we have $R_{yy}(0) \triangleq R_{yy}(s=u, m=0)$ as

$$\begin{aligned} R_{yy}(0) &= \frac{1}{N(1+K)} \sum_{l_1=-L_1}^{L_2} \sum_{l_2=-L_1}^{L_2} \sum_{k=0}^{N-1} C_{l_1,l_2} e^{j\frac{2\pi(l_2-l_1)k}{N}} + \\ &\quad \frac{K}{N(1+K)} \sum_{p_1=-P_1}^{P_2} \sum_{p_2=-P_1}^{P_2} \sum_{k=0}^{N-1} \sigma_{p_1} \sigma_{p_2}^{*} e^{j\frac{2\pi(p_2-p_1)k}{N}} + \sigma^2 \\ &= 1+\sigma^2 \end{aligned} \tag{3.10}$$

Thus, the auto-covariance of the received signal power can be written as

$$\begin{aligned} V_{|y|^2|y|^2}(s-u,m) &= R_{|y|^2|y|^2}(s-u,m) - \mathbb{E}^2\left[\left|y^{(s)}(n)\right|^2\right] \\ &= R_{|y|^2|y|^2}(s-u,m) - (1+\sigma^2)^2 \end{aligned} \tag{3.11}$$

The statistics described in (3.8), (3.9) and (3.11) are expressed as functions of the Doppler spread f_d. However, the expressions of the statistics are extremely complicated, thus it would be rather difficult, if not impossible, to directly extract the values of f_d based on these expressions. To facilitate the development of the Doppler spread estimation algorithm, we have the following three remarks on the signal statistics.

Remark 1: From (3.8), we observe that signals from different OFDM symbols, *i.e.*, $(s \neq u)$, are always uncorrelated regardless of the value of m. This observation is intuitive since signals within one OFDM symbol are independent from adjacent OFDM symbols due to the presence of cyclic prefix and cyclic postfix. For the case $s=u$, the auto-correlation of the received signal samples within one OFDM symbol interval is also zero if $L<|m|<N-L$, where $L=L_1+L_2$, because both of the triple summation terms in (3.8) are zeros in this case. For other values of m, the value of $R_{yy}(s-u,m)$ is involved with m in a very complicated way as evident in (3.8). Therefore, the auto-correlation function, $R_{yy}(s-u,m)$, is not a good candidate for Doppler estimation.

Remark 2: When $s \neq u$, the auto-correlation and auto-covariance of received signal

power in (3.9) and (3.11) can be simplified as follows

$$R_{|y|^2|y|^2}(s-u,m) = 1+2\sigma^2+\sigma^4+\frac{J_0^2\{2\pi f_d[(s-u)N_s+m]T_s\}}{(1+K)^2}\sum_{l_1=-L_1}^{L_2}\sum_{l_2=-L_1}^{L_2}|C_{l_1,l_2}|^2+$$
$$\frac{2KJ_0\{2\pi f_d[(s-u)N_s+m]T_s\}\cos\{2\pi f_d[(s-u)N_s+m]T_s\cos\theta_0\}}{(1+K)^2}\times$$
$$\sum_{l_1=-L_1}^{L_2}\sum_{\substack{l_2=-L_1\\ l_1=p_1,l_2=p_2}}^{L_2}\sum_{p_1=-P_1}^{P_2}\sum_{p_2=-P_1}^{P_2}C_{l_1,l_2}\rho_{p_1}^*\rho_{p_2} \tag{3.12}$$

$$V_{|y|^2|y|^2}(s-u,m) = \frac{J_0^2\{2\pi f_d[(s-u)N_s+m]T_s\}}{(1+K)^2}\sum_{l_1=-L_1}^{L_2}\sum_{l_2=-L_1}^{L_2}|C_{l_1,l_2}|^2+$$
$$\frac{2KJ_0\{2\pi f_d[(s-u)N_s+m]T_s\}\cos\{2\pi f_d[(s-u)N_s+m]T_s\cos\theta_0\}}{(1+K)^2}\times$$
$$\sum_{l_1=-L_1}^{L_2}\sum_{\substack{l_2=-L_1\\ l_1=p_1,l_2=p_2}}^{L_2}\sum_{p_1=-P_1}^{P_2}\sum_{p_2=-P_1}^{P_2}C_{l_1,l_2}\rho_{p_1}^*\rho_{p_2} \tag{3.13}$$

It is worth pointing out that the expression in (3.13) is independent of the AWGN variance σ^2.

Remark 3: Comparing (3.9) and (3.11) with (3.12) and (3.13), we can see that, when $s = u$, there is a complicated extra term involving f_d in the expressions of the auto-correlation and auto-covariance of signal power as compared to the $s \neq u$ case. Since it is extremely difficult to evaluate the extra term, the $s = u$ case is not a desirable candidate for Doppler spread estimation.

Based on the analysis above, we conclude that the auto-covariance of signal power evaluated at $s \neq u$ is the most suitable candidate for Doppler spread estimation. Compared to other cases, $V_{|y|^2|y|^2}(s-u,m)$ at $s \neq u$ has two advantages. First, it is directly related to the maximum Doppler spread in an expression that is easy to analyze. Second, the effect of AWGN is completely removed, and this is highly desirable for the design of a robust estimation algorithm.

3.3.2 Doppler Spread Estimation

We are now in a position to develop the Doppler spread estimation algorithm based on the auto-covariance given in (3.13). Denote

$$\alpha = \frac{1}{(1+K)^2} \sum_{l_1=-L_1}^{L_2} \sum_{l_2=-L_1}^{L_2} |C_{l_1,l_2}|^2, \tag{3.14a}$$

$$\beta = \frac{2K}{(1+K)^2} \sum_{l_1=-L_1}^{L_2} \sum_{\substack{l_2=-L_1 \\ l_1=p_1,l_2=p_2}}^{L_2} \sum_{p_1=-P_1}^{P_2} \sum_{p_2=-P_1}^{P_2} C_{l_1,l_2} \rho_{p_1}^* \rho_{p_2}, \tag{3.14b}$$

$$z = 2\pi f_d[(s-u)N_s + m]T_s, \tag{3.14c}$$

then (3.13) can be written in a compact form as

$$V_{|y|^2|y|^2}(z) = \alpha J_0^2(z) + \beta J_0(z)\cos(z\cos\theta_0) \tag{3.15}$$

Since the values of α and β are unknown, (3.15) cannot be used directly for the estimation of the Doppler spread f_d. Instead, we resort to the normalized auto-covariance defined as

$$V_N(k,z) \triangleq \frac{V_{|y|^2|y|^2}(kz)}{V_{|y|^2|y|^2}(z)} = \frac{\alpha J_0^2(kz) + \beta J_0(kz)\cos(kz\cos\theta_0)}{\alpha J_0^2(z) + \beta J_0(z)\cos(z\cos\theta_0)}, \quad (k > 1 \text{ integer}) \tag{3.16}$$

where k is an integer that can be adjusted to achieve better estimation accuracy. When k is properly chosen such that kz is small, second-order approximations, $J_0(x) \approx 1 - \frac{x^2}{4}$ and $\cos(x) \approx 1 - \frac{x^2}{2}$, can be employed, and this leads to the following approximation

$$V_N(k,z) \approx \frac{\alpha\left[1 - \frac{(kz)^2}{4}\right]^2 + \beta\left[1 - \frac{(kz)^2}{4}\right]\left[1 - \frac{(kz\cos\theta_0)^2}{2}\right]}{\alpha\left(1 - \frac{z^2}{4}\right)^2 + \beta\left(1 - \frac{z^2}{4}\right)\left[1 - \frac{(z\cos\theta_0)^2}{2}\right]}. \tag{3.17}$$

To further simplify the representation, replacing $\cos^2\theta_0$ with its expectation, $\mathbb{E}(\cos^2\theta_0) = 0.5$, we are able to cancel the two unknown parameters, α and β, from the expression of $V_N(k,z)$, and the result is

$$V_N(k,z) \approx \frac{\left[1 - \frac{(kz)^2}{4}\right]^2}{\left(1 - \frac{z^2}{4}\right)^2} \tag{3.18}$$

The solution of z from (3.18) is

$$z = 2\sqrt{\frac{1 - U_N(k,z)}{k^2 - U_N(k,z)}} \tag{3.19}$$

where $U_N(k,z) = \sqrt{V_N(k,z)}$. Let $s-u=1, m=0$, then $z = 2\pi f_d N_s T_s$, and the estimation for Doppler spread is obtained as

$$\tilde{f}_d = \frac{\sqrt{\frac{1-U_N(k,z)}{k^2-U_N(k,z)}}}{\pi N_s T_s} = \frac{F_1(k,z)}{\pi N_s T_s} \tag{3.20}$$

where

$$F_1(k,z) \triangleq \sqrt{\frac{1-U_N(k,z)}{k^2-U_N(k,z)}} \tag{3.21}$$

It should be noted that other values of $s-u$ and m can also be used in Doppler spread estimation without affecting the estimation accuracy. In this chapter, however, we fix $z = 2\pi f_d N_s T_s$ without loss of generality.

Similarly, if we employ fourth-order approximations: $J_0(x) \approx 1 - \frac{x^2}{4} + \frac{x^4}{64}$ and $\cos(x) \approx 1 - \frac{x^2}{2} + \frac{x^4}{24}$, and noting the fact that $\mathbb{E}\left(\cos^4\theta_0\right) = \frac{3}{8}$, then

$$\begin{aligned} V_N(k,z) &\approx \frac{\alpha\left[1-\frac{(kz)^2}{4}+\frac{(kz)^4}{64}\right]^2+\beta\left[1-\frac{(kz)^2}{4}+\frac{(kz)^4}{64}\right]\left[1-\frac{(kz\cos\theta_0)^2}{2}+\frac{(kz\cos\theta_0)^4}{24}\right]}{\alpha\left(1-\frac{z^2}{4}+\frac{z^4}{64}\right)^2+\beta\left(1-\frac{z^2}{4}+\frac{z^4}{64}\right)\left[1-\frac{(z\cos\theta_0)^2}{2}+\frac{(z\cos\theta_0)^4}{24}\right]} \\ &= \frac{\left[1-\frac{(kz)^2}{4}+\frac{(kz)^4}{64}\right]^2}{\left(1-\frac{z^2}{4}+\frac{z^4}{64}\right)^2}, \end{aligned} \tag{3.22}$$

from which z can be solved as

$$z = 2\sqrt{2}\sqrt{\frac{k^2-U_N(k,z)-(k^2-1)\sqrt{U_N(k,z)}}{k^4-U_N(k,z)}} \tag{3.23}$$

The Doppler spread estimation using fourth-order approximation can then be obtained from (3.23) as

$$\hat{f}_d = \frac{\sqrt{2}\sqrt{\frac{k^2-U_N(k,z)-(k^2-1)\sqrt{U_N(k,z)}}{k^4-U_N(k,z)}}}{\pi N_s T_s} = \frac{F_2(k,z)}{\pi N_s T_s} \tag{3.24}$$

where

$$F_2(k,z) \triangleq \sqrt{2}\sqrt{\frac{k^2-U_N(k,z)-(k^2-1)\sqrt{U_N(k,z)}}{k^4-U_N(k,z)}} \tag{3.25}$$

When Doppler spread estimation is obtained, the mobile speed can be calculated from Doppler spread as $v = f_d c/f_c$, where c is the speed of light and f_c is the carrier frequency.

Compared to existing algorithms, the newly proposed method has the following advantages. First, the estimation of the Doppler spread doesn't require the knowledge of fading channel coefficients or transmitted data symbols. Thus, all of the received signals, including both unknown data and known pilot, can be used in the estimation. Second, the effect of additive noise is removed in the estimation process due to the employment of the auto-covariance of received signal power. Third, the channel inter-tap correlation, which is present in practical systems, is taken into account during the estimation process. Fourth, the estimation is performed over time domain signals, thus it is not affected by ICI in frequency domain.

3.4 A Practical Doppler Estimation Algorithm

Based on the theoretical analysis presented in section 3.3, a practical Doppler spread estimation algorithm with low estimation latency and high computation efficiency is presented in this section.

From the theoretical estimators given in (3.20) and (3.24), the proper operation of the Doppler estimation algorithm requires the knowledge of the auto-covariance function, $V_{|y|^2|y|^2}(s-u,m)$, which can be approximated using time average. To obtain an accurate time-averaged approximation of the auto-covariance function, long data sequences are needed. This will result in long estimation delay with high computational complexity. To keep the estimation latency small while achieving satisfactory estimation reliability, we pass the received signal power, $p^{(i)}(n) = |y^{(i)}(n)|^2$, through a low pass filter to suppress the effects of AWGN and power fluctuations. The filtered signal power can be represented by

$$\hat{p}^{(i)}(n) = \sum_{l=0}^{L_f} f(l) p^{(i)}(n-l), \tag{3.26}$$

where L_f and $f(l)$ are the order and coefficient of the low pass filter, respectively.

The time-averaged approximation of the auto-covariance function can then be calculated by collecting the filtered signal power from M consecutive OFDM symbols, and the

result is

$$\hat{V}_{|y|^2|y|^2}(s-u=l,m)=\frac{1}{(M-k)(N-m)}\sum_{i=1}^{M-l}\sum_{n=0}^{N-m-1}[\hat{p}^{(i+l)}(n+m)-\bar{p}][\hat{p}^{(i)}(n)-\bar{p}] \quad (3.27)$$

where $\bar{p}=\frac{1}{MN}\sum_{i=1}^{M}\sum_{n=0}^{N-1}\hat{p}^{(i)}(n)$ is the time average of the signal power.

In addition to the auto-covariance function, another key parameter required for Doppler spread estimation is the integer k as shown in (3.20) and (3.24). The selection of k depends on two factors: first, kz should be small such that approximations in (3.18) and (3.22) still hold; second, for a given Doppler spread f_d, or $z=2\pi f_d N_s T_s$, the normalized auto-covariance, $V_N(k,z)$, should not be too close to 1, such that enough information can be collected from $V_N(k,z)$ for Doppler spread estimation. To meet both of the two objectives, the value of k should adapt roughly according to the variation of Doppler spread. Therefore, we classify the Doppler spread into three categories, "low", "medium", and "high", and different values of k are used for each of the three categories.

Classification of Doppler spread is performed at receiver by using the normalized auto-covariance of received signal power. In (3.11), when $s=u$, we choose a value m such that $T_m=mT_s$ is less than $30\mu s$, then $J_0(2\pi f_d mT_s)\approx 1$ and $\cos(2\pi f_d mT_s\cos\theta_0)\approx 1$ even if f_d is as high as 500Hz. In this case, the auto-covariance $V_{|y|^2|y|^2}(s-u=0,m)$ tends to a constant value irrelevant to f_d. We denote this constant as $V_{|y|^2|y|^2}(T_m)$. Further, choose $s-u=k_0$, such that $T_{blk}=k_0T_{sym}\approx 5ms$, where $T_{sym}=N_sT_s$ is the time duration of one OFDM symbol including cyclic prefix and postfix. Similarly, define $V_{|y|^2|y|^2}(T_{blk})\triangleq V_{|y|^2|y|^2}(s-u=k_0,m=0)$. Then, the classification of Doppler spread can be achieved as follows

$$\frac{V_{|y|^2|y|^2}(T_{blk})}{V_{|y|^2|y|^2}(T_m)}\begin{cases}>0.95, & \text{low},\\ <0.3, & \text{high},\\ \text{otherwise}, & \text{medium}.\end{cases} \quad (3.28)$$

where the classification thresholds, 0.95 and 0.3, are chosen for illustration purpose only. Other threshold values can be obtained through optimization for different levels of "low", "high", and "medium".

Based on the Doppler spread classification given in (3.28), the value of k corresponding

to each category is

$$k = \begin{cases} 10k_0, & \text{low}, \\ k_0, & \text{medium}, \\ \lceil 0.1k_0 \rceil, & \text{high}. \end{cases} \tag{3.29}$$

The values used in (3.29) are obtained based on empirical simulation results.

With the auto-covariance function approximation in (3.27) and the values of k given in (3.29), the Doppler spread can be estimated by substituting (3.27) and (3.29) into (3.20) or (3.24) with second-order and fourth-order approximations, respectively. The practical Doppler spread estimation algorithm is summarized as follows.

Step 1: Choose $\{m, k_0, M\}$ such that $mT_s < 30\mu s, T_{blk} = k_0 T_{sym} \approx 5ms$, and $MT_{sym} < 1s$.

Step 2: Compute $V_{|y|^2|y|^2}(T_m)$ and $V_{|y|^2|y|^2}(T_{blk})$. Classify Doppler spread as "low", "medium" or "high" according to (3.28), and select k based on (3.29).

Step 3: Compute $V_{|y|^2|y|^2}(kz)$, $V_{|y|^2|y|^2}(z)$ and thus $U_N(k, z)$, then obtain Doppler spread estimations $\tilde{f}_d$ and $\hat{f}_d$ according to (3.20) and (3.24) as follows:

$$\tilde{f}_d = \begin{cases} \frac{F_1(10k_0,z)}{\pi N_s T_s,} & \text{low}, \\ \frac{F_1(k_0,z)}{\pi N_s T_s,} & \text{medium}, \\ \frac{F_1(\lceil 0.1k_0 \rceil,z)}{\pi N_s T_s,} & \text{high} \end{cases} \tag{3.30}$$

$$\hat{f}_d = \begin{cases} \frac{F_2(10k_0,z)}{\pi N_s T_s,} & \text{low}, \\ \frac{F_2(k_0,z)}{\pi N_s T_s,} & \text{medium}, \\ \frac{F_2(\lceil 0.1k_0 \rceil,z)}{\pi N_s T_s,} & \text{high} \end{cases} \tag{3.31}$$

Step 4: Take the average of $\tilde{f}_d$ and $\hat{f}_d$ in (3.30) and (3.31) as the final Doppler spread estimation $\bar{f}_d = (\hat{f}_d + \tilde{f}_d)/2$.

3.5 Simulation

In this section, the performance of the proposed Doppler spread estimation algorithm in practical OFDM systems is evaluated by performing simulations in a DVB-H system.

In the simulation, one OFDM symbol excluding cyclic prefix and postfix has a time duration of $T_u = 224\mu s$. Sampling interval is $T_s = T_u/N$, where the value of N is 2048

corresponding to the 2K-mode of DVB-H system. The lengths of the cyclic prefix and cyclic postfix are set as $N_p = N_q = N/8 = 256$. One OFDM frame consists of 68 OFDM symbols, and four frames form one super-frame. The transmit filter, $p_{_T}(\tau)$, and receive filters, $p_{_R}(\tau)$, are normalized square root raised cosine filter with roll-off factor 0.3. The power delay profile of the wireless physical fading channel has 120 uncorrelated taps with tap space being $T_s/2$. The average power of the first 40 taps ramps up linearly and the last 80 taps ramps down linearly. The equivalent T_s-spaced composite discrete-time channel, $h(n, l)$, has $L = 63$ *correlated* taps. The noise-suppression low pass filter has $L_f = 50$ taps, and $k_0 = 20$ is selected in (3.29) based on the above system configuration.

We first study the estimation performance in Rayleigh fading channel with Rice factor $K = 0$. The mean and standard deviation of the estimated Doppler spreads obtained with the proposed algorithm are shown in Fig. 3.2 for a system with 64QAM modulation. For each Doppler spread, the estimation is performed over $N_f = 24$ consecutive OFDM frames, which correspond to a time duration less than 0.5 second. It's clear from the

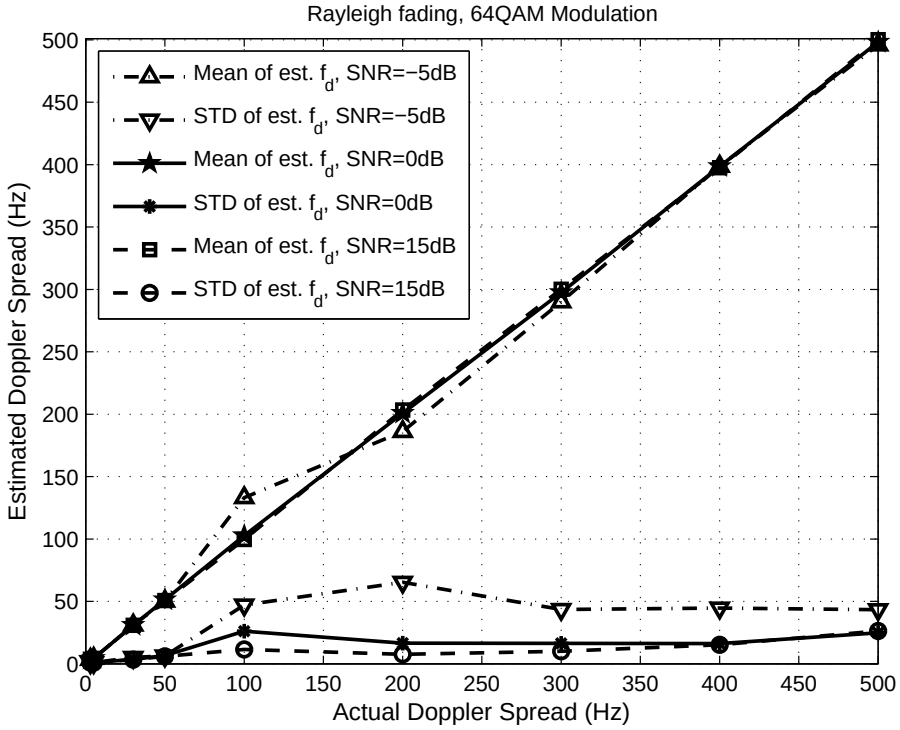

Figure 3.2: Doppler spread estimation (Rayleigh fading, 64QAM modulation).

figure that the proposed algorithm provides accurate and reliable estimation of the Doppler spread for SNR as low as 0 dB. More accurate estimations can be achieved at higher SNR. Similar observation is obtained for system with 8PSK modulation as shown in Fig. 3.3, which is obtained by using the same parameters as in Fig. 3.2 except the modulation scheme. Comparing Figs. 3.2 and 3.3 we conclude that the proposed estimation algorithm is insensitive to modulation schemes. In Fig. 3.4, the standard deviation (STD) of estimated

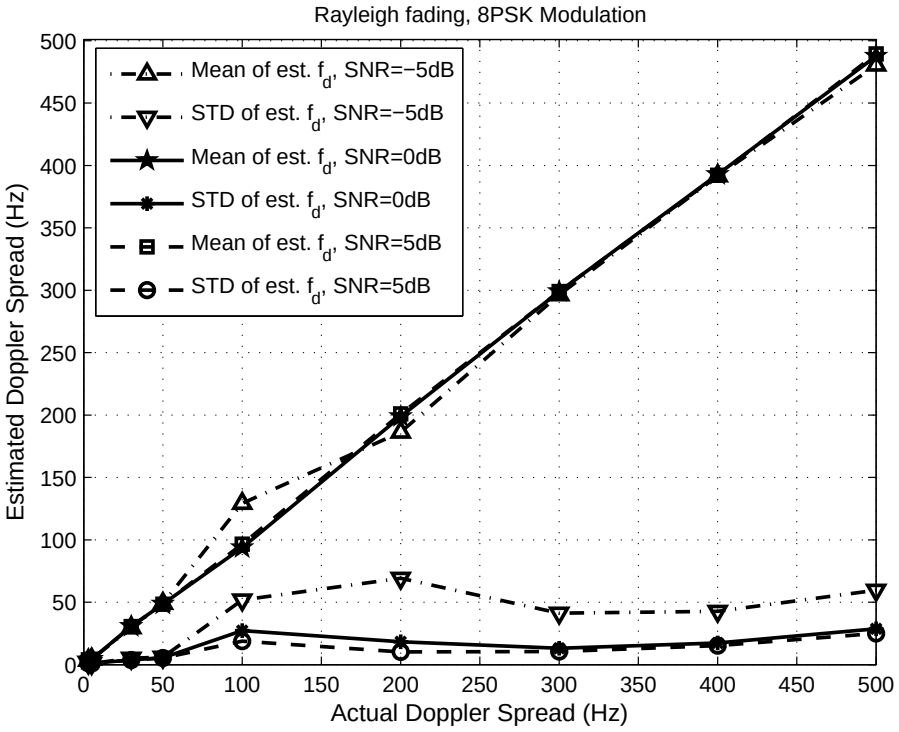

Figure 3.3: Doppler spread estimation (Rayleigh fading, 8PSK modulation).

Doppler spreads is plotted as a function of the number of OFDM frames, N_f, used in one estimation. As expected, the estimation standard deviation decreases when more OFDM frames are used during estimation. This is intuitive because more frames lead to a better time-averaged approximation of the auto-covariance function. The simulation results for Rician fading with 64QAM modulations are presented in Fig. 3.5. The Rice factor is fixed at $K = 5$, and the Rician channel simulator in [46] is used for the generation of Rician fading during simulation. Comparing the results in Figs. 3.2 and 3.5, we can see that the

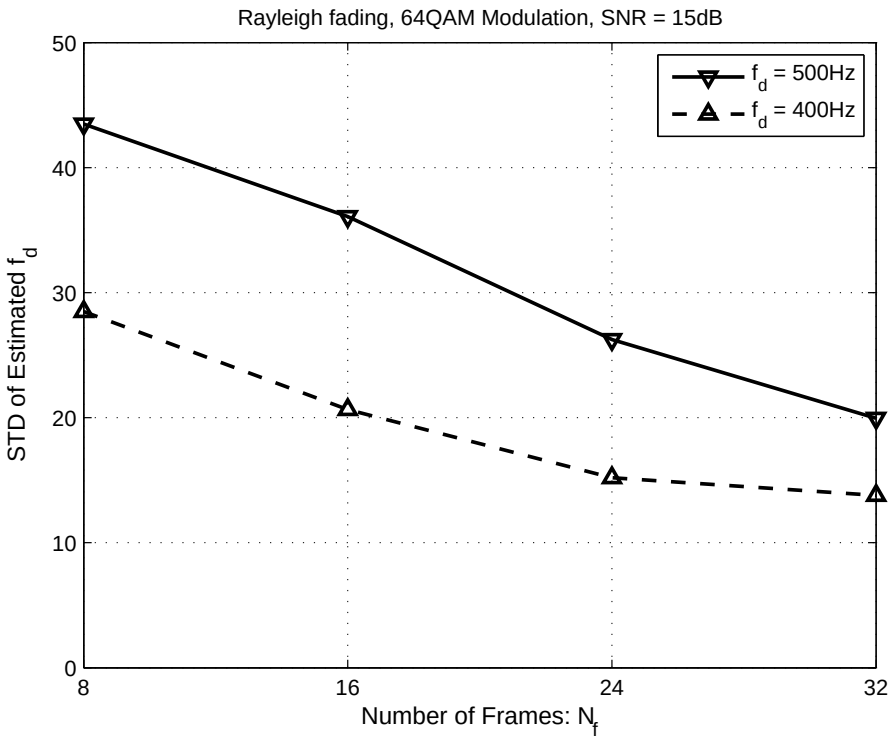

Figure 3.4: STD v.s. number of frames (Rayleigh fading, 64QAM modulation).

estimation accuracy in Rician fading channel is slightly worse compared to the Rayleigh case. The performance difference is mainly contributed by the approximations of $\cos(x)$ and $\cos^2(\theta_0)$ used in the derivation of (3.18) and (3.22) for Rician fading channel, yet these approximations are not necessary for Doppler spread estimation in Rayleigh fading channel. Even though the estimation accuracy in Rician fading channel is slightly worse compared to the Rayleigh case, the algorithm can still obtain a very accurate estimation of the Doppler spread, and the estimation accuracy increases with the increase of SNR as expected. Similar results are obtained for system with other modulation schemes, and this corroborates that the proposed method is insensitive to modulation schemes. The impact of Rice factor on the performance of the estimation algorithm is investigated in Fig. 3.6, where the standard deviation of the estimated Doppler spread is shown as a function of Rice factor K at different values of Doppler spread. 8PSK modulation is used in this example. It can be seen from the figure that the estimation accuracy degrades gradually

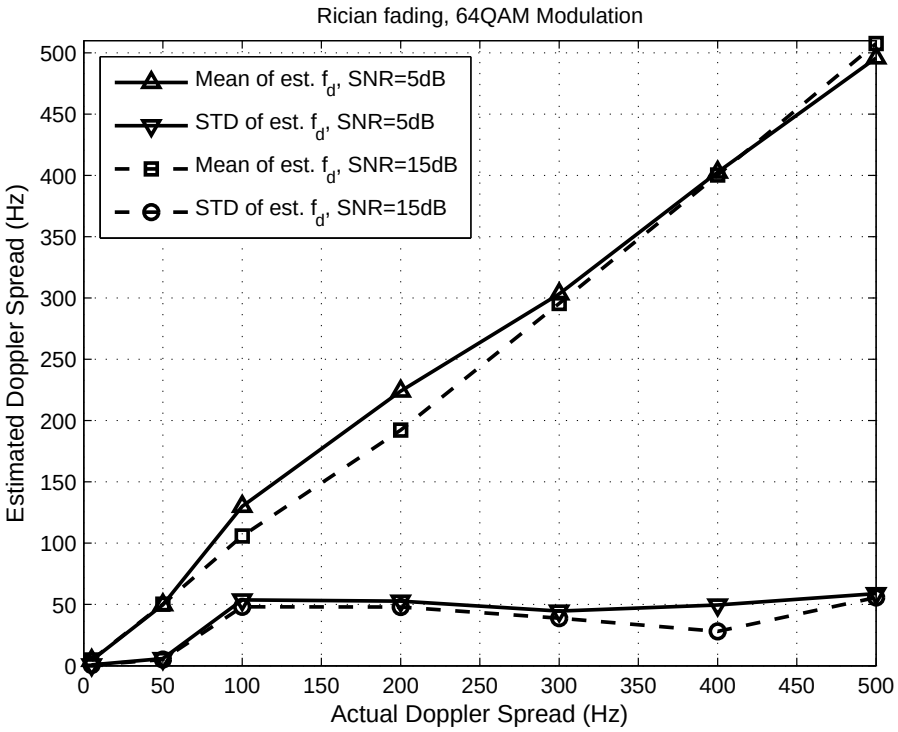

Figure 3.5: Doppler spread estimation (Rician fading, 64QAM modulation).

with the increase of K. As analyzed before, the performance degradation is mainly due to extra approximations involved in the LOS component of the fading during the estimation process.

3.6 Conclusion

An accurate low latency Doppler spread estimation algorithm was presented in this chapter for OFDM systems with fast time-varying frequency-selective Rayleigh and Rician fading. The algorithm doesn't require pilots in the transmitted signal, and was developed by analyzing the statistical properties of received signals containing unknown transmitted data symbols and unknown channel fading. The estimation is performed with the auto-covariance function of the power of the received time domain signals. Since the algorithm operates in the time domain, its performance is not affected by the ICI induced by the time variation of fading channel within one OFDM symbol. In addition, a practical algorithm

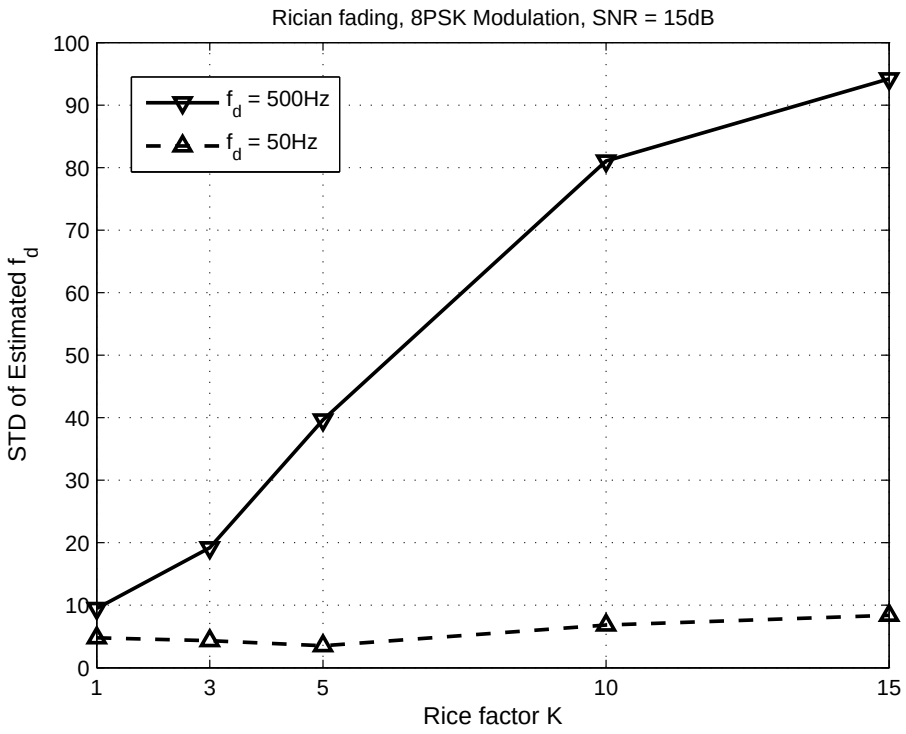

Figure 3.6: Standard deviation v.s. Rice factor K (8PSK modulation).

was proposed for accurate and high efficiency Doppler estimation. Extensive simulations have shown that the new algorithm works well for doubly-selective Rayleigh and Rician fading channels at SNR as low as 0 dB.

Chapter 4

Channel Estimation for OFDM Systems with CFO and Phase Noise

4.1 Introduction

As mentioned in Chapter 3, OFDM system has emerged as one of the most promising communication technologies for both wireless and wireline communications [13] – [19]. OFDM achieves broadband communication by multiplexing a large number of narrow-band data streams onto mutually orthogonal subcarriers via fast Fourier transform (FFT). The adoption of FFT greatly reduces the implementation cost due to the advancement in digital signal processing (DSP) and very large scale integrated circuit (VLSI). Compared to single carrier system, OFDM has higher spectral efficiency and is less sensitive to intersymbol interference (ISI). However, the performance of OFDM system is very sensitive to carrier frequency offset (CFO) and phase noise. CFO is caused by Doppler shift, and/or frequency mismatch between oscillators at transmitter and receiver; phase noise is the phase difference between carrier and local oscillator (LO) [47]. The CFO and phase noise, if not properly estimated and compensated, will cause amplitude reduction and phase drift in equalized symbols, and introduce inter-carrier interference (ICI), thus degrade the performance of OFDM systems [48] – [57].

CFO and phase noise estimations for OFDM system have attracted considerable attentions during the past decade [48] – [57]. A large number of algorithms have been developed for CFO estimation, where CFO can be estimated by utilizing either specially designed

training symbols [48], [49], redundant information contained in cyclic prefix (CP) [50], [51], or null subcarriers embedded in one OFDM symbol [52], [53]. Works on phase noise estimation and suppression for OFDM systems can be found in [54] – [57]. In [54], a carrier recovery (CR) scheme is performed in the time domain with the aid of CR pilot tones for the estimation and compensation of phase noise. In [55] and [56], phase noise is estimated by using a parametric frequency-domain model of the received OFDM signal. In [57], phase noise cancellation is achieved via approximate probabilistic inference.

The proper operation of coherent OFDM system demands the joint estimation of CFO, phase noise, and channel state information. In [58], the CFO is estimated and compensated before channel estimation, and phase noise is suppressed by passing the estimated channel impulse response through a low-pass filter originally designed for additive noise suppression. In [59], joint CFO and channel estimation for MIMO OFDM system is performed by relying on null-subcarrier and non-zero pilot symbols hopping from block to block. This specifically designed pilot pattern enables the decoupling of CFO estimation and channel estimation. However, the optimum solution in [59] requires exhaustive line search, which leads to high computational complexity. The CFO, timing error and channel impulse response (CIR) for a multiuser orthogonal frequency division multiple access (OFDMA) uplink transmission are estimated in [60] with maximum likelihood (ML) criterion. Again, the ML solution in [60] requires exhaustive search over a multi-dimensional grid spanned by CFOs and timing errors from multiple users. Even though simplifications can be performed to reduce the search effort for the optimum solutions, the computational complexity is still high. A joint CFO/phase noise/CIR estimator (JCPCE) is presented in [61]. Similar to [59] and [60], the JCPCE suffers from high computational complexity due to the non-closed-form estimation of CFO. To reduce the complexity of JCPCE, a modified JCPCE (MJCPCE) algorithm with closed-form CFO estimation is developed in [61] by adopting a special training symbol structure as proposed in [48]. The MJCPCE algorithm requires the knowledge of channel length, which is usually not available at receiver before channel estimation. In addition, its practical value is seriously limited by the fact that it can only

estimate CFO with value less than the frequency space between two adjacent subcarriers.

We present in this chapter an enhanced algorithm for the efficient estimation of CFO, phase noise, and channel state information. The new algorithm doesn't suffer from any of the aforementioned limitations. The CFO estimation is developed by exploring the time-frequency properties of two consecutive training symbols with structures similar to those used in [49]. The new method renders an accurate estimation of CFO in the presence of both unknown frequency selective fading and phase noise. More importantly, the CFO can take arbitrary values, as against the limitation imposed by MJCPCE that CFO must be less than the subcarrier space [61]. With the estimated CFO, the phase noise and frequency selective fading are jointly estimated based on the maximum *a posteriori* (MAP) criterion. In particular, the channel is estimated in terms of frequency-domain channel transfer function (CTF), and it is different from the time-domain CIR estimation method used in MJCPCE. The adoption of CTF instead of CIR leads to an estimator with lower complexity and better accuracy. In addition, it eliminates the requirement for *a priori* knowledge of channel length, which is usually unavailable at receiver before channel estimation. The Cramer-Rao lower bound (CRLB) for the mean square error (MSE) of CTF estimation is derived to benchmark the performance of the proposed algorithm. Simulation results show that the new channel estimator can achieve a performance close to CRLB.

The remainder of this chapter is organized as follows. In Section 4.2, an OFDM system model with CFO and phase noise distortion is presented. In Section 4.3, a CFO estimation method is first developed by exploring the time-frequency structure of the training symbols, then a joint phase noise and CTF estimation algorithm is developed based on the CFO-compensated signals. Simulation results are presented in Section 4.5, and Section 4.6 concludes the chapter.

4.2 System Model

Baseband OFDM signal can be obtained by performing normalized inverse discrete Fourier transform (IDFT) on a group of modulated symbols, $s = \left[s_0, s_1, \cdots, s_{N-1}\right] \in \mathcal{C}^{1\times N}$, at the transmitter, as

$$x_n = \frac{1}{\sqrt{N}} \sum_{k=0}^{N-1} s_k e^{j2\pi \frac{kn}{N}}, -N_p \leq n < N \tag{4.1}$$

where N is the number of subcarriers, $N_p \geq L$ is the length of cyclic prefix (CP), with L being the length of the equivalent discrete-time CIR, $\{h_l\}_{l=0}^{L-1}$. The adoption of CP removes ISI, and it enables the conversion of linear channel convolution to circular convolution, which leads to simple equalization at receiver.

We consider slow frequency selective fading in this chapter. The CIR is assumed to be constant over one slot duration, which contains two OFDM training symbols followed by multiple OFDM data symbols [61]. The OFDM training symbol is generated by alternatively transmitting pilot symbols and zeros in the frequency domain. Without loss of generality, it is assumed that $N/2$ pilot symbols are transmitted on the even-indexed subcarriers and zeros on the odd-indexed subcarriers. The time-domain representation of the OFDM training symbol can then be expressed as

$$x_n = \frac{1}{\sqrt{N/2}} \sum_{k=0}^{N/2-1} s_{2k} e^{j2\pi \frac{kn}{N/2}}, -N_p \leq n < N \tag{4.2}$$

where $\{s_{2k}\}_{k=0}^{N/2-1}$ are pilot symbols, and the normalization factor, $\frac{1}{\sqrt{N/2}}$, is used in (4.2) to maintain constant OFDM symbol energy. The transmission of zeros on odd-indexed subcarriers results in a $\frac{N}{2}$-point IDFT in (4.2). In addition, it is clear from (4.2) that the time-domain OFDM training symbol has two identical halves, *i.e.*, $\{x_n\}_{n=0}^{N/2-1}$ is exactly the same as $\{x_n\}_{n=N/2}^{N-1}$. This property of the training symbol will be exploited to assist CFO estimation.

At the receiver, after the removal of CP, we have the time-domain samples of the

received OFDM training symbol as

$$\begin{aligned} y_n &= e^{j\left(2\pi\frac{n\epsilon}{N}+\phi_n\right)}\left(h_n \otimes x_n\right) + v_n \\ &= e^{j\left(2\pi\frac{n\epsilon}{N}+\phi_n\right)}\frac{1}{\sqrt{N/2}}\sum_{k=0}^{N/2-1} s_{2k} H_{2k} e^{j2\pi\frac{kn}{N/2}} + v_n \end{aligned} \tag{4.3}$$

where $n = 0, 1, \cdots, N-1$, $\otimes$ denotes circular convolution, v_n is the additive white Gaussian noise (AWGN) with variance σ^2, ϵ is the CFO normalized with respect to subcarrier space $\frac{1}{NT_s}$, with T_s being the sampling period at receiver, ϕ_n is the phase noise distortion, and the frequency-domain CTF, H_{2k}, is defined as

$$H_{2k} = \sum_{l=0}^{L-1} h_l e^{-j2\pi\frac{2kl}{N}},\ 0 \le k \le N/2-1. \tag{4.4}$$

It should be noted that the circular convolution in the first equality of (4.3) is due to the insertion of the CP, and the relationship described in (4.3) is valid as long as $N_p \geq L$.

Define $\mathbf{E} = \text{diag}\left\{1, e^{j2\pi\epsilon/N}, \cdots, e^{j2\pi(N-1)\epsilon/N}\right\}$, $\mathbf{P} = \text{diag}\left\{e^{j\phi_0}, e^{j\phi_1}, \cdots, e^{j\phi_{N-1}}\right\}$, $\mathbf{S} = \text{diag}\left\{s_0, s_2, \cdots, s_{N-2}\right\}$ and $\mathbf{H} = \left[H_0, H_2, \cdots, H_{N-2}\right]^t$, then (4.3) can be represented in matrix format as

$$\mathbf{y} = \mathbf{E}\mathbf{P}\tilde{\mathbf{F}}^h\mathbf{S}\mathbf{H} + \mathbf{v} \tag{4.5}$$

where $\mathbf{y} = \left[y_0, y_1, \cdots, y_{N-1}\right]^t$, $\mathbf{v} = \left[v_0, v_1, \cdots, v_{N-1}\right]^t$, $(\cdot)^t$ and $(\cdot)^h$ stand for transpose and Hermitian transpose, respectively, and $\tilde{\mathbf{F}} = \left[\mathbf{F}_{N/2}, \mathbf{F}_{N/2}\right] \in \mathcal{C}^{\frac{N}{2}\times N}$ with $\mathbf{F}_{N/2}$ being the $\frac{N}{2}$-point DFT matrix. The (k,l)-th element of $\mathbf{F}_{N/2}$ is $\left(\mathbf{F}_{N/2}\right)_{k,l} = \frac{1}{\sqrt{N/2}} e^{-\frac{j2\pi(k-1)(l-1)}{N/2}}$.

The statistical properties of phase noise depend on specific receiver implementations [47]. For receiver equipped with a phase-locked loop (PLL), the phase noise can be modeled as a zero-mean colored stationary Gaussian process [47]. When the system is only frequency-locked, the phase noise is modeled as a zero-mean, nonstationary Wiener process [62]. Since PLL is necessary for a coherent receiver, the stationary Gaussian process model, which has been extensively used in the literature [54, 57, 61, 63], is adopted in this chapter. In this case, $\boldsymbol{\phi} = \left[\phi_0, \phi_1, \cdots, \phi_{N-1}\right]^t$ has a multivariate Gaussian distribution of $\boldsymbol{\phi} \sim \mathcal{N}\left(\mathbf{0}_N, \mathbf{R}_\phi\right)$, where the mean vector, $\mathbf{0}_N$, is a size $N \times 1$ all zero vector, and $\mathbf{R}_\phi$ is

the covariance matrix of $\boldsymbol{\phi}$. The value of $\mathbf{R}_{\phi}$ can be calculated with the specifications of phase-locked voltage controlled oscillator (VCO) [62].

4.3 Development of Estimation Algorithm

In this section, the CFO estimation exploring the time-frequency structure of the training symbols, is first discussed. After that, a joint channel estimation and phase noise suppression method using MAP criteria is developed, with the CFO-compensated signal.

4.3.1 CFO Estimation in The Presence of Fading and Phase Noise

Based on the training symbol property, $x_n = x_{n+N/2}$, for $n = 0, \cdots, N/2-1$, the received time-domain training samples, y_n and $y_{n+N/2}$, are the same except a phase difference, in the absence of additive noise and phase noise [c.f. (4.3)],

$$y_n^* y_{n+N/2} = |y_n|^2 e^{j\pi\epsilon}. \tag{4.6}$$

Obviously, (4.6) is a periodic function of ϵ with period $2z$, where z is an integer. Thus, the CFO can be estimated by measuring the phase difference between $\mathbf{y}_1 = \left[y_0, y_1, \cdots, y_{N/2-1}\right]^t$ and $\mathbf{y}_2 = \left[y_{N/2}, y_{N/2+1}, \cdots, y_{N-1}\right]^t$, up to an ambiguity, $2z$. In [61], CFO estimation with additive noise and phase noise rejection is performed in the time domain by measuring the phase difference between $\mathbf{y}_1$ and $\mathbf{y}_2$, and the result can be written as

$$\hat{\epsilon} = \frac{1}{\pi} \measuredangle \left[\mathbf{y}_1^h (\mathbf{Y}_1 \mathbf{R}_{\Delta} \mathbf{Y}_1^h + 2\sigma^2 \mathbf{I}_{N/2})^{-1} \mathbf{y}_2\right] \tag{4.7}$$

where $\measuredangle a \in (-\pi, \pi]$ returns the phase of the complex-valued number a, $\mathbf{Y}_1 = \mathrm{diag}\{\mathbf{y}_1\}$ with $\mathrm{diag}\{\mathbf{a}\}$ being a diagonal matrix with the vector $\mathbf{a}$ on its diagonal, $\mathbf{I}_{N/2}$ is a size $N/2$ identity matrix, and $\mathbf{R}_{\Delta} = 2\mathbf{R}_{N/2} - \boldsymbol{\Upsilon} - \boldsymbol{\Upsilon}^t$, with $\mathbf{R}_{N/2} \in \mathcal{C}^{\frac{N}{2}\times\frac{N}{2}}$ and $\boldsymbol{\Upsilon} \in \mathcal{C}^{\frac{N}{2}\times\frac{N}{2}}$ being sub-matrices of $\mathbf{R}_{\phi}$ expressed as follows

$$\mathbf{R}_{\phi} = \begin{bmatrix} \mathbf{R}_{N/2} & \boldsymbol{\Upsilon} \\ \boldsymbol{\Upsilon}^t & \mathbf{R}_{N/2} \end{bmatrix}. \tag{4.8}$$

The CFO estimation described in (4.7) implies that the estimated CFO satisfies $|\hat{\epsilon}| < 1$. When the actual CFO is larger than subcarrier space, or $|\epsilon| > 1$, it fails to solve the ambiguity $2z$ with z being a nonzero integer, as indicated by (4.6). In other words, if we denote CFO as $\epsilon = \epsilon_0 + 2z$ with $|\epsilon_0| < 1$, then only the fractional CFO, ϵ_0, is estimated from (4.7).

We propose to estimate the integer part of the CFO, $2z$, in the frequency domain by utilizing two consecutive OFDM training symbols. From (4.3), the received samples of the first and second OFDM training symbols can be written as

$$y_{1,n} = \sqrt{\frac{2}{N}} e^{j2\pi \frac{n\epsilon}{N}} e^{j\phi_n} \sum_{k=0}^{N/2-1} s_{1,2k} H_{2k} e^{j2\pi \frac{kn}{N/2}} + v_{1,n} \tag{4.9a}$$

$$y_{2,n} = \sqrt{\frac{2}{N}} e^{j2\pi \frac{(n+N+N_p)\epsilon}{N}} e^{j\phi_{n+N+N_p}} \sum_{k=0}^{N/2-1} s_{2,2k} H_{2k} e^{j2\pi \frac{kn}{N/2}} + v_{2,n} \tag{4.9b}$$

where $n = 0, 1, \cdots, N-1$ for both $y_{1,n}$ and $y_{2,n}$. The ratio of the two training sequences, $\{s_{1,2k}\}_{k=0}^{N/2-1}$ and $\{s_{2,2k}\}_{k=0}^{N/2-1}$, is set to be equal to a predefined pseudo-noise (PN) sequence $\{\alpha_k\}_{k=0}^{N/2-1}$, *i.e.*, $s_{2,2k}/s_{1,2k} = \alpha_k$.

Fractional CFO, ϵ_0, is estimated with (4.7) and then compensated in $y_{1,n}$ and $y_{2,n}$, respectively, and it leads to the following approximation

$$\hat{y}_{1,n} \approx \sqrt{\frac{2}{N}} \sum_{k=0}^{N/2-1} s_{1,2k} H_{2k} e^{j2\pi \frac{(k+z)n}{N/2}} + \hat{v}_{1,n} \tag{4.10a}$$

$$\hat{y}_{2,n} \approx \sqrt{\frac{2}{N}} e^{j4\pi \frac{zN_p}{N}} \sum_{k=0}^{N/2-1} s_{2,2k} H_{2k} e^{j2\pi \frac{(k+z)n}{N/2}} + \hat{v}_{2,n} \tag{4.10b}$$

where $\hat{v}_{1,n}$ and $\hat{v}_{2,n}$ are the noise components after fractional CFO compensation, and the approximation, $e^{j\left[\phi_n + 2\pi n(\epsilon_0 - \hat{\epsilon}_0)/N\right]} \approx 1$, is used in the above equations based on the fact that the combined disturbance of phase noise and residual CFO are usually small in practice [54]. It should be noted that the approximation used in (4.10) is only for the convenience of integer CFO estimation. The actual phase noise will be estimated and compensated during channel estimation described in the next subsection. It'll be shown in simulation that the integer CFO $2z$ can be accurately estimated even with the approximation used in (4.10).

The estimation of $2z$ is performed in the frequency domain. Performing N-point DFT on $\hat{y}_{1,n}$ and $\hat{y}_{2,n}$ leads to

$$\hat{Y}_{1,k} = \sqrt{2} s_{1,(k-2z)_N} H_{(k-2z)_N} + \hat{V}_{1,k} \tag{4.11a}$$

$$\hat{Y}_{2,k} = \sqrt{2} e^{j4\pi z N_p/N} s_{2,(k-2z)_N} H_{(k-2z)_N} + \hat{V}_{2,k} \tag{4.11b}$$

where $(\cdot)_N$ denotes modulus N operation, $\hat{Y}_{i,k}$ and $\hat{V}_{i,k}$ are the DFTs of $\hat{y}_{i,n}$ and $\hat{v}_{i,n}$, respectively, for $i = 1, 2$. There is a phase difference, $e^{j4\pi z N_p/N}$, between $\hat{Y}_{1,k}$ and $\hat{Y}_{2,k}$ in the frequency domain, and the phase difference is independent of the subcarrier index k. Define the metric used to estimate z as

$$\mathcal{M}(z) = \left| \sum_{k=0}^{N/2-1} \hat{Y}^*_{1,2k+2z} \alpha_k^* \hat{Y}_{2,2k+2z} \right| \tag{4.12}$$

where $(\cdot)^*$ denotes complex conjugate. With $\mathcal{M}(z)$ defined in (4.12), the estimated value of z is obtained as

$$\hat{z} = \arg \max_{z \in \mathcal{I}} \mathcal{M}(z). \tag{4.13}$$

The estimation of the CFO, $\epsilon = \epsilon_0 + 2z$, can then be expressed as $\hat{\epsilon} = \hat{\epsilon}_0 + 2\hat{z}$.

It should be noted that with the estimation method derived from (4.11) and (4.12), the value of the integer CFO, z, must satisfy $|z| < N/4$, due to the fact that both $\hat{Y}_{1,k}$ and $\hat{Y}_{2,k}$ in (4.11) are periodic functions of z with period $N/2$. In a practical OFDM system, it is reasonable to assume that the CFO (proportional to $2z$) is much less compared to OFDM signal bandwidth (proportional to N). Therefore, the additional restriction of $|z| < N/4$ can be met in most practical OFDM systems.

An alternative null-subcarrier based suboptimum integer CFO estimation algorithm was presented in [52] by transmitting zeros on not only odd subcarriers, but also part of the even subcarriers of the pilot symbol. While the method requires only one pilot symbol, the reduction in the number of non-null even-indexed subcarriers leads to inferior estimation of the overall channel impulse response. Simulation results show that the algorithm proposed in this chapter obtains a more accurate estimation of CFO compared to that in [52] at low signal-to-noise ratio (SNR).

4.3.2 Joint Phase Noise and CTF Estimation

With the estimated CFO $\hat{\epsilon}$, we are able to construct $\hat{\mathbf{E}} = \text{diag}\left\{1, e^{j2\pi\hat{\epsilon}/N}, \cdots, e^{j2\pi\hat{\epsilon}(N-1)/N}\right\}$, as the CFO compensation matrix. Multiplying both sides of (4.5) with $\hat{\mathbf{E}}^h$ leads to

$$\tilde{\mathbf{y}} = \mathbf{P}_{\text{eff}}\tilde{\mathbf{F}}^h\mathbf{S}\mathbf{H} + \tilde{\mathbf{v}} \tag{4.14}$$

where $\tilde{\mathbf{y}} = \hat{\mathbf{E}}^h\mathbf{y}$, and $\mathbf{P}_{\text{eff}} = (\Delta\mathbf{E})\mathbf{P}$ is the effective phase noise matrix after CFO compensation, with $\Delta\mathbf{E}$=diag $\left\{1, e^{j2\pi\Delta\epsilon/N}, \cdots, e^{j2\pi\Delta\epsilon(N-1)/N}\right\}$ being a phase rotation matrix due to CFO estimation error $\Delta\epsilon = \epsilon - \hat{\epsilon}$. The equivalent noise $\tilde{\mathbf{v}} = \hat{\mathbf{E}}^h\mathbf{v}$ is still AWGN with covariance matrix $\sigma^2\mathbf{I}$.

The effective phase noise matrix can be alternatively represented as $\mathbf{P}_{\text{eff}} = \text{diag}\left\{\boldsymbol{\phi}_{\text{eff}}\right\}$, where $\boldsymbol{\phi}_{\text{eff}} = \left[\phi_0, \phi_1 + 2\pi\frac{\Delta\epsilon}{N}, \cdots, \phi_{N-1} + 2\pi\frac{\Delta\epsilon(N-1)}{N}\right]^t$. The vector $\boldsymbol{\phi}_{\text{eff}}$ has a multivariate Gaussian distribution of $\boldsymbol{\phi}_{\text{eff}} \sim \mathcal{N}(\mathbf{0}, \mathbf{R}_{\phi_{\text{eff}}})$. The covariance matrix, $\mathbf{R}_{\phi_{\text{eff}}}$, depends on the variance of the residual CFO $\Delta\epsilon$. At high SNR, the variance of $\Delta\epsilon$ can be approximated by [48], [49]

$$\sigma^2_{\Delta\epsilon} = \frac{1}{\pi^2 \cdot (N/2) \cdot \gamma} \tag{4.15}$$

where γ denotes SNR in linear scale. Therefore, the covariance matrix of $\boldsymbol{\phi}_{\text{eff}}$ can be accurately approximated as $\mathbf{R}_{\phi_{\text{eff}}} = \mathbf{R}_{\phi} + \frac{8}{N^3\gamma}\mathbf{T}$, where $\mathbf{T} = \mathbf{b}\mathbf{b}^t$ with $\mathbf{b} = [0, 1, \cdots, N-1]^t$. Noting the fact that the scaling factor $\frac{8}{N^3\gamma}$ of $\mathbf{T}$ is inversely proportional to N^3, while the maximum element in $\mathbf{T}$ is in the order of N^2, we conclude that the effect of residual CFO on phase noise is negligible for practical values of N. As a result, it is reasonable to assume that $\boldsymbol{\phi}_{\text{eff}}$ has the same distribution as $\boldsymbol{\phi}$, *i.e.* $\boldsymbol{\phi}_{\text{eff}} \sim \mathcal{N}(\mathbf{0}, \mathbf{R}_{\phi})$. Simulation results show that the assumption of $\boldsymbol{\phi}_{\text{eff}} \sim \mathcal{N}(\mathbf{0}, \mathbf{R}_{\phi})$ is valid under both low SNR and high SNR, and it doesn't apparently affect the accuracy of the proposed channel estimation method.

The MAP criterion is adopted for the joint estimation of $\boldsymbol{\phi}_{\text{eff}}$ and $\mathbf{H}$. From (4.14). The *a posteriori* probability (APP) density of $\boldsymbol{\phi}_{\text{eff}}$ and $\mathbf{H}$ can be written as

$$p(\boldsymbol{\phi}_{\text{eff}}, \mathbf{H}|\tilde{\mathbf{y}}) = p(\tilde{\mathbf{y}}|\boldsymbol{\phi}_{\text{eff}}, \mathbf{H})p(\boldsymbol{\phi}_{\text{eff}})\, p(\mathbf{H})\, / p(\tilde{\mathbf{y}}) \tag{4.16}$$

where it is assumed that $\boldsymbol{\phi}_{\text{eff}}$ and $\mathbf{H}$ are mutually independent. In practice, the *a priori* knowledge of channel is usually unavailable, so it is reasonable to treat $\mathbf{H}$ as an unknown constant during channel estimation, thus $p(\mathbf{H}) = 1$. From (4.16), the negative log-likelihood function can be written as

$$\begin{aligned}\mathcal{L}\left(\boldsymbol{\phi}_{\text{eff}}, \mathbf{H}\right) &= -\log p\left(\boldsymbol{\phi}_{\text{eff}}, \mathbf{H}|\tilde{\mathbf{y}}\right) \\ &= -\log p\left(\tilde{\mathbf{y}}|\boldsymbol{\phi}_{\text{eff}}, \mathbf{H}\right) - \log p(\boldsymbol{\phi}_{\text{eff}}) + \log p(\tilde{\mathbf{y}}).\end{aligned} \tag{4.17}$$

Discarding irrelevant constants and noting that $p\left(\tilde{\mathbf{y}}\right)$ is irrelevant to specific values of $\boldsymbol{\phi}_{\text{eff}}$ and $\mathbf{H}$, we define the cost function for the MAP criterion as

$$\mathcal{J}\left(\boldsymbol{\phi}_{\text{eff}}, \mathbf{H}\right) = \frac{1}{\sigma^2}\left\|\tilde{\mathbf{y}} - \mathbf{P}_{\text{eff}}\tilde{\mathbf{F}}^h\mathbf{S}\mathbf{H}\right\|^2 + \frac{1}{2}\boldsymbol{\phi}_{\text{eff}}{}^t\mathbf{R}_{\phi}^{-1}\boldsymbol{\phi}_{\text{eff}} \tag{4.18}$$

where $\|\mathbf{a}\|^2 = \mathbf{a}^h\mathbf{a}$ for a column vector $\mathbf{a}$.

Solving $\partial\mathcal{J}\left(\boldsymbol{\phi}_{\text{eff}}, \mathbf{H}\right)/\partial\mathbf{H}^* = 0$ leads to the optimal estimation of the CTF vector, $\mathbf{H}$, as

$$\hat{\mathbf{H}} = \frac{1}{2}\mathbf{S}^{-1}\tilde{\mathbf{F}}\mathbf{P}_{\text{eff}}^h\tilde{\mathbf{y}}. \tag{4.19}$$

The solution in (4.19) requires the knowledge of the effective phase noise matrix $\mathbf{P}_{\text{eff}}$. When $\mathbf{P}_{\text{eff}}$ is ideally estimated, the channel estimator given by (4.19) is a minimum variance unbiased estimator (MVUE) for $\mathbf{H}$ [64].

To estimate $\mathbf{P}_{\text{eff}}$, substituting (4.19) into (4.18) yields

$$\mathcal{J}\left(\boldsymbol{\phi}_{\text{eff}}\right) = \frac{1}{\sigma^2}\mathbf{p}^t\mathbf{B}\mathbf{p}^* + \frac{1}{2}\boldsymbol{\phi}_{\text{eff}}{}^t\mathbf{R}_{\phi}^{-1}\boldsymbol{\phi}_{\text{eff}} \tag{4.20}$$

where $\mathbf{p} = e^{j\boldsymbol{\phi}_{\text{eff}}}$, $\mathbf{B} = \tilde{\mathbf{Y}}^h\left(\mathbf{I}_N - \frac{1}{2}\tilde{\mathbf{F}}^h\tilde{\mathbf{F}}\right)\tilde{\mathbf{Y}}$, and $\tilde{\mathbf{Y}} = \text{diag}\left\{\tilde{\mathbf{y}}\right\}$. Using the approximation of $\mathbf{p} = e^{j\boldsymbol{\phi}_{\text{eff}}} \approx \mathbf{1}_N + j\boldsymbol{\phi}_{\text{eff}}$ for small $\boldsymbol{\phi}_{\text{eff}}$ [54], and solving $\partial\mathcal{J}\left(\boldsymbol{\phi}_{\text{eff}}\right)/\partial\boldsymbol{\phi}_{\text{eff}} = 0$, we have the optimal estimation of $\boldsymbol{\phi}_{\text{eff}}$ as

$$\hat{\boldsymbol{\phi}}_{\text{eff}} = \left[\text{Re}\left(\mathbf{B}\right) + \left(\sigma^2/2\right)\mathbf{R}_{\phi}^{-1}\right]^{-1}\text{Im}\left(\mathbf{B}\right)\mathbf{1}_N \tag{4.21}$$

where $\text{Re}(\cdot)$ and $\text{Im}(\cdot)$ are the real part and imaginary part operators, respectively, and $\mathbf{1}_N$ denotes an $N \times 1$ all-one column vector. Obviously, the estimation of $\hat{\boldsymbol{\phi}}_{\text{eff}}$ is independent

of the modulation data matrix $\mathbf{S}$, which, on the other hand, is required by the MJCPCE method in [61]. The independence of the estimation on $\mathbf{S}$ leads to a much simpler form of estimator, which requires less computational complexity and no *a priori* knowledge of transmitted modulation symbols, compared to the phase noise estimator provided by MJCPCE method.

The estimated value of $\hat{\boldsymbol{\phi}}_{\text{eff}}$ can then be substituted back into (4.19) to obtain an estimate of the CTF vector $\hat{\mathbf{H}}$. Eqn. (4.19) provides estimation of $\mathbf{H} \in \mathcal{C}^{\frac{N}{2}\times 1}$, which is the CTF of even-indexed subcarriers. The estimation of normalized CTF on all subcarriers can be calculated from $\hat{\mathbf{H}}$ as

$$\hat{\mathbf{H}}_{\text{full}} = \sqrt{2/N}\mathbf{F}_{N}\left[\left(\mathbf{F}_{N/2}^{h}\hat{\mathbf{H}}\right)^{t}\mathbf{0}_{N/2}^{t}\right]^{t} \tag{4.22}$$

where $\mathbf{F}_{N}$ is the N-point normalized DFT matrix with the (k,l)-th element being $(\mathbf{F}_{N})_{k,l} = \frac{1}{\sqrt{N}}e^{-j2\pi(k-1)(l-1)/N}$, $\mathbf{F}_{N/2}$ is the $\frac{N}{2}$-point normalized DFT matrix, and $\mathbf{0}_{N/2}$ is an all zero column vector with size $N/2$. Furthermore, the time-domain CIR, $\mathbf{h} = [h_0, h_1, \cdots, h_{L-1}]^t$, can be estimated by performing IDFT over the estimated CTF vector $\hat{\mathbf{H}}$ as [c.f. (4.4)]

$$\hat{\mathbf{h}} = \sqrt{2/N}\mathbf{F}_{1:L}^{h}\hat{\mathbf{H}} \tag{4.23}$$

where $\mathbf{F}_{1:L} \in \mathcal{C}^{\frac{N}{2}\times L}$ contains the first L columns of the $\frac{N}{2}$-point DFT matrix $\mathbf{F}_{N/2}$. In case that the channel length L is unknown, the matrix $\mathbf{F}_{1:L}$ can be replaced by $\mathbf{F}_{N/2}$. Replacing $\mathbf{F}_{1:L}$ with $\mathbf{F}_{N/2}$ leads to an estimated CIR with $N/2$ channel taps, where the first L channel taps are exactly the same as those estimated by using $\mathbf{F}_{1:L}$, and the remaining $N/2 - L$ channel taps contain pure noise. In this case, the estimation accuracy can be improved by either directly discarding channel taps with negligible power [65], or applying noise reduction algorithm [66].

Compared to the MJCPCE method presented in [61], the algorithm proposed in this chapter has three main advantages. First, the new algorithm can accurately estimate CFO with arbitrary values, while the method in [61] can only estimate CFO with value less than subcarrier space. Second, estimating the frequency-domain CTF instead of the time-domain CIR leads to a simpler estimator with lower computational complexity. Third,

the knowledge of channel length L is not required during CTF estimation, whereas the estimation procedure in [61] depends on L. The estimation method discussed above can be easily extended to single input multiple output (SIMO) system with independent CFO, phase noise and fading channel on different receive antenna.

4.4 CRLB for OFDM Channel Estimation

The CRLBs of the mean square error for the estimation of the frequency-domain CTF, $\mathbf{H}$ and $\mathbf{H}_{\text{full}}$, and the time-domain CIR, $\mathbf{h}$, are derived in this section.

In the absence of CFO and phase noise, the log likelihood function, $\log p(\mathbf{y}|\mathbf{H})$, can be calculated from (4.5) as

$$\log p\left(\mathbf{y}|\mathbf{H}\right) = c - \frac{1}{\sigma^2}\left(\mathbf{y} - \tilde{\mathbf{F}}^h\mathbf{S}\mathbf{H}\right)^h\left(\mathbf{y} - \tilde{\mathbf{F}}^h\mathbf{S}\mathbf{H}\right) \tag{4.24}$$

where c is a constant independent of $\mathbf{y}$ and $\mathbf{H}$. The CRLB for the estimation of $\mathbf{H}$ can then be calculated as

$$\begin{aligned}\text{CRLB}\left(\mathbf{H}\right) &= \text{tr}\left\{\left[\mathbb{E}\left\{\left[\frac{\partial}{\partial\mathbf{H}^*}[\log p(\mathbf{y}|\mathbf{H})]\right]\left[\frac{\partial}{\partial\mathbf{H}^*}[\log p(\mathbf{y}|\mathbf{H})]\right]^h\right\}\right]^{-1}\right\} \\ &= \frac{\sigma^2}{2}\text{tr}\left\{\left\{\mathbb{E}\left[\mathbf{S}^h\mathbf{S}\right]\right\}^{-1}\right\}\end{aligned} \tag{4.25}$$

where $\text{tr}\{\cdot\}$ denotes trace of a square matrix, and $\mathbb{E}\{\cdot\}$ denotes mathematical expectation. Based on (4.22) and (4.25), it is easy to obtain the CRLB for the estimation of normalized $\mathbf{H}_{\text{full}}$ as

$$\text{CRLB}\left(\mathbf{H}_{\text{full}}\right) = \frac{2}{N}\times\text{CRLB}\left(\mathbf{H}\right) = \frac{\sigma^2}{N}\text{tr}\left\{\left\{\mathbb{E}\left[\mathbf{S}^h\mathbf{S}\right]\right\}^{-1}\right\}. \tag{4.26}$$

Similarly, from (4.23) and (4.25), the CRLB for the estimation of the CIR vector $\mathbf{h}$ is obtained as

$$\text{CRLB}\left(\mathbf{h}\right) = \frac{\sigma^2}{N}\text{tr}\left\{\left\{\mathbf{F}_{1:L}^H\mathbb{E}\left[\mathbf{S}^h\mathbf{S}\right]\mathbf{F}_{1:L}\right\}^{-1}\right\}. \tag{4.27}$$

If the modulation symbols are equiprobable and independent, *i.e.*, $\mathbb{E}\left[\mathbf{S}^h\mathbf{S}\right] = \sigma_s^2\mathbf{I}$, then (4.26) and (4.27) can be simplified to

$$\text{CRLB}\left(\mathbf{H}_{\text{full}}\right) = \frac{1}{2}\cdot\frac{\sigma^2}{\sigma_s^2} \tag{4.28}$$

$$\mathrm{CRLB}\left(\mathbf{h}\right) = \frac{L}{N} \cdot \frac{\sigma^2}{\sigma_s^2}. \tag{4.29}$$

We conclude this section by the following two remarks.

Remark 1: From (4.28) and (4.29), we find $\mathrm{CRLB}(\mathbf{H}_{\text{full}}) \neq \mathrm{CRLB}(\mathbf{h})$ when $N \neq 2L$. The difference is due to the fact that the estimation of $\mathbf{h}$ in (4.23) depends on the knowledge of channel length L, while $\mathbf{H}_{\text{full}}$ is estimated without the knowledge of L.

Remark 2: From (4.19), the channel estimation MSE can be evaluated as

$$\mathbb{E}\left[\left\|\mathbf{H} - \hat{\mathbf{H}}\right\|^2\right] = \frac{\sigma^2}{2}\mathrm{tr}\left\{\mathbb{E}\left[\left(\mathbf{S}\mathbf{S}^h\right)^{-1}\right]\right\} \tag{4.30}$$

which is equal to CRLB given by (4.25) when constant modulus modulation scheme, such as phase shift keying, is adopted. In other words, if $\mathbf{P}_{\text{eff}}$ is ideally estimated, then CRLB for the estimation of $\hat{\mathbf{H}}$ can be achieved for systems with constant modulus modulation. On the other hand, for non-constant modulus modulation scheme, the MSE in (4.30) is always larger than the CRLB bound in (4.25). This means that, even the obtained estimator is still MVUE, the CRLB can never be reached for system with non-constant modulus modulations. Therefore, in terms of channel estimation, constant modulus modulation schemes are preferable compared to non-constant modulus modulation schemes under the same energy constraint.

4.5 Simulation

Simulation results are presented in this section to verify the performance of the proposed algorithm. System parameters similar to those used in [61] are adopted here for comparison purpose: the number of subcarriers is $N = 64$, and the system sampling rate is $f_s = 20$MHz, leading to a subcarrier space of $\Delta f = f_s/N = 312.5$KHz. Phase noise is simulated by passing a white Gaussian process through a one-pole Butterworth low-pass filter with 3dB bandwidth $f_o = 100$KHz. The covariance matrix of phase noise $\mathbf{R}_\phi$ is calculated as $\left(\mathbf{R}_\phi\right)_{m,n} = \left(\pi\phi_{\text{rms}}/180\right)^2 \exp\left\{-2\pi f_o|m-n|/f_s\right\}$. Fractional CFO ϵ_0 is generated as a uniform distribution over (-1,1), and integer CFO z is taken randomly from $[-z_m, z_m]$

with $|z_m| < N/4$. The frequency selective fading has a power delay profile (PDP) of $1.2257\times e^{-0.8l}$ $(0 \le l < L)$, which is normalized to unit energy. The CP length N_p is selected so that ISI is avoided among OFDM symbols. Unless otherwise specified, QPSK modulation is adopted and ϕ_{rms} is set as 6° in the simulations. The PN sequence $\{\alpha_k\}_{k=0}^{N/2-1}$ is generated randomly from the set $\{1, j, -j, -1\}$.

We first investigate the accuracy of CFO estimation. The channel length is chosen as $L = 8$. The integer CFO is in the range of $[-14, 14] \subset [-(N/4-1), N/4-1]$, with $N/4-1$ being the maximum integer CFO that can be estimated by the proposed method. Fig. 4.1 plots the residual CFO, $\Delta\epsilon = \epsilon - \hat{\epsilon}$, at different SNRs. For each SNR, 300 independent CFO estimations are performed at the presence of phase noise. From the figure, it is obvious that the residual CFO, $\Delta\epsilon$, is consistently less than 0.2. This observation indicates that the proposed algorithm can accurately estimate the integer part of the CFO without error, *i.e.*, $\hat{z} = z$, at the presence of unknown frequency selective fading and phase noise.

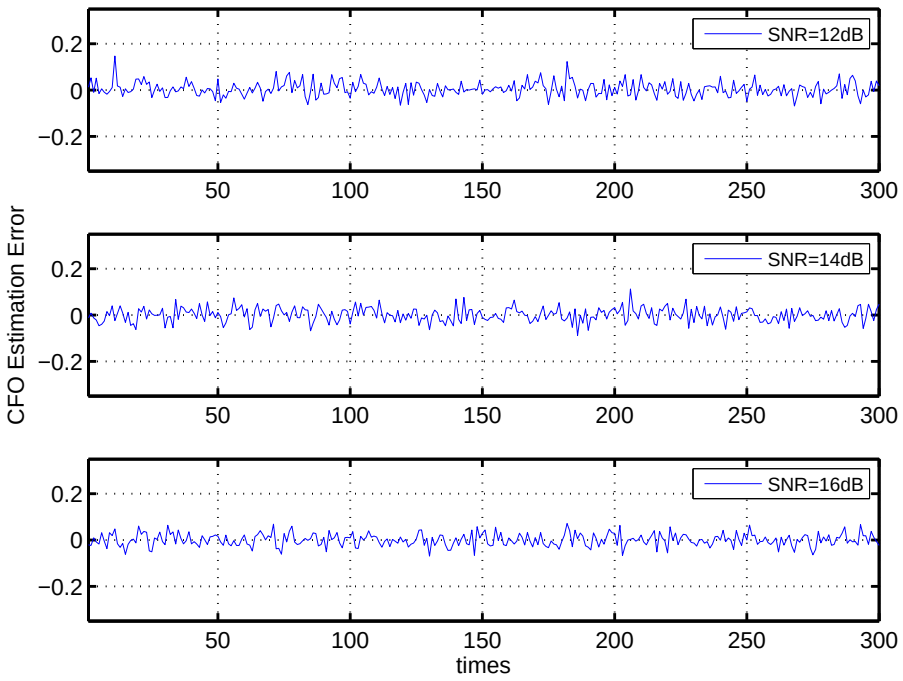

Figure 4.1: CFO estimation error ($\epsilon_0 \in (-1, 1), z \in [-14, 14]$, QPSK).

The 1000-times averaged absolute residual CFO $|\Delta\epsilon|$ is shown in Fig. 4.2 as a function

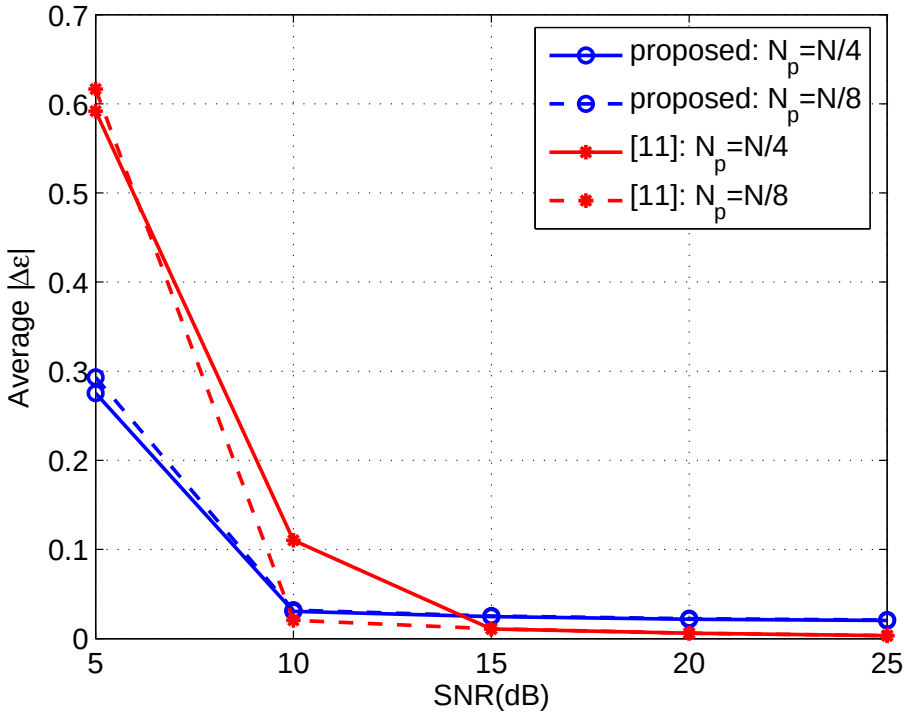

Figure 4.2: Average $|\Delta\epsilon|$ versus SNR ($\epsilon_0 \in (-1, 1), z \in [-14, 14]$, QPSK).

of SNR, with $N_p = N/4$ and $N_p = N/8$, respectively. For comparison purpose, the results obtained with the CFO estimation method in [52] are also shown in this figure. For fairness of comparison, the power of the pilot symbol used in the method of [52] is maintained the same as the pilot symbol in our proposed method. As expected, the average absolute CFO estimation error for both methods decreases monotonically with the increase of SNR. The proposed method is better than [52] at low SNR. When SNR is high, the residual CFO, $|\Delta\epsilon|$, from both methods is very small and thus has negligible impact on the subsequent channel estimation.

The performance of joint phase noise and CTF estimation algorithm is studied in the next example, where the channel length is set as $L = 10$ and $N_p = N/4$. We first consider the case that $|\epsilon| < 1$, and the performance of systems with arbitrary ϵ is discussed in the next example. Fig. 4.3 illustrates the MSE and the corresponding CRLB of the estimated normalized CTF, $\hat{\mathbf{H}}_{\text{full}}$, in the presence of phase noise. The results from MJCPCE method

[61], and the proposed algorithm neglecting phase noise are also shown in the figure for comparison. Obviously, the new algorithm achieves a performance that is very close to CRLB. As expected, the estimation performance degrades when phase noise is ignored. For the MJCPCE method, it has been shown in [61] that its MSE performance is very close to the CRLB when $|\epsilon| < 0.4$. However, its performance degrades when the range of ϵ is extended to $(-1, 1)$, as evidenced in Fig. 4.3. The performance degradation of MJCPCE method is caused by phase flipping introduced during CFO estimation. Phase flipping refers to the case that $-\pi$ is estimated as π, or vice versa, when the phase difference $\pi\epsilon$ in (4.6) approaches $-\pi$ or π. The performance of MJCPCE method suffers greatly from phase flipping, even in system with only fractional CFO. Due to phase flipping, the inclusion of CFO estimation and compensation in MJCPCE results in worse performance compared to the case that CFO is not estimated at all. Phase flipping also happens in the proposed method. However, the incorrectly estimated fractional CFO caused by phase flipping can be easily corrected by integer CFO estimation. Therefore, the performance of the proposed method is not affected by phase flipping. Similar results are observed for CIR estimation, as shown in Fig. 4.4. We repeat the simulations for system with 8PSK modulation, and observe that the proposed algorithm performs consistently well and has better performance than MJCPCE method. Finally, we note that the unresolvable residual common phase rotation (RCPR), which means the phase noise can be estimated accurately but differs from the actual one by a constant phase rotation, also exists in the proposed method, as in [61]. Detailed analysis for the cause of RCPR is referred to [61].

The next example demonstrates channel estimation performance when integer CFO z is introduced in addition to fractional CFO, ϵ_0. The maximum integer CFO is set as $z_m = 4$. The MSE results along with the CRLB of CIR estimation are presented in Fig. 4.5. As expected, the MJCPCE method, which neglects the integer CFO, doesn't function properly under such system configuration. The proposed scheme, on the other hand, consistently works well regardless of the presence of integer CFO.

The uncoded bit error rates (BER) obtained from different channel estimation algo-

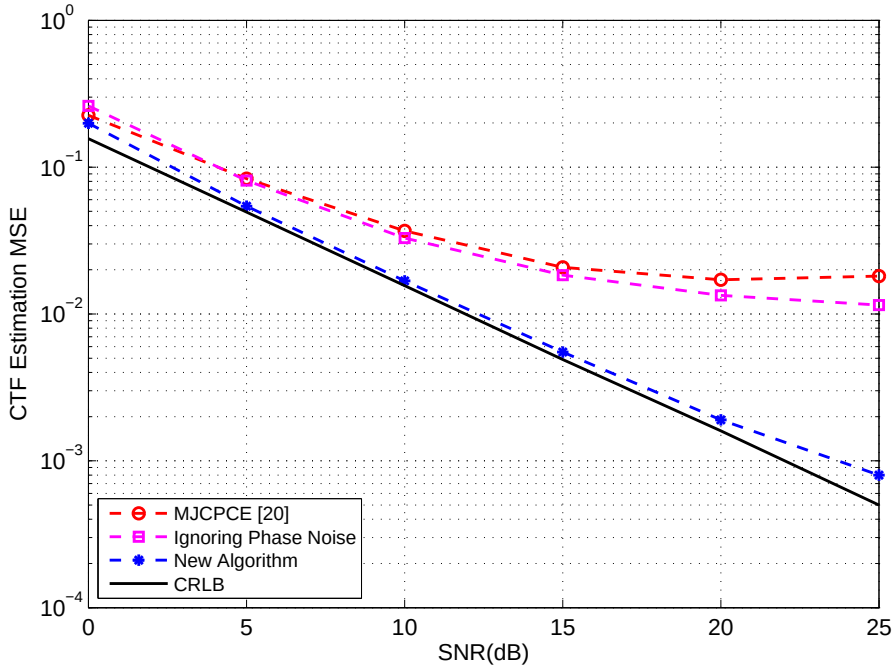

Figure 4.3: CTF estimation MSE versus SNR (QPSK, $\epsilon_0 \in (-1, 1), z = 0$).

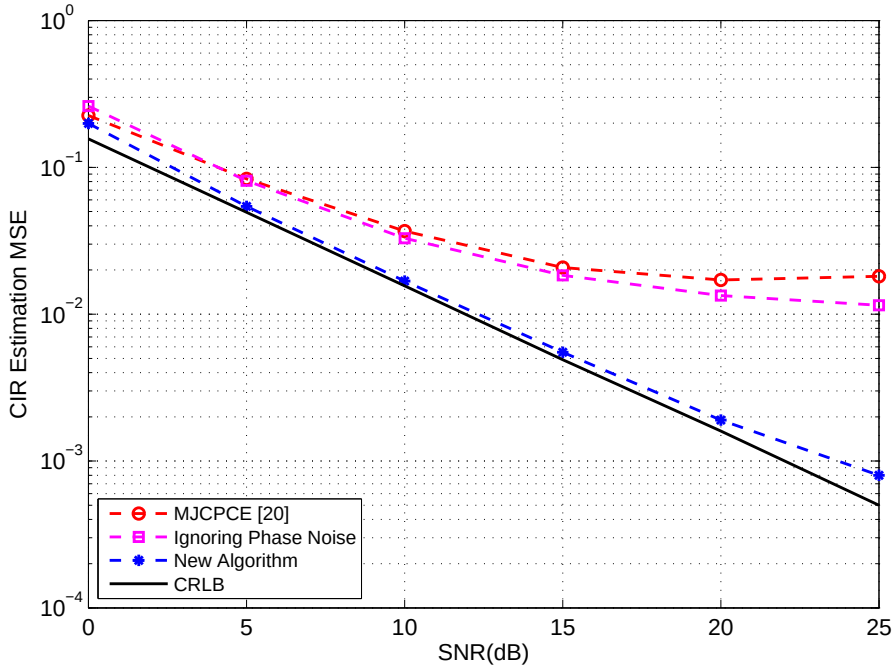

Figure 4.4: CIR estimation MSE versus SNR (QPSK, $\epsilon_0 \in (-1, 1), z = 0$).

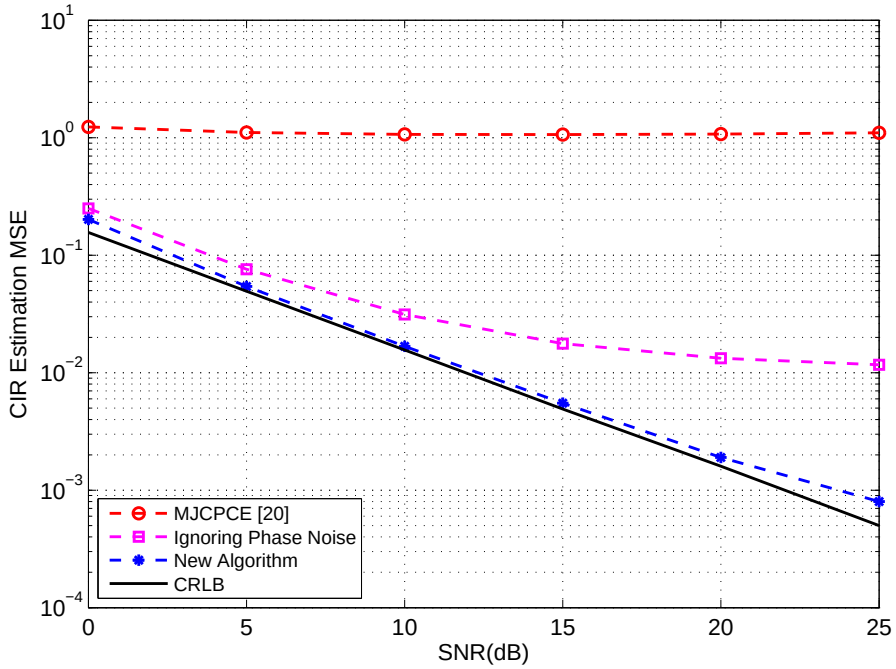

Figure 4.5: CIR estimation MSE versus SNR (QPSK, $\epsilon_0 \in (-1, 1), z \in [-4, 4]$).

rithms are compared in Fig. 4.6. The phase noise has a standard deviation of $\phi_{\text{rms}} = 10^{\text{o}}$. Each slot consists of 52 OFDM symbols with the first two as training symbols. Each BER point is obtained by simulating 1,000 slots. The BER curve for system with ideal channel estimation is plotted as a reference. The performance of the system with the proposed channel estimation method is only 0.5 dB away from the system with ideal channel estimation. This corroborates the MSE results presented in the previous figures.

4.6 Conclusion

A new channel estimation algorithm for OFDM system with CFO and phase noise was presented in this chapter. The CFO is estimated by a hybrid time-frequency estimation method. Specifically, the fractional part of the CFO is estimated by identifying phase difference between the time-domain samples from the same training symbol, while the integer part of the CFO is estimated by utilizing the frequency-domain samples residing on the same subcarrier but belonging to different training symbols. Simulation results

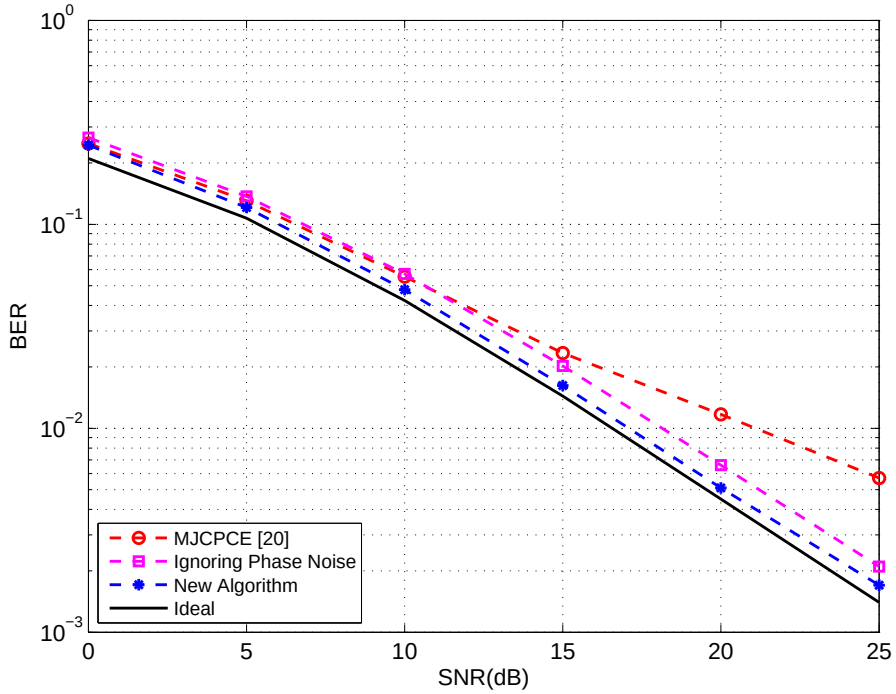

Figure 4.6: BER versus SNR ($\epsilon_0 \in (-1, 1), z = 0$, QPSK).

show that the integer part of the CFO can be estimated without error even at low SNR. With the CFO-compensated signal, a joint phase noise and CTF estimation algorithm was developed by employing the MAP criterion over the time-domain samples. Compared to the CIR estimation algorithm in the literature, the new algorithm has lower complexity and better accuracy, and it can operate without the knowledge of channel length in the time domain. Simulation results show that the joint phase noise and CTF estimation algorithm achieve a MSE performance close to CRLB. The proposed estimation method can be easily extended to single input multiple output (SIMO) OFDM system with independent fading channels.

Chapter 5

Enhanced MIMO LMMSE Turbo Equalization

5.1 Introduction

Turbo equalization is a powerful receiver technique that improves system performance by iteratively exchanging extrinsic soft information between a soft-decision equalizer and a soft-decision channel decoder. Optimum turbo equalization can be performed by using the soft-output Viterbi algorithm (SOVA) [67] – [69], or the Bahl-Cocke-Jelinek-Raviv (BCJR) algorithm [70]. Both SOVA and BCJR are trellis-based algorithms, and their computational complexity in a soft-decision equalizer grows exponentially with the channel length, L, and the modulation level, Q. The complexity gets prohibitively high when L and Q are large.

A large number of low-complexity turbo equalization algorithms have been developed during the last decade to trade-off complexity with performance for both SISO systems [71] – [76] MIMO systems [79] – [78]. In [71] – [73], a linear minimum mean square error (LMMSE) filter combined with soft-interference cancelation (SIC) is used to replace the BCJR-based optimum maximum *a posteriori* (MAP) equalizer for SISO systems. A decision-aided equalization (DAE) is proposed in [74]. DAE utilizes decisions from the pervious iteration for interference cancelation in the current iteration, and it has similar operation as [71]. A similar idea is adopted in [75], where the equalizer tap coefficients are adaptively updated taking account of the suboptimality of the previously estimated

symbols. The result in [75] is extended to an infinite-length MMSE turbo equalization in [76]. The turbo detection scheme proposed in [73] has been extended to MIMO systems [77], [78]. In [79], pre-filtering is employed to reduce the number of channel trellis states so that the BCJR-based equalization can be performed with reduced complexity for MIMO systems.

The turbo equalizer in [71] performs SIC by subtracting tentative soft decisions of the interfering symbols from the received samples. The tentative soft decisions are calculated from the *a priori* information at the input of the equalizer, and we denote it as *a priori* soft decision in this chapter. While only binary modulation is considered in [71], LMMSE turbo equalization with high-order constellation is investigated in [73]. The result of [71] has also been extended to MIMO systems undergoing frequency-selective fading [77].

In this chapter, we propose an enhanced LMMSE turbo equalizer for a spatially multiplexed MIMO system with frequency-selective fading. The turbo equalizer needs to deal with both the inter-symbol interference (ISI) due to time dispersion of the fading, and the spatial multiplexing interference (MI) among the data streams transmitted by different antennas. Existing LMMSE turbo equalizers [71] – [77] perform SIC (with respect to both ISI and MI) by completely relying on the *a priori* soft decisions of the interfering symbols. Motivated by the fact that the *a posteriori* soft information at the output of the equalizer has better quality than the *a priori* information, we propose to improve the SIC performance by continuously updating the soft decisions with the *a posteriori* information of the already equalized symbols, and such soft decision is denoted as *a posteriori* soft decision.

Since the *a posteriori* soft decision of a given symbol will affect the SIC of all the subsequent symbols to be equalized [80], [81], the order in which the symbols are equalized has significant impact on the performance. We propose a reliability-based detection ordering scheme, where symbols with more "reliable" soft input will be equalized before those with less "reliable" soft input. The reliability information can be extracted from the *a priori* soft information, which is a unique byproduct in the turbo equalization process, thus can be obtained at minimum extra cost. Simulation results demonstrate that, compared to

the existing turbo equalization methods, the proposed new turbo equalization scheme can achieve better performance at a faster converging rate .

5.2 Conventional MIMO LMMSE Turbo Equalization

Consider a MIMO system with N transmit antennas and M receive antennas as shown in Fig. 5.1. At the transmitter, N bit streams, with $a_{n,k}$ being the k-th information bit of

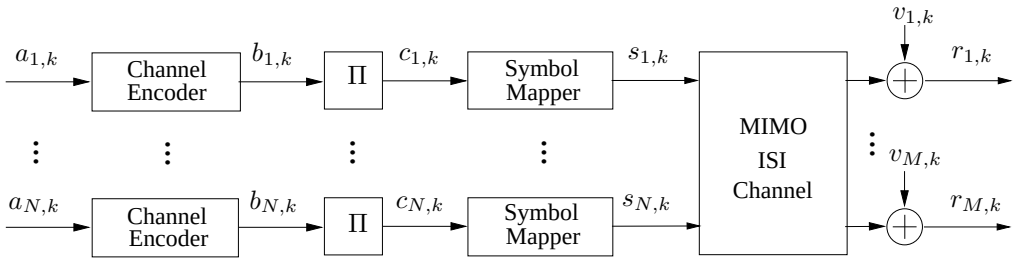

Figure 5.1: A MIMO transmission system

the n-th stream, are independently encoded, interleaved, and modulated, and the outputs of the encoder, interleaver, and symbol mapper (modulator) are denoted by $b_{n,k}$, $c_{n,k}$, and $s_{n,k}$, respectively. For a Q-ary modulation with the constellation set $\mathcal{S} = \{\chi_q\}_{q=1}^{Q}$, every $\log_2 Q$ coded bits are mapped onto one modulation symbol, *i.e.*, the group of coded bits, $\{c_{n,(k-1)\log_2 Q+p}\}_{p=1}^{\log_2 Q}$, are mapped to the modulation symbol $s_{n,k}$. The modulated symbols on the n-th branch are transmitted by the n-th transmit antenna in the form of length-N_p packet as, $\mathbf{s}^{(n)} = [s_{n,1}, \cdots, s_{n,N_p}]^t \in \mathcal{S}^{N_p \times 1}$, where $(\cdot)^t$ denotes matrix transpose.

The signal received by the m-th receive antenna at the time instant k is represented by

$$r_{m,k} = \sum_{l=0}^{L-1} \sum_{n=1}^{N} h_{m,n}(l) s_{n,k-l} + v_{m,k} \tag{5.1}$$

where $\{h_{m,n}(l)\}_{l=0}^{L-1}$ is the length-L discrete-time channel impulse response (CIR) between the n-th transmit antenna and the m-th receive antenna, and $v_{m,k}$ is the k-th sample of the zero-mean additive white Gaussian noise (AWGN) with variance σ_v^2 at the m-th receive antenna. Stacking $\{r_{m,k}\}_{m=1}^{M}$ into a column vector, $\mathbf{r}_k = [r_{1,k}, r_{2,k}, \cdots, r_{M,k}]^t \in \mathcal{C}^{M \times 1}$, leads

to

$$\mathbf{r}_k = \sum_{l=0}^{L-1} \mathbf{H}_l \mathbf{s}_{k-l} + \mathbf{v}_k \tag{5.2}$$

where

$$\mathbf{H}_l = \begin{bmatrix} h_{1,1}(l) & \cdots & h_{1,N}(l) \\ \vdots & \ddots & \vdots \\ h_{M,1}(l) & \cdots & h_{M,N}(l) \end{bmatrix} \in \mathcal{C}^{M \times N}, \tag{5.3}$$

$$\mathbf{s}_{k-l} = [s_{1,k-l}, s_{2,k-l}, \cdots, s_{N,k-l}]^t \in \mathcal{C}^{N \times 1}, \tag{5.4}$$

$$\mathbf{v}_k = [v_{1,k}, v_{2,k}, \cdots, v_{M,k}]^t \in \mathcal{C}^{M \times 1}. \tag{5.5}$$

The received samples are first processed by an SIC unit, then passed through a LMMSE equalizer in the form of a tapped-delay-line filter as shown in Fig. 5.2. The MIMO LMMSE equalizer is defined by $(K_1 + K_2 + 1)$ tap coefficient vectors, $\mathbf{w}_{n,k}(l) \in \mathcal{C}^{M \times 1}$, for $l = -K_1, \cdots, K_2$, where K_1 and K_2 are positive integers that delimit the index range of the LMMSE tap coefficients. Since there are M received samples at each sampling instant for a MIMO system as shown in (5.2), each tap coefficient of the LMMSE equalizer is a $M \times 1$ vector instead of a scalar as in the original LMMSE scheme presented in [71].

From Fig. 5.2, the equalization of $s_{n,k}$ is performed over a time window of $[k - K_2, k + K_1]$, which contains a total of $(K_1 + K_2 + 1)M$ samples from all the M receive antennas. Define the received sample vector that corresponds to the equalization window as

$$\begin{aligned} \mathbf{y}_k &= \left[\mathbf{r}_{k-K_2}^t, \mathbf{r}_{k-K_2+1}^t, \cdots, \mathbf{r}_{k+K_1}^t\right]^t \\ &= \mathbf{H}\mathbf{x}_k + \mathbf{z}_k \end{aligned} \tag{5.6}$$

where $\mathbf{H} \in \mathcal{C}^{M(K_1+K_2+1) \times N(K_1+K_2+L)}$ is expressed as

$$\mathbf{H} = \begin{bmatrix} \mathbf{H}_{L-1} & \cdots & \mathbf{H}_0 & \mathbf{0} \\ & \ddots & \ddots & \\ \mathbf{0} & \mathbf{H}_{L-1} & \cdots & \mathbf{H}_0 \end{bmatrix} \tag{5.7}$$

and $\mathbf{x}_k \in \mathcal{C}^{N(K_1+K_2+L) \times 1}$, $\mathbf{z}_k \in \mathcal{C}^{M(K_1+K_2+1) \times 1}$ are denoted, respectively, as

$$\mathbf{x}_k = \left[\mathbf{s}_{k-K_2-L+1}^t, \cdots, \mathbf{s}_{k+K_1}^t\right]^t \tag{5.8}$$

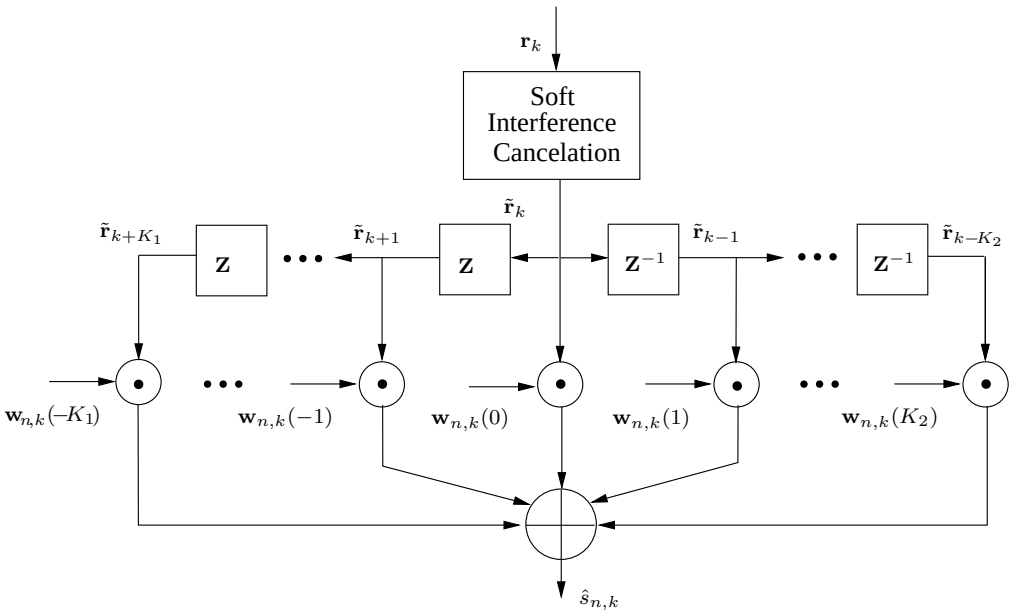

Figure 5.2: Tapped delay line structure for MIMO equalization

and

$$\mathbf{z}_k = \left[\mathbf{v}_{k-K_2}^t, \cdots, \mathbf{v}_{k+K_1}^t\right]^t. \tag{5.9}$$

Both SIC and LMMSE equalizer are designed based on the *a priori* soft information at the input of the equalizer. Define the *a priori* mean, $\bar{s}_{n,k}$, and the *a priori* variance, $\sigma_{n,k}^2$, respectively, as

$$\bar{s}_{n,k} = \sum_{q=1}^{Q} \chi_q P(s_{n,k} = \chi_q) \tag{5.10a}$$

$$\sigma_{n,k}^2 = \sum_{q=1}^{Q} (\chi_q - \bar{s}_{n,k})^2 P(s_{n,k} = \chi_q) \tag{5.10b}$$

where, according to [73], the symbol *a priori* probability $P(s_{n,k} = \chi_q)$ can be obtained from the bit *a priori* probabilities as $P(s_{n,k} = \chi_q) = \prod_{p=1}^{\log_2 Q} P\left[c_{n,(k-1)\log_2 Q+p} = c_{q,p}\right]$, with $\left\{c_{n,(k-1)\log_2 Q+p}\right\}_{p=1}^{\log_2 Q}$ and $\left\{c_{q,p}\right\}_{p=1}^{\log_2 Q}$ being the mapping bits of $s_{n,k}$ and χ_q, respectively. The *a priori* probability $P(c_{n,k})$ of the coded bit is calculated directly with the input bit *a priori* log-likelihood ratio (LLR) $\Lambda_a(c_{n,k})$, which is the interleaved output of the soft channel decoder in a turbo equalizer [73].

In the conventional LMMSE equalizer in [71], the SIC is performed by subtracting the *a priori* mean of the interfering symbols from $\mathbf{r}_k$ as

$$\tilde{\mathbf{r}}_k = \mathbf{r}_k - \sum_{l=0}^{L-1} \mathbf{H}_l \bar{\mathbf{s}}_{k-l}^{(n,k)} \tag{5.11}$$

where $\bar{\mathbf{s}}_j^{(n,k)} = [\bar{s}_{1,j}, \cdots, \bar{s}_{N,j}]^t$ when $j \neq k$, and $\bar{s}_k^{(n,k)} = [\bar{s}_{1,k}, \cdots, \bar{s}_{n-1,k}, 0, \bar{s}_{n+1,k}, \cdots, \bar{s}_{N,k}]^t$. It can be seen that the *a priori* mean of the symbols are used during the SIC.

The output of the SIC passes through the tapped-delay-line filter, which produces the equalized symbol as

$$\hat{s}_{n,k} = \sum_{l=-K_1}^{K_2} \mathbf{w}_{n,k}^h(l) \tilde{\mathbf{r}}_{k-l} = \mathbf{w}_{n,k}^h \tilde{\mathbf{y}}_{n,k} \tag{5.12}$$

where $(\cdot)^h$ denotes matrix Hermitian transpose, and $\mathbf{w}_{n,k} = [\mathbf{w}_{n,k}^h(K_2), \cdots, \mathbf{w}_{n,k}^h(-K_1)]^h \in \mathcal{C}^{(K_1+K_2+1)M\times 1}$. The vector $\tilde{\mathbf{y}}_{n,k} = [\tilde{\mathbf{r}}_{k-K_2}^t, \cdots, \tilde{\mathbf{r}}_{k+K_1}^t]^t$ can also be calculated as $\tilde{\mathbf{y}}_{n,k} = \mathbf{y}_k - \mathbf{H}\bar{\mathbf{x}}_{n,k}$, with

$$\bar{\mathbf{x}}_{n,k} = [\bar{\mathbf{s}}_{k-K_2-L+1}^{(n,k)}; \cdots; \bar{\mathbf{s}}_{k+K_1}^{(n,k)}] \in \mathcal{C}^{N(K_1+K_2+L)\times 1} \tag{5.13}$$

where $[\mathbf{a}; \mathbf{b}]$ means stacking two column vectors, $\mathbf{a}$ and $\mathbf{b}$, vertically into a single column vector.

Based on the MMSE criterion, the equalizer coefficient vector can be calculated as

$$\mathbf{w}_{n,k}^h = \mathbb{E}[|s_{n,k}|^2]\mathbf{h}_n^h \times \{\mathbf{\Sigma}_k + [\mathbb{E}(|s_{n,k}|^2) - \sigma_{n,k}^2]\mathbf{h}_n\mathbf{h}_n^h\}^{-1} \tag{5.14}$$

where $\mathbf{h}_n$ is the $[N(K_2+L-1)+n]$-th column of $\mathbf{H}$. The matrix $\mathbf{\Sigma}_k$ is defined as

$$\begin{aligned}
\mathbf{\Sigma}_k &\triangleq \mathrm{Cov}[\mathbf{y}(k), \mathbf{y}(k)] \\
&= \mathbf{H}\mathrm{diag}\{\sigma_{1,k-K_2-L+1}^2, \cdots, \sigma_{N,k-K_2-L+1}^2, |\cdots|\sigma_{1,k}^2, \\
&\quad \cdots, \sigma_{N,k}^2, |\cdots|\sigma_{1,k+K_1}^2, \cdots, \sigma_{N,k+K_1}^2\}\mathbf{H}^h + \sigma_v^2\mathbf{I}
\end{aligned} \tag{5.15}$$

where $\mathrm{Cov}(\cdot)$ is the auto-covariance operation, $\mathbf{I}$ is an identity matrix of size $M(K_1+K_2+1)$, and $\mathrm{diag}\{\cdot\}$ returns a diagonal matrix. Without loss of generality, the power of the modulation symbol is set as $\mathbb{E}[|s_{n,k}|^2] = 1$, then the equalizer vector can be simplified as

$$\mathbf{w}_{n,k}^h = \mathbf{h}_n^h\{\mathbf{\Sigma}_k + [1-\sigma_{n,k}^2]\mathbf{h}_n\mathbf{h}_n^h\}^{-1} \tag{5.16}$$

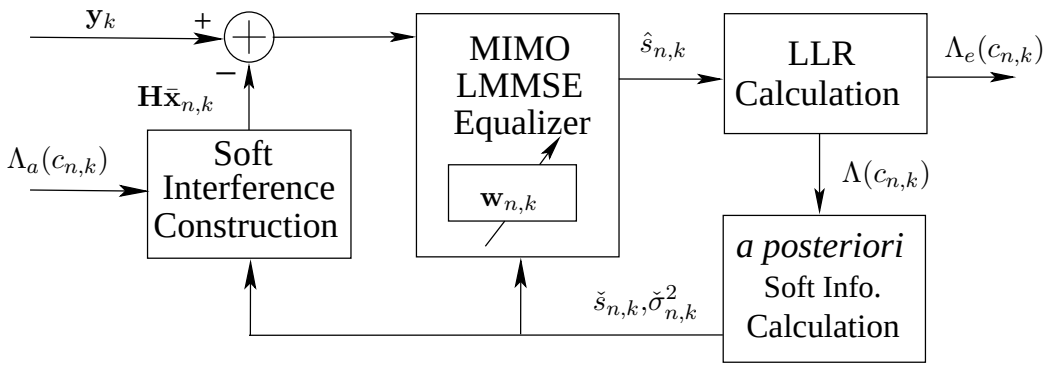

Figure 5.3: Enhanced MIMO LMMSE turbo equalizer structure.

For turbo equalization, the equalized symbol in (5.12) will be translated into soft information in the form of extrinsic LLR $\Lambda_e(c_{n,k})$, which will be used as the input for the soft-decision channel decoder. The soft-decision channel decoder then generates new extrinsic information fed back to the turbo equalizer to launch the next iteration. In this work, we focus on the enhanced design of the turbo equalizer, and the details on turbo detection are referred to [77].

5.3 Enhanced MIMO LMMSE Turbo Equalization

The block diagram of the enhanced MIMO LMMSE turbo equalizer is shown in Fig. 5.3.

5.3.1 SIC Using *a posteriori* Soft Decisions

The SIC is performed by subtracting soft decisions of the interfering symbols from the received samples. In conventional turbo equalization [71] – [77], the soft decision is in the form of the *a priori* mean as shown in (5.10a) and (5.11), which is calculated from the soft information at the *input* of the equalizer. The performance of SIC depends heavily on the quality of the soft decision. Intuitively, the soft information at the *output* (the *a posteriori* information) of the equalizer should have a better fidelity compared to that at the *input* (the *a priori* information).

Since the equalization is performed on a symbol-by-symbol basis, the *a posteriori* information of the already equalized symbols can be used during the SIC for all the subsequent

symbols to be equalized. It is expected that extra performance gain can be achieved by performing SIC with the *a posteriori* information given its better quality.

The *a posteriori* information can be obtained by analyzing the statistical properties of the equalizer output $\hat{s}_{n,k}$ (c.f. (5.12)). Similar to [71] and [73], it is assumed that the conditional probability density function (PDF) $p(\hat{s}_{n,k}|s_{n,k} = \chi_q)$ is Gaussian, with the conditional mean, $\mu_{n,k}(q) \triangleq \mathrm{E}[\hat{s}_{n,k}|s_{n,k} = \chi_q]$, and conditional variance, $\sigma^2_{n,k}(q) \triangleq \mathrm{Cov}(\hat{s}_{n,k}, \hat{s}_{n,k}|s_{n,k} = \chi_q)$, as

$$\begin{aligned}
\mu_{n,k}(q) &= \mathrm{E}[\mathbf{w}^h_{n,k}\tilde{\mathbf{y}}_{n,k}|s_{n,k} = \chi_q] \\
&= \mathbf{w}^h_{n,k}\,\mathrm{E}[(\mathbf{H}\mathbf{x}_k + \mathbf{z}_k - \mathbf{H}\bar{\mathbf{x}}_{n,k})|s_{n,k} = \chi_q] \\
&= \chi_q \mathbf{w}^h_{n,k}\mathbf{h}_n
\end{aligned} \tag{5.17}$$

and

$$\begin{aligned}
\sigma^2_{n,k}(q) &= \mathbf{w}^h_{n,k}\mathrm{Cov}(\tilde{\mathbf{y}}_{n,k}, \tilde{\mathbf{y}}_{n,k}|s_{n,k} = \chi_q)\mathbf{w}_{n,k} \\
&= \mathbf{w}^h_{n,k}\mathrm{Cov}(\mathbf{y}_k, \mathbf{y}_k|s_{n,k} = \chi_q)\mathbf{w}_{n,k} \\
&= \mathbf{w}^h_{n,k}[\mathbf{\Sigma}_k - \sigma^2_{n,k}\mathbf{h}_n\mathbf{h}^h_n]\mathbf{w}_{n,k}
\end{aligned} \tag{5.18}$$

where the two identities $\mathrm{Cov}(\mathbf{a}^h\mathbf{x}, \mathbf{a}^h\mathbf{x}) = \mathbf{a}^h\mathrm{Cov}(\mathbf{x}, \mathbf{x})\mathbf{a}$ and $\mathrm{Cov}(\mathbf{x}+\mathbf{a}, \mathbf{x}+\mathbf{a}) = \mathrm{Cov}(\mathbf{x}, \mathbf{x})$ are used for the evaluation of (5.18). The *a posteriori* probability can then be calculated as

$$P(s_{n,k} = \chi_q|\hat{s}_{n,k}) = \frac{p(\hat{s}_{n,k}|s_{n,k} = \chi_q)P(s_{n,k} = \chi_q)}{p(\hat{s}_{n,k})} \tag{5.19}$$

where $P(s_{n,k} = \chi_q)$ is the *a priori* probability obtained at the equalizer input, and $p(\hat{s}_{n,k})$ can be obtained by using $\sum_{q=1}^{Q} p(s_{n,k} = \chi_q|\hat{s}_{n,k}) = 1$.

With (5.19), define, respectively, the *a posteriori* mean and the *a posteriori* variance of $s_{n,k}$ as

$$\check{s}_{n,k} = \sum_{q=1}^{Q} \chi_q P(s_{n,k} = \chi_q|\hat{s}_{n,k}) \tag{5.20a}$$

$$\check{\sigma}^2_{n,k} = \sum_{q=1}^{Q} (\chi_q - \check{s}_{n,k})^2 P(s_{n,k} = \chi_q|\hat{s}_{n,k}) \tag{5.20b}$$

We propose to use the *a posteriori* mean given in (5.20a) as the *a posteriori* soft decision, which will be used during the SIC in a similar way as described in (5.12). With the progress of the equalization, the *a priori* soft decision, $\bar{s}_{n,k}$, will be replaced by the *a posteriori* soft decision, $\check{s}_{n,k}$, once $s_{n,k}$ is equalized. As a result, the soft decision vector, $\bar{\mathbf{s}}_j^{(n,k)}$, is constantly updated with more reliable *a posteriori* decisions. Therefore, the SIC in the newly proposed scheme is performed with a combination of the *a priori* and *a posteriori* soft decisions. We will show with simulations that the system benefits from the mixed *a priori* and *a posteriori* SIC due to the better quality of the *a posteriori* soft decisions.

5.3.2 Reliability-based Detection Ordering

In conventional turbo equalization [71] – [77], the order in which the symbols are detected does not affect the detection performance, since only *a priori* statistics as shown in (5.10) are used during the equalization, and they remain unchanged during the entire packet. With the newly proposed SIC scheme, the detection order matters as to the equalization performance, because the quality of the *a posteriori* soft decision of a given symbol will affect the SIC operation of all the subsequent symbols to be equalized. A high-quality soft decision will positively affect the equalization of the subsequent symbols. Optimal detection ordering was discussed for space-time detection [80], [81], where additional operations need to be performed to determine the order of the detection.

To minimize the overhead during equalization, we propose to determine the detection order by using the *a priori* information at the equalizer input. Define the symbol *a priori* reliability as

$$\rho_{n,k} = 1/\sigma_{n,k}^2 \tag{5.21}$$

where $\sigma_{n,k}^2$ is the symbol *a priori* variance given in (5.10b). Such a definition of "reliability" is motivated by the fact that the variance of a random variable (RV) measures the expected squared deviation of the RV from its mean, which is used as the *a priori* soft decision. A lower *a priori* variance means the soft decision is closer to its true value, thus

a higher reliability of the *a priori* soft decision. We sort $\rho_{n,k}$ over an entire data packet in a descending order as

$$\boldsymbol{\rho} = [\rho_{<1>}, \rho_{<2>}, \cdots, \rho_{<NN_p>}]^t \tag{5.22}$$

such that $\rho_{<m>} \geq \rho_{<n>}$ for $m < n$, and $< \cdot >$ is an index mapping operator

$$< \cdot >: \{1, \cdots, NN_p\} \rightarrow \{(1,1), \cdots, (N, N_p)\} \tag{5.23}$$

The equalization will be performed in an order that is determined by the ordered vector $\boldsymbol{\rho}$, *i.e.*, $\forall m < n$, $s_{<m>}$ will be equalized before $s_{<n>}$ given that the *a priori* information of $s_{<m>}$ has a higher reliability. The reliability-based ordering scheme will improve the quality of the *a posteriori* soft decision, and accelerate the convergence of the turbo equalization scheme.

5.3.3 Low-Complexity Enhanced MIMO LMMSE Turbo Equalization

Similar to the conventional turbo equalization method [77], the equalizer coefficient vector, $\mathbf{w}_{n,k}$, of the newly proposed method needs to be updated for each symbol as shown in (5.16), where the computation involves inversion of a matrix of size $M(K_1 + K_2 + 1)$.

We propose a low-complexity approximation of the enhanced MIMO LMMSE turbo equalization, where the equalizer taps are calculated for every block of N_b symbols instead of for every symbol. The low-complexity equalizer coefficient vector is given as

$$\bar{\mathbf{w}}_n = \left[\frac{1}{N_p} \sum_{k=1}^{N_p} [\boldsymbol{\Sigma}_k + \left(1 - \sigma_{n,k}^2\right) \mathbf{h}_n \mathbf{h}_n^h] \right]^{-1} \mathbf{h}_n \tag{5.24}$$

Once a block of symbols are equalized with the constant equalizer taps given in (5.24), the obtained *a posteriori* soft decisions of the block will replace the corresponding *a priori* soft decisions in the subsequent SIC operations. In this case, each block is considered as a "generalized layer" in the sense that it may contain symbols at any time instant k and from any transmitter with index n. The complexity for updating the equalizer coefficient is then determined by the number of layers $R = N_t N_p / N_b$.

5.4 Simulation Results

We study a 2×2 MIMO system with quadrature phase shift keying (QPSK) modulation. The data is transmitted in packets. Each packet carries $N_p = 2,000$ information bits, which are encoded by a rate 1/2 non-systematic convolutional code with a constraint length 4 and a generator polynomial $[G_1, G_2] = [17, 13]_{\text{oct}}$. The Proakis type C channel [82] is used to construct the 2×2 MIMO channel as $\mathbf{h}_{1,1} = [0.227, 0.460, 0.668, 0.460, 0.227]$, $\mathbf{h}_{1,2} = \mathbf{h}_{1,1} \times \exp(j\pi/4)$, $\mathbf{h}_{2,1} = \mathbf{h}_{1,1} \times \exp(j3\pi/4)$, and $\mathbf{h}_{2,2} = \mathbf{h}_{1,1} \times \exp(j7\pi/4)$. The equalizer parameters K_1 and K_2 are set as $K_1 = 2L, K_2 = L$, with $L = 5$. For each investigated signal-to-noise (SNR) point, 100 packets are simulated for the bit error rate (BER) evaluation.

In Fig. 5.4, we compare the BER performance of the proposed MIMO LMMSE turbo equalization with that of the original method [77], using symbol-based equalizer coefficients adaptation. We have two observations on the results. First, as expected, the BER improves consistently as the iterations progress in both cases. Second, the proposed turbo equalization outperforms the method of [77] in all the iterations. At the BER level of 10^{-3}, the proposed method achieves a 1 dB performance improvement over [77] after the 4-th iteration.

For the low-complexity turbo equalization discussed in 5.3.3, its performance with the original SIC (which depends completely on the *a priori* soft decision) and with the newly proposed SIC (which uses a combination of the *a priori* and *a posteriori* soft decisions) are also compared, and the result is shown in Fig. 5.5. For the proposed SIC, we have chosen the block size as $N_b = 250$. It can be seen from the figure that the low-complexity turbo equalization also benefits from the proposed SIC, which leads to better BER performance than the original SIC in all the iterations.

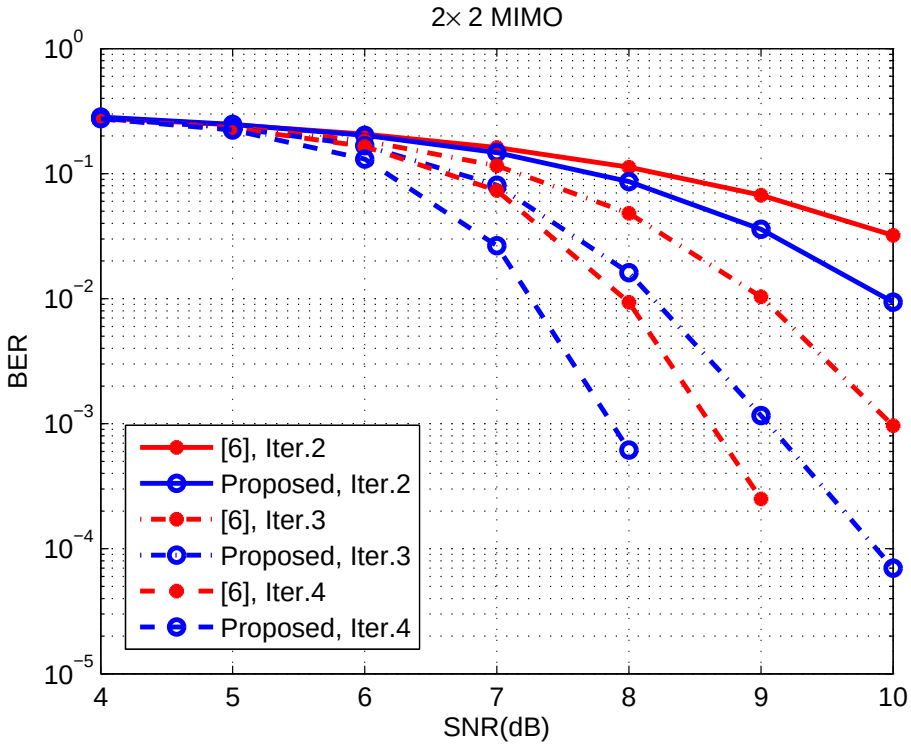

Figure 5.4: BER comparison between conventional and proposed equalization schemes

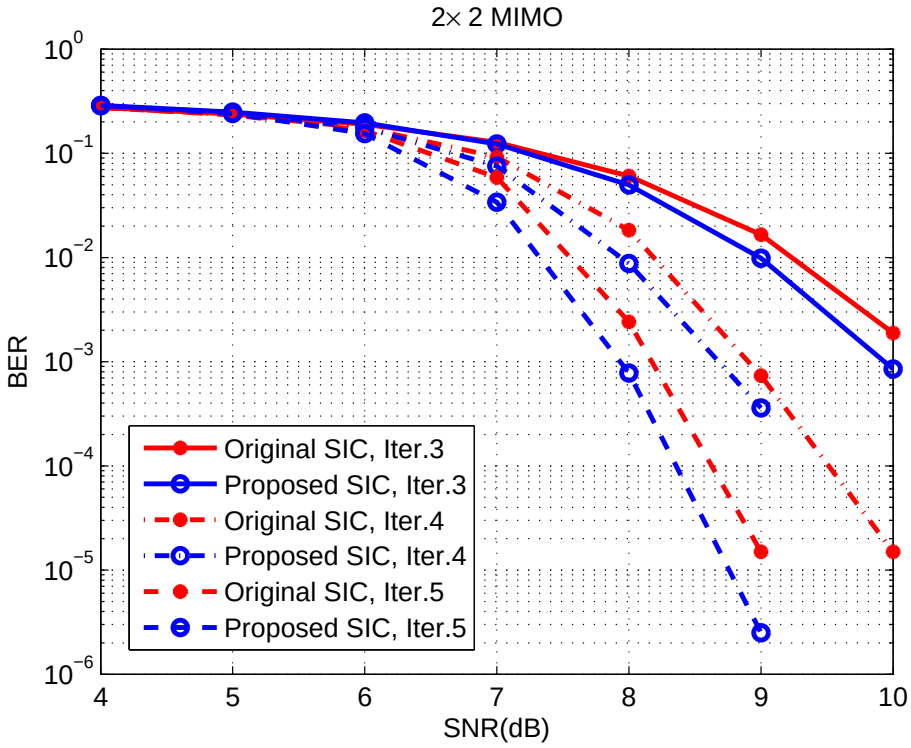

Figure 5.5: BER performance of the low-complexity turbo equalization

5.5 Conclusion

An enhanced MIMO LMMSE turbo equalization scheme was proposed in this chapter. The new turbo equalization performs SIC by continuously replacing the *a priori* soft decision with the more reliable *a posteriori* soft decision as the equalization progresses. The employment of the *a posteriori* soft decisions also enables us to take advantage of the order of detection, as an additional degree-of-freedom during the equalization process. We proposed a reliability-based detection ordering scheme, where the symbol reliability is defined as the inverse of the *a priori* mean, which is a natural byproduct of turbo equalization and can be obtained with minimum extra cost. With the enhanced MIMO LMMSE turbo equalization, considerable performance gain over existing turbo equalization methods was observed in the simulation results.

Chapter 6

MIMO Turbo Block Decision Feedback Equalization

6.1 Introduction

In last chapter, we have proposed an enhanced turbo equalization based on conventional linear equalization for MIMO systems. The conventional nonlinear equalization technologies have actually also been developed into their turbo versions. In [83], a joint coding and decision feedback equalization (DFE) scheme is proposed, where the DFE employs two transversal filters corresponding to the soft feedback from both the equalizer output and the channel decoder. In [84], soft feedback equalizer is proposed where the soft output of the equalizer is fedback for canceling the causal part of the ISI, and it is different from the turbo DFE using hard-decision feedback in [72]. Recently, a turbo detection structure employing block decision feedback equalizer (BDFE) was proposed in [126] for SISO systems. The non-linear structure of BDFE achieves better bit error rate (BER) performance than both LMMSE equalization and conventional DFE [125]. The turbo equalization in [126] has enabled a low-complexity sequence-based log-likelihood ratio (LLR) calculation leading to near-optimum performance.

In this chapter, we propose a new BDFE-based turbo equalization scheme with reliability-based successive soft interference cancellation (SSIC) for MIMO systems. In a spatially-multiplexed MIMO system with frequency selective fading, the interference among the transmitted symbols arises from two sources: the inter-symbol interference (ISI) due to

the time dispersion of the fading, and the spatial multiplexing interference (MI) among the data streams transmitted by different antennas. Therefore, the turbo equalizer for MIMO systems needs to deal with both time-domain ISI and space-domain MI. The proposed MIMO BDFE performs SSIC on both ISI and MI with previously detected soft-decision symbols. One of the main performance limiting factors of SSIC is error propagation, where an erroneously detected soft symbol will negatively affect the detection of all the subsequent symbols. Therefore, the order in which the symbols are detected during SSIC is critical to the system performance. To minimize error propagation while maintain the mechanism of successive interference cancelation, we propose a *reliability-based* group-wise detection ordering scheme. With the new scheme, an entire block is divided into multiple groups, over which symbols with higher reliability will be detected before those with lower reliability. The knowledge of symbol reliability is obtained from the symbol *a priori* probability at the input of the soft-decision equalizer, and it is a unique byproduct in the turbo equalization process.

A low-complexity implementation of the MIMO BDFE is also presented. The instantaneous BDFE filter matrices that are updated for each symbol are replaced by filter matrices that stay constant for all the symbols within one block, and this greatly reduces the computational complexity. It is shown that the adoption of the constant equalizer matrices does not apparently degrade the detection performance. In addition, following the model in [125], we present an alternative system model that incorporates all the received samples over one block in a zero-padding block transmission mode. The alternative model leads to two advantages: first, the detection performance is improved because more information is incorporated during the equalization process; second, it leads to a "windowed block-Toeplitz" structure of the channel matrix, which is desirable for developing fast algorithm for equalizer matrices calculation.

The rest of this chapter is organized as follows. Section 6.2 introduces the MIMO block transmission model and the basics of MIMO turbo detection. The theoretical analysis for the MIMO turbo BDFE together with the *reliability-based* detection ordering scheme is de-

veloped in Section 6.3. Section 6.4 presents a low-complexity implementation of the MIMO turbo BDFE. Simulation results are presented in Section 6.5 and Section 6.6 concludes the chapter.

Notation: The superscripts, $(\cdot)^t$ and $(\cdot)^h$, represent the matrix transpose and Hermitian transpose, respectively. The matrix $\mathbf{I}_N$ is an identity matrix of size N. The $M \times N$ complex matrix space is represented by $\mathcal{C}^{M\times 1}$. $\mathrm{E}(\cdot)$ is the mathematical expectation operator. The matrix $\mathrm{diag}\{d_1, d_2, \cdots, d_M\}$ is a $M \times M$ diagonal matrix with diagonal elements $d_1, d_2, \cdots, d_M$. $\mathrm{trace}\,(\mathbf{A})$ returns the trace of the matrix $\mathbf{A}$. The operator $\mathbf{a} \ll k$ denotes the left circular shift of the vector $\mathbf{a}$ by k locations.

6.2 System Description

Consider a $N \times M$ MIMO system as shown in Fig. 6.1, with N and M being the number of transmit antennas and receive antennas, respectively.

At the transmitter, N bit streams, with $a_{n,k}$ being the k-th information bit of the n-th stream, are multiplexed onto the N transmit branches. The n-th bit stream is encoded, interleaved, and modulated. The outputs of the encoder, interleaver, and symbol mapper (modulator) are denoted by $b_{n,k}$, $c_{n,k}$, and $x_{n,k}$, respectively. For a Q-ary modulation with the constellation set $\mathcal{S} = \{\chi_q\}_{q=1}^{Q}$, every $\log_2 Q$ coded bits are mapped onto one modulation symbol, *i.e.*, the group of coded bits, $\{c_{n,(k-1)\log_2 Q+p}\}_{p=1}^{\log_2 Q}$, are mapped to the modulation symbol $x_{n,k}$. The modulation symbols on the n-th branch are transmitted via the n-th transmit antenna in the form of a length-N_b block as, $\mathbf{x}^{(n)} = [x_{n,1}, x_{n,2}, \cdots, x_{n,N_b}]^t \in \mathcal{S}^{N_b\times 1}$. To avoid inter-block interference (IBI), guard intervals (GI) are inserted among the transmitted blocks. The GI is implemented as zeros padded at the beginning of each block.

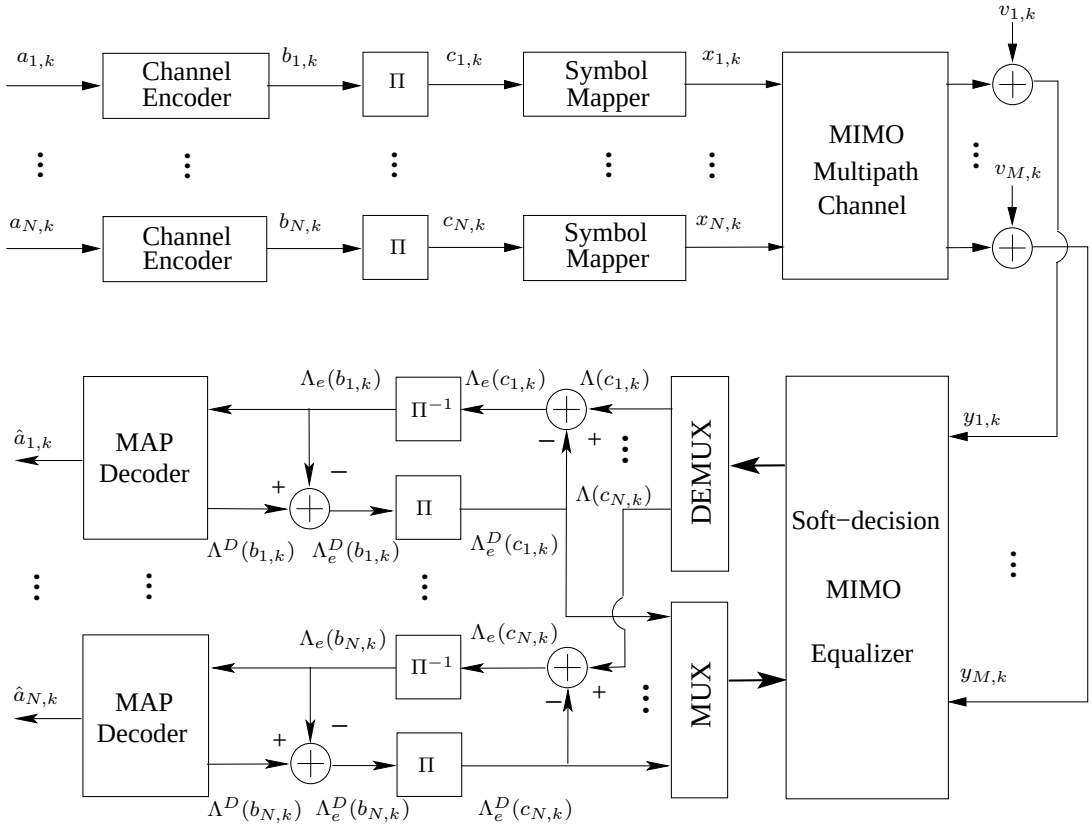

Figure 6.1: A MIMO communication system with turbo detection.

At the receiver side, the received block at the m-th receive antenna can be written as

$$y_{m,k} = \sum_{l=0}^{L-1} \sum_{n=1}^{N} f_{m,n}(l) x_{n,k-l} + v_{m,k} \tag{6.1}$$

for $k = 1, 2, \cdots, N_b + L - 1$, where $f_{m,n}(l)$ is the l-th tap of the equivalent discrete-time channel between the n-th transmit antenna and the m-th receive antenna, L is the channel length, and $v_{m,k}$ is the zero-mean additive white Gaussian noise (AWGN) with variance σ_v^2. With zero-padding block transmission, $x_{n,k} = 0$ for $k \leq 0$. It is assumed that the channel is constant over one block.

Stacking the received samples from all the receive antennas at time k into a vector, we have

$$\mathbf{y}_k = \sum_{l=0}^{L-1} \mathbf{F}_l \mathbf{x}_{k-l} + \mathbf{v}_k \tag{6.2}$$

where $\mathbf{y}_k = [y_{1,k}, \cdots, y_{M,k}]^t \in \mathcal{C}^{M\times 1}$, $\mathbf{x}_{k-l} = [x_{1,k-l}, \cdots, x_{N,k-l}]^t \in \mathcal{S}^{N\times 1}$, and $\mathbf{v}_k = [v_{1,k}, \cdots, v_{M,k}]^t \in \mathcal{C}^{M\times 1}$ are the received sample vector, transmitted symbol vector, and noise vector, respectively, and the (m,n)-th element of the channel matrix, $\mathbf{F}_l \in \mathcal{C}^{M\times N}$, is $f_{m,n}(l)$. Stacking $\{\mathbf{y}_k\}_{k=1}^{N_b+L-1}$ into a column vector, as $\mathbf{y} = \left[\mathbf{y}_1^t, \mathbf{y}_2^t, \cdots, \mathbf{y}_{N_b+L-1}^t\right]^t \in \mathcal{C}^{M(N_b+L-1)\times 1}$, leads to

$$\mathbf{y} = \mathbf{F}\mathbf{x} + \mathbf{v} \tag{6.3}$$

where $\mathbf{x} = \left[\mathbf{x}_1^t, \cdots, \mathbf{x}_{N_b}^t\right]^t \in \mathcal{S}^{NN_b\times 1}$, $\mathbf{v} = \left[\mathbf{v}_1^t, \mathbf{v}_2^t, \cdots, \mathbf{v}_{N_b+L-1}^t\right]^t \in \mathcal{C}^{M(N_b+L-1)\times 1}$, and the channel matrix, $\mathbf{F} \in \mathcal{C}^{M(N_b+L-1)\times NN_b}$, is denoted by

$$\mathbf{F} = \begin{bmatrix} \mathbf{F}_0 & \mathbf{0} & \mathbf{0} & \mathbf{0} & \cdots & \mathbf{0} & \mathbf{0} \\ \vdots & \ddots & \ddots & \ddots & \ddots & \ddots & \vdots \\ \mathbf{F}_{L-1} & \cdots & \cdots & \mathbf{F}_0 & \mathbf{0} & \cdots & \mathbf{0} \\ \vdots & \ddots & \ddots & \ddots & \ddots & \ddots & \vdots \\ \mathbf{0} & \mathbf{0} & \cdots & \mathbf{F}_{L-1} & \cdots & \cdots & \mathbf{F}_0 \\ \vdots & \ddots & \ddots & \ddots & \ddots & \ddots & \vdots \\ \mathbf{0} & \mathbf{0} & \mathbf{0} & \mathbf{0} & \cdots & \mathbf{0} & \mathbf{F}_{L-1} \end{bmatrix}. \tag{6.4}$$

The channel matrix in (6.4) possesses a block-Toepliz structure that is desirable for fast algorithm implementation.

For a MAP-based detection, the detector calculates the LLR of the information bit as follows

$$\begin{aligned} \Lambda\left[a_{n,k}\right] &\triangleq \ln\frac{P\left[a_{n,k}=0|\mathbf{y}\right]}{P\left[a_{n,k}=1|\mathbf{y}\right]} \\ &= \underbrace{\ln\frac{\sum\limits_{\forall \mathbf{a}: a_{n,k}=0} p(\mathbf{y}|\mathbf{a})\left[\prod\limits_{\forall n',k': k'\neq k \text{ if } n'=n} P(a_{n',k'})\right]}{\sum\limits_{\forall \mathbf{a}: a_{n,k}=1} p(\mathbf{y}|\mathbf{a})\left[\prod\limits_{\forall n',k': k'\neq k \text{ if } n'=n} P(a_{n',k'})\right]}}_{\Lambda_e\left[a_{n,k}\right]} + \Lambda_a[a_{n,k}] \end{aligned} \tag{6.5}$$

where $\Lambda_a[a_{n,k}] = \ln\frac{P\left[a_{n,k}=0\right]}{P\left[a_{n,k}=1\right]}$ is the *a priori* LLR of $a_{n,k}$. The computation of (6.5) has a complexity on the order of $\mathcal{O}\left(Q^{NN_b}\right)$ [87], and it becomes prohibitively high when N and N_b are large. A reduced-complexity detection scheme is shown in the bottom part of Fig. 6.1,

which performs separate equalization and decoding. The MIMO equalizer produces soft decisions for all the N transmitted streams. At the n-th output branch, the extrinsic LLR, $\Lambda_e[c_{n,k}] = \Lambda[c_{n,k}] - \Lambda_a[c_{n,k}]$, of the code bit is deinterleaved into $\Lambda_e[b_{n,k}]$, which is used as the *a priori* soft input of the channel decoder. The decoder calculates the extrinsic LLR, $\Lambda_e^D[b_{n,k}] = \Lambda^D[b_{n,k}] - \Lambda_e[b_{n,k}]$, for each code bit by exploiting the code trellis structure and the *a priori* information $\Lambda_e[b_{n,k}]$. The extrinsic LLR at the output of the channel decoder is interleaved into $\Lambda_e^D[c_{n,k}]$, which is then fed back to the soft-decision equalizer as the *a priori* LLR for the next iteration. Successive iterations are performed until convergence is achieved. In the final iteration, the decoder calculates the LLR $\Lambda[a_{n,k}]$ of the information bit and outputs the corresponding hard decision, $\hat{a}_{n,k}$. In practice, the MAP-based channel decoder is commonly adopted with moderate number of trellis states resulting in acceptable complexity. The MAP-based equalizer, however, may incur a prohibitive complexity in the order of $\mathcal{O}\left(Q^{NL}\right)$ especially for large channel length L. We next develop a sub-optimum soft-decision MIMO equalizer that can approach the performance of the optimum MAP equalizer, but at a much lower complexity.

6.3 MIMO Turbo BDFE with Reliability-based SSIC

In this section, a soft-decision MIMO BDFE is developed by employing a new *reliability-based* SSIC.

6.3.1 Reliability-based SSIC

The reliability information of a symbol is extracted from the *a priori* statistics of the symbol at the input of the equalizer. Define the *a priori* mean and the *a priori* variance of a symbol, $x_{n,k}$, as

$$\bar{x}_{n,k} = \sum_{q=1}^{Q} \chi_q P(x_{n,k} = \chi_q), \tag{6.6a}$$

$$\sigma_{n,k}^2 = \sum_{q=1}^{Q} (\chi_q - \bar{x}_{n,k})^2 P(x_{n,k} = \chi_q), \tag{6.6b}$$

where $P(x_{n,k} = \chi_q)$ is the symbol *a priori* probability, and it can be obtained from the bit *a priori* probabilities as, $P(s_{n,k} = \chi_q) = \prod_{p=1}^{\log_2 Q} P\left[c_{n,(k-1)\log_2 Q+p} = c_{q,p}\right]$, where the bit sequence, $\{c_{q,p}\}_{p=1}^{\log_2 Q}$, is mapped to the symbol χ_q.

The *a priori* mean and *a priori* variance will be used by the reliability-based SSIC, which achieves better performance than conventional SIC from two perspectives. First, the reliability-based SSIC performs interference cancellation by subtracting tentative soft decisions instead of hard decisions of the interfering symbols. Using soft decision during SSIC will reduce the effects of error propagation, thus leads to a better system performance. Second, during the reliability-based SSIC, the symbols are ordered based on their reliability, such that more reliable symbols are detected before less reliable symbols, to further reduce the negative effects of error propagation.

We propose to measure the symbol reliability by using the symbol *a priori* variance as defined in (6.6b). The variance of a random variable (RV) measures the expected squared deviation of the RV from its mean. A lower *a priori* variance thus means less uncertainty in the soft decision, thus a better reliability. Therefore, we define the *a priori* reliability measure for the symbol $x_{n,k}$ as

$$\rho_{n,k} = \frac{1}{\sigma_{n,k}^2}. \tag{6.7}$$

With the reliability information, the detection ordering can be determined. Instead of sorting $\rho_{n,k}$ over the entire block, we propose a *group-wise* detection ordering scheme based on the considerations of both performance and complexity. As to detection performance, the SIC should be performed among neighboring symbols that mutually interfere with each other. For symbols that are further apart in the time domain, their mutual interference will be very small. As a result, a global ordering of all the symbols might group unrelated symbols together and destroy the SIC mechanism. In the proposed group-wise ordering scheme, adjacent symbols are clustered into the same group, thus SIC is always guaranteed. As to complexity, a local ordering within a small group demands much less computations than the global ordering over the entire block.

With the *group-wise* ordering scheme, the reliability information is first divided into N_g groups with size NN_r as

$$\mathcal{G}_1 = \{\rho_{1,k}, \cdots, \rho_{N,k}\}_{k=1}^{N_r}, \mathcal{G}_2 = \{\rho_{1,k}, \cdots, \rho_{N,k}\}_{k=N_r+1}^{2N_r}, \\ \cdots, \mathcal{G}_{N_g} = \{\rho_{1,k}, \cdots, \rho_{N,k}\}_{k=(N_g-1)N_r+1}^{N_gN_r} \tag{6.8}$$

where $N_b = N_gN_r$. Sorting $\rho_{n,k}$ within each of the N_g groups in an ascending order, leads to

$$\mathcal{G}_i' = [\rho_{\langle O_{(i-1)NN_r+1}\rangle}, \rho_{\langle O_{(i-1)NN_r+2}\rangle}, \cdots, \rho_{\langle O_{iNN_r}\rangle}], \quad \text{for} \quad i = 1, 2, \cdots, N_g \tag{6.9}$$

such that $\rho_{\langle O_{(i-1)NN_r+1}\rangle} \leq \rho_{\langle O_{(i-1)NN_r+2}\rangle} \leq \cdots \leq \rho_{\langle O_{iNN_r}\rangle}$, where the ordered index set, $\{O_{(i-1)NN_r+1}, \cdots, O_{iNN_r}\}$, is a permutation of the index set, $\{(i-1)NN_r+1, \cdots, iNN_r\}$, and $\langle\cdot\rangle$ is an index mapping operator defined as

$$\langle\cdot\rangle : \langle j\rangle = (n,k) \quad \text{with} \quad j = (k-1)N + n \tag{6.10}$$

Stack the ordered reliability information of all the groups into a column vector as

$$\boldsymbol{\rho} = [\rho_{\langle O_1\rangle}, \rho_{\langle O_2\rangle}, \cdots, \rho_{\langle O_{NN_b}\rangle}]^t, \tag{6.11}$$

The reliability-based ordering leads to an alternative system representation

$$\mathbf{y} = \mathbf{H}\mathbf{x}' + \mathbf{v} \tag{6.12}$$

where $\mathbf{x}' = [x_{\langle O_1\rangle}, x_{\langle O_2\rangle}, \cdots, x_{\langle O_{NN_b}\rangle}]^t$, $\mathbf{H} = [\mathbf{f}_{O_1}, \mathbf{f}_{O_2}, \cdots, \mathbf{f}_{O_{NN_b}}]$, with $\mathbf{f}_j$ being the j-th column of the channel matrix $\mathbf{F}$. In (6.12), the symbols in $\mathbf{x}'$ are ordered based on their respective *a priori* reliability, $\rho_{n,k}$, in an ascending order within their own groups. Such a reliability based ordering will benefit the MIMO BDFE with SSIC as shown in Fig. 6.2.

During the detection of the symbol $x_{\langle O_g\rangle}$, a feedforward filter, $\mathbf{C}_g \in \mathcal{C}^{NN_b \times M(N_b+L-1)}$, and a zero-diagonal strict upper triangular feedback filter, $\mathbf{D}_g \in \mathcal{C}^{NN_b \times NN_b}$, are adopted, leading to

$$\tilde{\mathbf{x}}_g' = \mathbf{C}_g\left(\mathbf{y} - \mathbf{H}\bar{\mathbf{x}}_g'\right) - \mathbf{D}_g\left(\hat{\mathbf{x}}' - \bar{\mathbf{x}}_g'\right) + \bar{\mathbf{x}}_g' \tag{6.13}$$

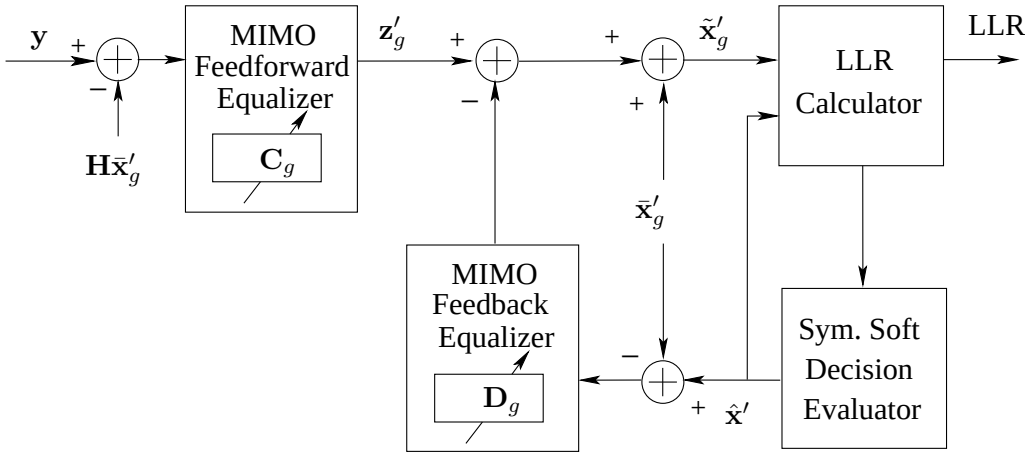

Figure 6.2: Soft-decision MIMO BDFE (when $x_{\langle O_g \rangle}$ is equalized).

where $\bar{\mathbf{x}}'_g = [\bar{x}_{\langle O_1 \rangle}, \cdots, \bar{x}_{\langle O_{g-1} \rangle}, 0, \bar{x}_{\langle O_{g+1} \rangle}, \cdots, \bar{x}_{\langle O_{NN_b} \rangle}]^t$ is the ordered *a priori* mean vector with the g-th element being zero, $\hat{\mathbf{x}}' = [\hat{x}_{\langle O_1 \rangle}, \cdots, \hat{x}_{\langle O_{NN_b} \rangle}]^t$ is the ordered tentative soft decision vector, and $\tilde{\mathbf{x}}'_g$ is the ordered vector at the output of the MIMO BDFE. The tentative soft decision is defined as the *a posteriori* mean at the output of the equalizer, as

$$\hat{x}_{\langle O_g \rangle} = \sum_{q=1}^{Q} \chi_q P(x_{\langle O_g \rangle} = \chi_q | \mathbf{y}). \tag{6.14}$$

where $P(x_{\langle O_g \rangle} = \chi_q | \mathbf{y})$ is the symbol *a posteriori* probability at the output of the MIMO BDFE. The calculation of $P(x_{\langle O_g \rangle} = \chi_q | \mathbf{y})$ is discussed in Subsection 6.3.3. Using soft decision during interference cancelation will partly reduce the negative effects of error propagation.

The upper triangular structure of $\mathbf{D}_g$ determines that the interference cancellation is performed successively by following the reverse order of the elements in $\mathbf{x}'$, *i.e.*, the last element in $\mathbf{x}'$ is detected first, and the first element in $\mathbf{x}'$ is detected last. With the reliability based ordering described in (6.11) and (6.12), symbols with higher *a priori* reliability is detected before those with lower reliability, and this will significantly reduce the negative impacts of error propagation plaguing most SIC receivers.

6.3.2 Calculation of $\mathbf{C}_g$ and $\mathbf{D}_g$

With the common assumption of perfect decision feedback [82], *i.e.*, $\hat{\mathbf{x}}' = \mathbf{x}'$, the error vector of BDFE can be written as

$$\mathbf{e}_g = \mathbf{C}_g \left(\mathbf{y} - \mathbf{H}\bar{\mathbf{x}}'_g\right) - \left(\mathbf{D}_g + \mathbf{I}_{NN_b}\right)\left(\mathbf{x}' - \bar{\mathbf{x}}'_g\right) \tag{6.15}$$

Minimizing the mean square error, $\sigma^2_{e_g} \triangleq \mathbb{E}\left[\mathbf{e}^h_g \mathbf{e}_g\right]$, with the orthogonality principle, $\mathbb{E}\left[\mathbf{e}_g \left(\mathbf{y} - \mathbf{H}\bar{\mathbf{x}}'_g\right)^h\right] = \mathbf{0}$, leads to

$$\mathbf{C}_g = \mathbf{R}_g \mathbf{\Sigma}'_g \mathbf{H}^h \left[\mathbf{H}\mathbf{\Sigma}'_g \mathbf{H}^h + \sigma_v^2 \mathbf{I}_{M(N_b+L-1)}\right]^{-1} \tag{6.16}$$

where $\mathbf{R}_g = \mathbf{D}_g + \mathbf{I}_{NN_b}$, and $\mathbf{\Sigma}'_g = \mathrm{diag}\{\sigma^2_{\langle O_1\rangle}, \cdots, \sigma^2_{\langle O_{g-1}\rangle}, 1, \sigma^2_{\langle O_{g+1}\rangle}, \cdots, \sigma^2_{\langle O_{NN_b}\rangle}\}$ is the ordered *a priori* covariance matrix with the g-th element being 1.

Combining (6.15) and (6.16) leads to

$$\mathbf{e}_g = \mathbf{R}_g \boldsymbol{\epsilon}_g \tag{6.17}$$

with

$$\boldsymbol{\epsilon}_g = \mathbf{\Sigma}'_g \mathbf{H}^h \left[\mathbf{H}\mathbf{\Sigma}'_g \mathbf{H}^h + \sigma_v^2 \mathbf{I}_{M(N_b+L-1)}\right]^{-1} \left(\mathbf{y} - \mathbf{H}\bar{\mathbf{x}}'_g\right) - \left(\mathbf{x}' - \bar{\mathbf{x}}'_g\right) \tag{6.18}$$

The autocorrelation matrix of $\boldsymbol{\epsilon}_g$ can be calculated as

$$\begin{aligned} \mathbf{\Sigma}_{\epsilon_g} &= \mathbf{\Sigma}'_g - \mathbf{\Sigma}'_g \mathbf{H}^h \left[\mathbf{H}\mathbf{\Sigma}'_g \mathbf{H}^h + \sigma_v^2 \mathbf{I}_{M(N_b+L-1)}\right]^{-1} \mathbf{H}\mathbf{\Sigma}'_g \\ &= \left[\mathbf{\Sigma}'^{-1}_g + \frac{1}{\sigma_v^2}\mathbf{H}^h\mathbf{H}\right]^{-1} \end{aligned} \tag{6.19}$$

where the second equality is obtained with the identity $(\mathbf{A}+\mathbf{C}\mathbf{B}\mathbf{C}^h)^{-1} = \mathbf{A}^{-1} - \mathbf{A}^{-1}\mathbf{C}(\mathbf{B}^{-1} + \mathbf{C}^h\mathbf{A}^{-1}\mathbf{C})^{-1}\mathbf{C}^h\mathbf{A}^{-1}$. Based on (6.17) and (6.19), the autocorrelation matrix of $\mathbf{e}_g$ can be expressed by

$$\mathbf{\Sigma}_{e_g} = \mathbf{R}_g \left[\mathbf{\Sigma}'^{-1}_g + \frac{1}{\sigma_v^2}\mathbf{H}^h\mathbf{H}\right]^{-1} \mathbf{R}^h_g. \tag{6.20}$$

Since $\sigma^2_{e_g} = \mathrm{trace}(\mathbf{\Sigma}_{e_g})$, the minimization of the mean square error is equivalent to minimizing $\mathrm{trace}(\mathbf{\Sigma}_{e_g})$. In addition, the solution that minimizes $\mathrm{trace}(\mathbf{\Sigma}_{e_g})$ should also satisfy

the successive interference cancellation constraint, *i.e.*, $\mathbf{R}_g = \mathbf{D}_g + \mathbf{I}_{NN_b}$ needs to be an upper triangular matrix with unit diagonal elements. The solution satisfying the above conditions is found as [88]

$$\mathbf{R}_g = \mathbf{U}_g^h \tag{6.21}$$

where $\mathbf{U}_g \in \mathcal{C}^{NN_b \times NN_b}$ is a lower triangular matrix with unit diagonal elements. The matrix $\mathbf{U}_g \in \mathcal{C}^{NN_b \times NN_b}$ is obtained from the Cholesky decomposition of ${\mathbf{\Sigma}'_g}^{-1} + \frac{1}{\sigma_v^2}\mathbf{H}^h\mathbf{H}$ as

$${\mathbf{\Sigma}'_g}^{-1} + \frac{1}{\sigma_v^2}\mathbf{H}^h\mathbf{H} = \mathbf{U}_g\mathbf{\Delta}_g\mathbf{U}_g^h \tag{6.22}$$

where $\mathbf{\Delta}_g \in \mathcal{C}^{NN_b \times NN_b}$ is a diagonal matrix. The solution for the feedforward and feedback equalizer matrices can then be obtained as

$$\mathbf{C}_g = \mathbf{U}_g^h\mathbf{\Sigma}'_g\mathbf{H}^h\left[\mathbf{H}\mathbf{\Sigma}'_g\mathbf{H}^h + \sigma_v^2\mathbf{I}_{M(N_b+L-1)}\right]^{-1} \tag{6.23a}$$

$$\mathbf{D}_g = \mathbf{U}_g^h - \mathbf{I}_{NN_b} \tag{6.23b}$$

6.3.3 Calculation of Extrinsic LLR Based on Equalized Symbols

The calculation of the extrinsic LLR at the MIMO BDFE output is discussed in this subsection. With the MIMO BDFE structure described above, we can obtain an equivalent equalization model as (c.f. (6.15))

$$\mathbf{z}_g \triangleq \mathbf{C}_g(\mathbf{y} - \mathbf{H}\bar{\mathbf{x}}'_g) = \mathbf{R}_g\left(\hat{\mathbf{x}}' - \bar{\mathbf{x}}'_g\right) + \mathbf{e}_g. \tag{6.24}$$

From (6.24), the g-th element in $\mathbf{z}_g$ can be represented by

$$z_g = x_{\langle O_g\rangle} + \sum_{l=g+1}^{NN_b} r_{g,l}\left[\hat{x}_{\langle O_l\rangle} - \bar{x}_{\langle O_l\rangle}\right] + e_g \tag{6.25}$$

where $r_{g,l}$ is the (g,l)-th element of $\mathbf{R}_g$ with $r_{g,l} = 1$ when $g = l$. The *a posteriori* probability (APP) of $x_{\langle O_g\rangle}$ conditioned on z_g is

$$P\left(x_{\langle O_g\rangle}|z_g\right) = \frac{p\left(z_g|x_{\langle O_g\rangle}\right)P\left(x_{\langle O_g\rangle}\right)}{p\left(z_g\right)}. \tag{6.26}$$

With the common approximation that e_g in (6.25) is a zero-mean complex Gaussian random variable, we have the conditional probability

$$p\left(z_g|x_{\langle O_g\rangle}\right) \approx \frac{1}{\pi\alpha_g^2}\exp\left\{-\frac{|\beta_g|^2}{\alpha_g^2}\right\} \tag{6.27}$$

where $\beta_g = z_g - x_{\langle O_g\rangle} - \sum_{l=g+1}^{NN_b} r_{g,l}\left[\hat{x}_{\langle O_l\rangle} - \bar{x}_{\langle O_l\rangle}\right]$. Since $\mathbf{\Sigma}_{e_g} = \mathbf{\Delta}_g^{-1}$, the variance of e_g is $\alpha_g^2 = \delta_{g,g}^{-1}$ with $\delta_{g,g}$ being the g-th diagonal element of $\mathbf{\Delta}_g$. To determine (6.26), the symbol *a priori* probability, $P\left(x_{\langle O_g\rangle}\right)$, can be calculated based on the bit *a priori* probabilities at the input to the equalizer, and are initialized as $P\left(x_{\langle O_g\rangle}\right) = \frac{1}{Q}$ during the first iteration. The value of $p(z_g)$ can be obtained by using the normalization $\sum_{q=1}^{Q} P\left(x_{\langle O_g\rangle} = \chi_q|z_g\right) = 1$.

Once the symbol APP $p\left(x_{\langle O_g\rangle}|z_g\right)$ is obtained, the bit APP $\left\{c_{n_g,(k_g-1)\log_2 Q+p}\right\}_{p=1}^{\log_2 Q}$ of the symbol $x_{\langle O_g\rangle}$, can be calculated as follows

$$P\left[c_{n,(k-1)\log_2 Q+p} = b|z_g\right] = \sum_{x_{\langle O_g\rangle}\in\mathcal{S}_p^{(b)}} P\left(x_{\langle O_g\rangle}|z_g\right) \tag{6.28}$$

where $\langle O_g\rangle = (n_g, k_g)$, $\mathcal{S}_p^{(b)} \triangleq \{\chi_q|\chi_q \in \mathcal{S} : c_{q,p} = b\}$ with $b \in \{0,1\}$, for $p = 1, \cdots, \log_2 Q$. The LLR of the code bit can then be calculated as

$$\Lambda\left[c_{n_g,(k_g-1)\log_2 Q+p}\right] = \ln\frac{\sum\limits_{x_{\langle O_g\rangle}\in\mathcal{S}_p^{(0)}} P\left(x_{\langle O_g\rangle}|z_g\right)}{\sum\limits_{x_{\langle O_g\rangle}\in\mathcal{S}_p^{(1)}} P\left(x_{\langle O_g\rangle}|z_g\right)}. \tag{6.29}$$

The extrinsic bit LLR is obtained by subtracting the *a priori* LLR, $\Lambda_a\left[c_{n_g,(k_g-1)\log_2 Q+p}\right]$, from (6.29). The bit extrinsic LLR will then be de-interleaved and used as the *a priori* input to the channel decoder.

Finally, since it is computationally expensive to calculate the sequence-based symbol APP $P(x_{\langle O_g\rangle}|\mathbf{y})$, the symbol APP $p\left(x_{\langle O_g\rangle}|z_g\right)$ is treated as an approximation of $P(x_{\langle O_g\rangle}|\mathbf{y})$, and is then used for calculating the tentative soft decision, $\hat{x}_{\langle O_g\rangle}$, as described in (6.14).

6.4 Low Complexity MIMO Turbo BDFE

One of the main computational burdens of the proposed algorithm comes from the calculation of the equalizer matrices in (6.23a) and (6.23b), which need to be updated for each

symbol. The calculation of the matrices $\mathbf{C}_g$ and $\mathbf{D}_g$ involves one Cholesky decomposition in (6.22) and one matrix inversion in (6.23a), resulting in a computational complexity in the order of $\mathcal{O}((NN_b)^3)$. The overall complexity over the entire BDFE block is then in the order of $\mathcal{O}((NN_b)^4)$, which is prohibitively expensive when N or N_b gets large. It is desirable to develop a low-complexity implementation that does not apparently sacrifice the performance of the MIMO BDFE. We propose to reduce the computation complexity of the MIMO BDFE from two perspectives described as follows.

First, the symbol-dependent equalizer matrices, $\mathbf{C}_g$ and $\mathbf{D}_g$, are replaced with constant symbol-independent matrices, $\mathbf{C}$ and $\mathbf{D}$, to achieve a low-complexity approximation of the MIMO turbo BDFE. A close observation on (6.23) reveals that the symbol-wise filter updating is solely due to the dependence on the second-order *a priori* information $\mathbf{\Sigma}'_g$. Therefore, computational complexity can be significantly reduced by replacing $\mathbf{\Sigma}'_g$ with the constant autocorrelation matrix $\mathbf{\Sigma}' = \text{diag}\{\sigma^2_{\langle O_1\rangle}, \sigma^2_{\langle O_2\rangle}, \cdots, \sigma^2_{\langle O_{NN_b}\rangle}\}$, which leads to the constant filter matrices, $\mathbf{C}$ and $\mathbf{D}$, for all the symbols to be equalized. It is demonstrated through simulations that employing constant equalizer matrices for all the symbols does not apparently degrade the equalization performance.

Second, fast matrix inversion algorithm is employed to further reduce complexity. The calculation of the constant feedforward matrix $\mathbf{C}$ requires one matrix inversion, as

$$\begin{aligned}\mathbf{C} &= \mathbf{R}\mathbf{\Sigma}'\mathbf{H}^h \left[\mathbf{H}\mathbf{\Sigma}'\mathbf{H}^h + \sigma_v^2\mathbf{I}_{M(N_b+L-1)}\right]^{-1} \\ &= \frac{1}{\sigma_v^2}\mathbf{R}\left[\mathbf{\Sigma}'^{-1} + \frac{1}{\sigma_v^2}\mathbf{H}^h\mathbf{H}\right]^{-1}\mathbf{H}^h. \end{aligned} \tag{6.30}$$

With the Cholesky decomposition, $\mathbf{\Sigma}'^{-1} + \frac{1}{\sigma_v^2}\mathbf{H}^h\mathbf{H} = \mathbf{U}\mathbf{\Delta}\mathbf{U}^h$, (6.30) can be simplified to

$$\mathbf{C} = \frac{1}{\sigma_v^2}\mathbf{\Delta}^{-1}\mathbf{U}^{-1}\mathbf{H}^h \tag{6.31}$$

Since $\mathbf{\Delta}$ is a diagonal matrix, it is easy to calculate $\mathbf{\Delta}^{-1}$. As of $\mathbf{U}^{-1}$, it was pointed out in [89] that there is no need to evaluate it explicitly. Instead, based on the fact that the matrix $\mathbf{U}$ is a lower triangular matrix with unit diagonal, the back-substitution method

can be employed to solve the following linear system

$$\mathbf{U}\mathbf{A} = \frac{1}{\sigma_v^2}\mathbf{H}^h \tag{6.32}$$

where $\mathbf{A} \in \mathcal{C}^{NN_b \times M(N_b+L-1)}$ is the unknown matrix to be solved. Once $\mathbf{A}$ is obtained, the feedforward matrix $\mathbf{C}$ can be calculated as

$$\mathbf{C} = \mathbf{\Delta}^{-1}\mathbf{A} \tag{6.33}$$

The low complexity algorithm for performing one iteration of the MIMO turbo BDFE is summarized in Table 6.1.

6.4.1 Complexity Comparison with MIMO Turbo LE

The computational complexities of the LE and the proposed low-complexity BDFE for a $N \times M$ MIMO system are compared in this subsection. It is assumed that the transmission block size is N_b, and all the MN subchannels have the same length L. The complexity is measured by the number of complex multiplications (CM). For both equalization methods, the main complexity arises from two source: the calculation of equalizer taps, and the calculation of LLR.

For BDFE, the complexity of calculating constant feedforward and feedback BDFE matrices $\mathbf{C}$ and $\mathbf{D}$ is dominated by the Cholesky decomposition, which incurs computation in the order of $\mathcal{O}((NN_b)^3)$, with an exception when $\mathbf{F} = \mathbf{H}$ (refer to (6.3) and (6.12)). When $\mathbf{F} = \mathbf{H}$, the property of block-Toepliz structure of $\mathbf{F}$ in (6.4) can be utilized, which reduces the complexity of Cholesky decomposition to the order of $\mathcal{O}((NN_b)^2)$ [89]. The complexity of LLR calculation lies mainly in the filtering operation in (6.24)–(6.25), and the conditional probability evaluation operation in (6.27). Over an entire block, the filtering operation induces a complexity in the order of $\mathcal{O}(MNN_b(N_b + L - 1) + N^2N_b^2)$, and the conditional probability evaluation in (6.27) incurs a complexity in the order of $\mathcal{O}(QN^2N_b^2)$.

For LE, it is assumed that the linear equalizer has $K = K_1 + K_2 + 1$ tap vectors (each with size M) spanning over the index range $[-K_1, K_2]$. For fairness of comparison, a

Table 6.1: Low-complexity MIMO turbo BDFE algorithm

INPUT:
- received signal vector $\mathbf{y}$ as shown in Eqn. (6.3),
- *a priori* LLR $\Lambda_a\left[c_{n,(k-1)\log_2 Q+p}\right]$ of all coded bits in the block $(1 \le p \le \log_2 Q, 1 \le n \le N, 1 \le k \le N_b)$.

INITIALIZATION:
- Compute the *a priori* mean $\bar{x}_{n,k}$ and *a priori* variance $\sigma^2_{n,k}$ of all symbols according to Eqns. (6.6a) and (6.6b),
- Calculate the symbol *a priori* reliability $\rho_{n,k}=1/\sigma^2_{n,k}$, and sort $\rho_{n,k}$ in ascending order according to (6.11),
- Based on the ordering $\{O_1, O_2, \cdots, O_{NN_b}\}$, formulate the ordered system model $\mathbf{y} = \mathbf{H}\mathbf{x}' + \mathbf{v}$ as Eqn. (6.12),
- Calculate autocovariance matrix $\mathbf{\Sigma}'$ of the ordered vector $\mathbf{x}'$, and perform Cholesky decomposition $\mathbf{\Sigma}'^{-1}+\frac{1}{\sigma_v^2}\mathbf{H}^h\hat{\mathbf{H}}=\mathbf{U}\mathbf{\Delta}\mathbf{U}^h$,
- Obtain feedback equalizer matrix $\mathbf{D} = \mathbf{U}^h - \mathbf{I}_{NN_b}$, and calculate feedforward equalizer matrix $\mathbf{C}$ according to (6.31)– (6.33),
- Initialize the soft-decision symbol vector $\hat{\mathbf{x}}'$ to be zero.

MIMO TURBO BDFE ALGORITHM:

FOR $g = NN_b$ TO 1 DO
  Set the mean of $x_{\langle O_g\rangle}$ in $\bar{\mathbf{x}}'$ as zero, to obtain $\bar{\mathbf{x}}'_g$,
  Calculate $\mathbf{z}_g = \mathbf{C}\left(\mathbf{y} - \mathbf{H}\bar{\mathbf{x}}'_g\right)$,
  FOR $q = 1$ TO Q
    Calculate $P\left(x_{\langle O_g\rangle} = \chi_q | z_g\right)$ according to Eqn. (6.26), (6.27).
  END
  FOR $p = 1$ TO $\log_2 Q$
    Calculate bit LLR $\Lambda\left[c_{n_g,(k_g-1)\log_2 Q+p}\right]$ according to (6.29),
    Then calculate bit extrinsic LLR $\Lambda_e\left[c_{n_g,(k_g-1)\log_2 Q+p}\right]$,
  END
  Calculate $\hat{x}_{\langle O_g\rangle}$ based on $P\left(x_{\langle O_g\rangle} = \chi_q | z_g\right)$, and update the tentative soft-decision symbol vector $\hat{\mathbf{x}}'$.
END

OUTPUT:

Extrinsic LLR of coded bits $\Lambda_e\left[c_{n,(k-1)\log_2 Q+p}\right]$
$(1 \le p \le \log_2 Q, 1 \le n \le N, 1 \le k \le N_b)$

constant equalizer is adopted. For each transmission stream, the calculation of the constant equalizer taps involves matrix inversion of size $N(K + L - 1)$. The overall complexity for

calculating equalizer taps is thus in the order of $\mathcal{O}(N^4(K+L-1)^3)$. The LLR calculation also includes the filtering operation and the conditional probability evaluation, requiring overall complexities in the order of $\mathcal{O}(MN^2N_bK(K+L-1))$ and $\mathcal{O}(QN^2N_b(K+L-1))$, respectively.

From the analysis above, the complexity of BDFE is determined by the system block size N_b, and the complexity of LE is closely related to the channel length L and the system parameters K (K_1 and K_2). The complexity comparison between BDFE and LE is then determined by the system parameters N_b, L and K. Since block transmission is primarily designed for fast-fading environment [125], the choice of block size N_b shall not be too large so as to guarantee the time-invariant assumption of the channel. In this case, the proposed BDFE has comparable complexity to LE. For example, for the choice $N_b = 100$, $L = 15$ and $K_1 = K_2 = L$, both BDFE and LE have complexities in the order of $\mathcal{O}(10^6)$. It is noted that once the block size is fixed, the complexity for BDFE remains nearly unchanged within a large range of channel length. The complexity of LE, however, is cubic in the channel length and will get very high for large channel length L.

6.5 Simulation Results

Simulation results are presented in this section to demonstrate the performance of the proposed MIMO turbo BDFE with reliability-based SSIC. The data is organized in packets. Each packet is independently encoded by a rate 1/2 non-systematic convolutional code with a constraint length 4 and a generator polynomial $[G_1, G_2] = [17, 13]_{\text{oct}}$. The encoded packet is further divided into blocks for transmission. The MIMO turbo BDFE is operated over blocks, and the MAP convolutional decoding is performed over an entire packet.

First we compare the performance of the BDFE with fixed and reliability-based SSIC. A 2×2 MIMO system using QPSK modulation is studied. The simulations are performed under two scenarios. In the first scenario, complex MIMO channel is adopted. Each of the subchannels has a length of $L = 5$ with exponential power delay profile (PDP)

$\exp(-0.4l)(0 \leq l \leq L-1)$. Each packet carries 2,000 symbols (or 2,000 information bits), which are divided into 20 blocks with size $N_b = 100$. For the group-wise detection ordering, $N_r = 5$ is selected so that each block is divided into $N_g = 20$ groups. The MIMO channel remains constant over each packet while changes from packet to packet. In the second scenario, real MIMO channel is employed. The MIMO channel is generated with the Proakis Type A channel [82] as $\mathbf{h}_{1,1} = [0.04, -0.05, 0.07, -0.21, -0.5, 0.72, 0.36, 0, 0.21, 0.03, 0.07]$, $\mathbf{h}_{1,2} = \mathbf{h}_{1,1} \ll 3$, $\mathbf{h}_{1,2} = \mathbf{h}_{1,1} \ll 6$, $\mathbf{h}_{1,2} = \mathbf{h}_{1,1} \ll 9$, where $\mathbf{h}_{m,n}$ denotes the subchannel between the n-th transmit antenna and the m-th receive antenna. Each packet carries 1,000 symbols (or 1,000 information bits), which are divided into 10 blocks with size $N_b = 100$. For the group-wise detection ordering, $N_r = 10$ is selected so that each block is divided into $N_g = 10$ groups. During the simulation, 200 packets are simulated for both scenarios. The simulation results are shown in Fig. 6.3 and Fig. 6.4, respectively. From the two figures, it is apparent that extra gains have been obtained for the second and third iterations, by utilizing the *a priori* reliability information for detection ordering. In the first iteration, there is no *a priori* reliability information available, so the BDFE with reliability-based SSIC has the same performance as the original BDFE with fixed SSIC.

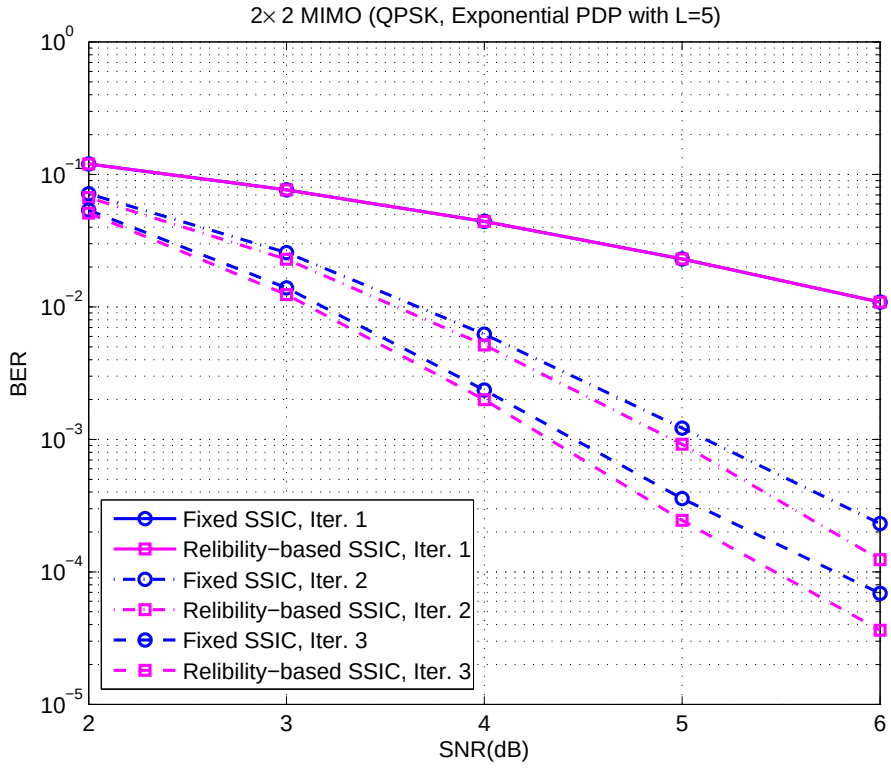

Figure 6.3: BER comparison between fixed and reliability-based SSIC (complex channel)

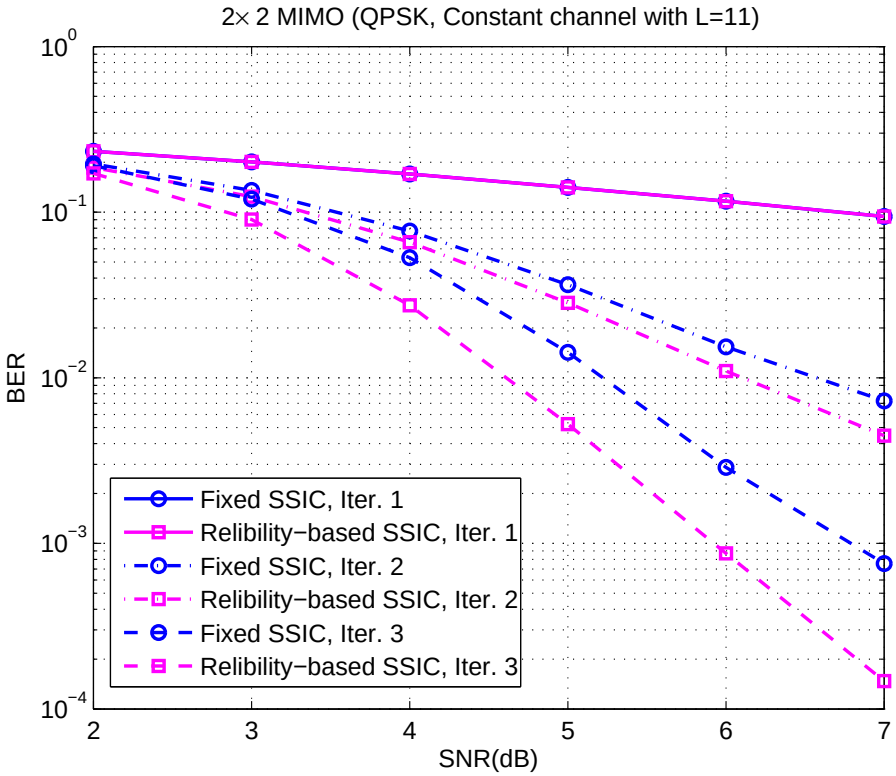

Figure 6.4: BER comparison between fixed and reliability-based SSIC (real channel)

Next we compare the performances of the proposed turbo BDFE and the turbo LE [77]. A 2×2 MIMO system with 8PSK modulation is considered, where the MIMO channel has a uniform PDP with a channel length of $L = 10$. Each packet carries 6,000 symbols (or 9,000 information bits), which are divided into 60 blocks with block size $N_b = 100$. In the simulation, 50 packets are simulated. The parameters K_1 and K_2 are set as $K_1 = K_2 = L$ for LE. The BER results of the two equalization schemes are compared in Fig. 6.5. From the figure, the proposed BDFE significantly outperforms LE and has achieved more than 2 dB gain in all three iterations.

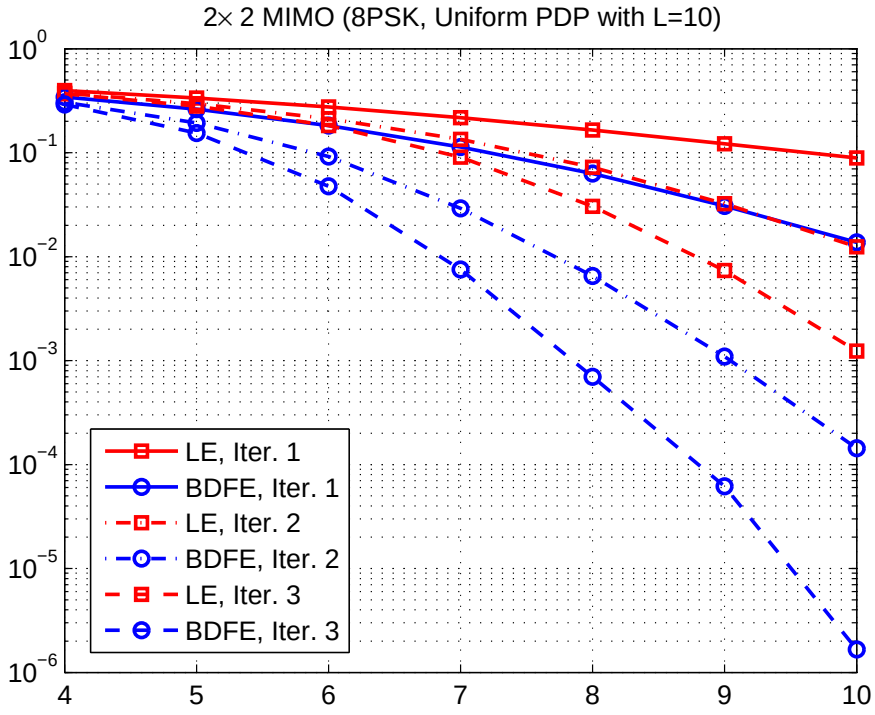

Figure 6.5: 2×2 MIMO: BER comparison for LE and BDFE (8PSK)

Fig. 6.6 compares the performance of the proposed BDFE with the optimum MAP equalizer in a 2×2 MIMO system. Constant MIMO channel with length $L = 3$ is adopted,

which is generated with the Proakis type B [82] channel as $\mathbf{h}_{1,1} = [0.407, 0.815, 0.407]$, $\mathbf{h}_{1,2} = [0.815, 0.407, 0.407]$, $\mathbf{h}_{2,1} = [0.407, 0.407, 0.815]$, and $\mathbf{h}_{2,2} = [0.407, -0.407, 0.815]$. With BPSK modulation, the trellis structure of the MIMO MAP equalization has $Q^{N(L-1)} = 16$ states. Each packet carries 2,000 symbols (or 2,000 information bits), and the block size is $N_b = 100$. The result shown in Fig. 6.6 is simulated with 300 packets. It is observed from the results that when the BER equals to 10^{-2}, the MIMO BDFE is within 0.5 dB from the optimum MAP equalizer, while the LE algorithm is about 1 dB from the MAP equalizer. In addition, only marginal performance improvement is observed by increasing the number of iterations from 4 to 5. Obviously, the proposed BDFE achieves a BER performance close to the optimum MAP equalization.

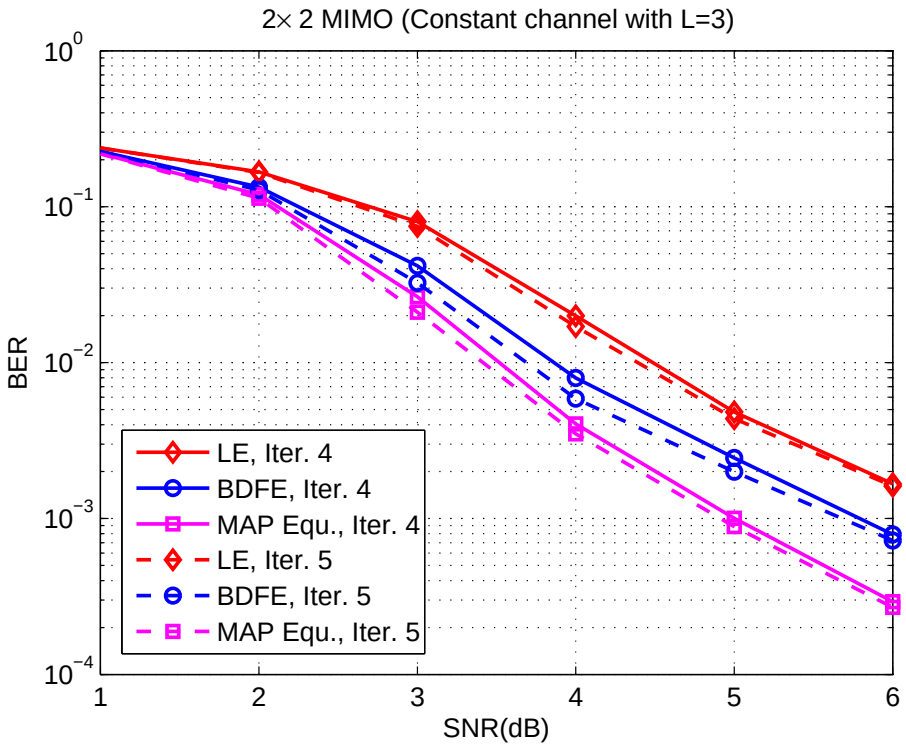

Figure 6.6: BER comparison among LE, BDFE and MAP equalization (BPSK)

6.6 Conclusion

A new turbo block decision feedback equalizer with reliability-based successive soft interference cancelation was proposed for MIMO systems. Compared to existing low-complexity turbo detection schemes, the proposed scheme has two advantages. First, it takes advantage of the degree-of-freedom in the detection ordering of SSIC, and introduces a reliability-based SSIC to reduce error propagation. Second, it utilizes the non-linear BDFE structure, which can achieve a better performance than the linear equalization structure with a similar complexity. In addition, the reliability information was obtained from the soft *a priori* information that is unique to turbo equalization. It was demonstrated through simulations that the proposed MIMO BDFE has a better BER performance and a faster converging rate compared to existing low-complexity algorithms, while retaining similar computation complexity.

Chapter 7

Channel Equalization for MIMO Underwater Acoustic Communications

7.1 Introduction

Underwater acoustic (UWA) channel is recognized as one of the most challenging channels in practical use [90]. The obstacles imposed by the water media on acoustic propagation are reflected in four aspects. First, the available channel bandwidth is very limited due to the frequency-dependent attenuation. For example, in medium-range UWA communications, the bandwidth is on the order of a few tens of kilohertz. Second, the channel delay spread is very long due to the rich scattering environment. For instance, it could be over several tens of milliseconds (ms), leading to an equivalent discrete-time channel with several tens or even hundreds of channel taps in contrast to less than twenty taps in radio frequency (RF) communications. Third, the Doppler effect is very significant due to the low propagation speed of sound (about 1500 m/s in water). On one hand, the motion-induced Doppler shift causes a normalized carrier frequency offset (CFO) on the order of 10^{-4} to 10^{-3}, compared to 10^{-8} to 10^{-6} in RF channels. On the other hand, the motion-induced waveform compression or dilation, incurs non-negligible symbol offset requiring signal resampling. Finally, the temporal variation of the UWA channel is very fast due to the dynamics of the water mass, which imposes difficulty on both channel estimation and phase tracking.

In the past three decades, significant progress has been achieved in UWA communi-

cations [91] – [103]. Earlier UWA communications adopted non-coherent frequency-shift keying (FSK) technology which enabled simple energy-based signal detection combating the unpleasant effect of channel reverberation [91]. The drawback of FSK lies in its low transmission rate and also low bandwidth efficiency. The partial coherent modulation of differential phase shift keying (DPSK) was then chosen to achieve a bandwidth efficiency between non-coherent and fully coherent systems. It was until early 1990's, UWA transmission using the bandwidth-efficient coherent modulation appeared in [92]. Different from FSK, coherent transmission adopting modulations like phase shift keying (PSK) and quadrature amplitude modulation (QAM) requires proper cancelation of inter-symbol interference (ISI) and compensation of phase distortion in signal detection, both tasks become very difficult under hash UWA channel conditions. Passive-phase conjugation (PPC) [93] and time reversal (TR) [94] technologies, both having different principles from equalization, have been proposed to mitigate ISI. The detection using PPC technology, however, has poor performance when only a small number of receiving hydrophones are available [95]. As a result, equalization technology is more commonly adopted for coherent detection. Generally, equalization can be performed in either time-domain (TD) [96] – [100] or frequency-domain (FD) [101] – [103]. In [96], [97], the classic joint design of decision feedback equalizer (DFE) and phase-locked loop (PLL) has been proposed, and its iterative implementation can be found in [98]. In [99], by coupling PPC technology with a single-channel DFE, the correlation-based DFE is proposed and tested to be robust to different acoustic environments. The phase rotation is tracked with PLL technology. In [100], linear equalization combined with proper phase compensation has been proposed to minimize error propagation due to decision feedback. In [101], single-carrier frequency-domain equalization (SC-FDE) followed by phase compensation is proposed for single-carrier systems, and the frequency-domain equalization for multiple-carrier orthogonal frequency division multiplexing (OFDM) systems has been proposed in [102], [103]. In [102], equalization is performed with adaptive channel estimation and phase tracking method. In [103], pilot-aided channel estimation is adopted for equalization, and a two-step Doppler compensation

is adopted to remove phase rotation. While FD equalization enables low-complexity implementation even over highly-dispersive channel, it usually requires extra guard intervals (GI) among transmission blocks, which sacrifices the data transmission efficiency. Moreover, the inherent sensitivity of OFDM systems to carrier frequency offset, makes the robust detection very challenging especially with moving transceivers.

Despite the diverse equalization schemes, the demonstrated data rate of UWA communication is relatively low due to the natural limitation on the available channel bandwidth. In recent years, researchers have started to explore the spatial structure of the oceans to fundamentally improve the transmission rate. In the past years, MIMO UWA communications have been investigated in [104] – [108]. In [104], the number of the available degrees of freedom in the UWA channel is studied. In [105], coherent MIMO transmission has been presented, using a time reversal approach. In [106], the joint DFE and PLL scheme originally proposed in [96] for single input multiple output (SIMO) systems has been extended to MIMO cases. In [107], turbo linear equalization has been used for MIMO UWA communication. The FD equalization schemes proposed in [101] and [103] have also been extended to MIMO systems in [108] and [109], respectively.

In this chapter, we propose a new time-domain MIMO equalization scheme for single carrier UWA communications. Different from conventional schemes performing joint equalization and phase tracking [92], [96], [97], [98], [106], where the requirement for careful tuning of DFE and PLL parameters makes the system less stable [90], the new scheme decouples the interference-cancelation functionality and phase-synchronization functionality leading to a generalized equalizer structure consists of an interference-cancelation (IC) equalizer and a phase compensator. MIMO linear equalizer (LE) is adopted to achieve low-complexity equalization and also to avoid the error propagation in DFE especially under harsh channel conditions. A novel group-wise phase estimation and correction method proposed in [110], which is insensitive to noise disturbance, is used to compensate phase rotations in the equalized symbols. The proposed equalization scheme has been adopted in a layered receiver structure for UWA communications, and has been tested by high-

rate MIMO experimental data measured off the northwestern coast of Kauai, Hawaii, in September 2005, and by both moving-source and fixed-source SIMO experimental data measured at Saint Margaret's Bay, Nova Scotia, Canada, in May 2006. We have achieved successful equalization in both experiments.

The rest of the chapter is organized as follows. In Section 7.2, a general MIMO UWA system model is given. Based on the system model, MIMO channel estimation is introduced in Section 7.3, as the basis for equalizer design. The new MIMO equalization scheme is then developed in Section 7.4, where the MIMO IC equalization, the group-wise phase estimation and compensation, and the layered space-time processing technology are discussed, respectively. Section 7.5 reports the results on experimental data processing, and conclusion is drawn in Section 7.6.

7.2 MIMO UWA System Model

For a MIMO UWA communication system employing N transmitting transducers and M receiving hydrophones, the baseband discrete-time signal received at the m-th hydrophone is represented as

$$\tilde{y}_m(k) = \sum_{n=1}^{N} \sum_{l=0}^{L-1} \tilde{h}_{n,m}(k,l)\tilde{x}_n(k-l)e^{j\tilde{\phi}_{n,m}(k)} + \tilde{v}_m(k) \tag{7.1}$$

where $\tilde{x}_n(k)$ is the effective transmission symbol of the n-th transducer observed at the receiver, $\tilde{h}_{n,m}(k,l)$ and $\tilde{\phi}_{n,m}(k)$ are the l-th complex fading coefficient and the phase drift of the time-varying subchannel between the n-th transducer and the m-th hydrophone, and L is the channel length. The phase drift is a combining effect of the average Doppler shift, $\bar{f}_{n,m}$, the instantaneous Doppler, $f_{n,m}(k)$, and the coarse synchronization phase error, $\theta_{n,m}$, and can be expressed as $\tilde{\phi}_{n,m}(k) = 2\pi \left[\bar{f}_{n,m} + f_{n,m}(k)\right] kT_s + \theta_{n,m}$, where T_s is the symbol interval. The term $\tilde{v}_m(k)$ is the sample of a zero-mean additive white Gaussian noise (AWGN) with power σ_v^2, on the m-th hydrophone. For practical UWA channels, the fading coefficient $\tilde{h}_{n,m}(k,l)$ usually changes slower than the instantaneous phase $\tilde{\phi}_{n,m}(k)$, so it is appropriate to treat them separately [106].

The average Doppler shift $\bar{f}_{n,m}$ is caused by the relative motion between the transmitter and the receiver, while the instantaneous Doppler $f_{n,m}(k)$ modeled as a zero-mean time-varying random variable comes from the dynamics of the oceans. When the transmitter-receiver relative motion is non-negligible, it causes the transmitted signal to be compressed or dilated at the receiver side [111], [112]. In this case, the effective transmission symbol $\tilde{x}_n(k)$ in (7.1) is not exactly the same as the originally transmitted symbol $x_n(k)$, where $x_n(k) \in \mathcal{S}$ with $\mathcal{S} = \{\chi_q\}_{q=1}^{Q}$ being the modulation constellation of size Q. As a result, compensation of the average Doppler shift $\bar{f}_{n,m}$ and re-sampling of the received signal, herein named as Doppler preprocessing, are necessary before signal detection can be performed. An efficient average Doppler shift estimation method has been provided in [111]. After Doppler preprocessing, the signal model in (7.1) becomes

$$y_m(k) = \sum_{n=1}^{N} \sum_{l=0}^{L-1} h_{n,m}(k,l) x_n(k-l) e^{j\phi_{n,m}(k)} + v_m(k) \tag{7.2}$$

where $y_m(k)$, $h_{n,m}(k,l)$, $\phi_{n,m}(k)$ and $v_m(k)$ are the received sample, the fading coefficient, the phase drift and the additive noise after Doppler preprocessing, respectively. The phase term, $\phi_{n,m}(k)$, may contain residual Doppler shift effect due to non-ideal Doppler shift estimation and compensation. The noise $v_m(k)$ is still zero-mean AWGN with variance power σ_v^2.

7.3 Channel Estimation for MIMO UWA Communications

As the basis for equalizer design, channel estimation for UWA communications is developed in this section. In training mode, MIMO channel estimation is performed with pilot symbols $\{p_n(k), 0 \le k < N_p\}_{n=1}^{N}$ from all N transducers. We assume that the time duration of the pilot sequences is less than the channel coherence time, in which case the fading coefficient $h_{n,m}(k,l)$ in (7.2) can be treated as approximately time-invariant, *i.e.*, $h_{n,m}(k,l) \approx h_{n,m}(l)$. The assumption is appropriate in many UWA communications. Then

(7.2) can be represented in matrix form as

$$\mathbf{y}_m = \sum_{n=1}^{N} \mathbf{\Phi}_{n,m}\mathbf{P}_n\mathbf{h}_{n,m} + \mathbf{v}_m \tag{7.3}$$

where $\mathbf{y}_m = [y_m(L-1), y_m(L), \cdots, y_m(N_p-1)]^t \in \mathcal{C}^{(N_p-L+1)\times 1}$ is the received sample vector at the m-th hydrophone with $(\cdot)^t$ denoting matrix transpose operation,

$$\mathbf{P}_n = \begin{bmatrix} p_n(L-1) & \cdots & p_n(1) & p_n(0) \\ p_n(L) & \cdots & p_n(2) & p_n(1) \\ \vdots & \ddots & \ddots & \vdots \\ p_n(N_p-1) & \cdots & p_n(N_p-L+1) & p_n(N_p-L) \end{bmatrix} \tag{7.4}$$

is the n-th pilot matrix, and $\mathbf{\Phi}_{n,m} = \text{diag}\left\{e^{j\phi_{n,m}(L-1)}, e^{j\phi_{n,m}(L)}, \cdots, e^{j\phi_{n,m}(N_p-1)}\right\}$, $\mathbf{h}_{n,m} = [h_{n,m}(0), h_{n,m}(1), \cdots, h_{n,m}(L-1)]^t$, and $\mathbf{v}_m = [v_m(L-1), v_m(L), \cdots, v_m(N_p-1)]^t$ are the phase drift matrix, the fading coefficient vector, and the noise vector, respectively. The operator diag$\{\cdot\}$ returns a diagonal matrix. It is still difficult to estimate $\mathbf{h}_{n,m}$ and $\mathbf{\Phi}_{n,m}$ simultaneously from (7.3), due to the separation of $\mathbf{\Phi}_{n,m}$ and $\mathbf{h}_{n,m}$ by $\mathbf{P}_n$ on the right hand side. To proceed, we rewrite $\mathbf{\Phi}_{n,m}$ as

$$\mathbf{\Phi}_{n,m} = e^{j\phi_{n,m}(I)} \times \text{diag}\left\{e^{j[\phi_{n,m}(L-1)-\phi_{n,m}(I)]}, e^{j[\phi_{n,m}(L)-\phi_{n,m}(I)]}, \cdots, e^{j[\phi_{n,m}(N_p-1)-\phi_{n,m}(I)]}\right\} \tag{7.5}$$

where the index I in $\phi_{n,m}(I)$ is determined as $I = \lceil (N_p + L - 2)/2 \rceil$ with $\lceil x \rceil$ denoting the smallest integer larger than x. The instantaneous phase drifts $\{\phi_{n,m}(k)\}_{k=L-1}^{N_p-1}$ in (7.5) could be significant. However, the differential phase drifts $\{\phi_{n,m}(k) - \phi_{n,m}(I)\}_{k=L-1}^{N_p-1}$ will be insignificant over a short period of time. Thus (7.5) can be approximated by $\mathbf{\Phi}_{n,m} \approx e^{j\phi_{n,m}(I)}\mathbf{I}_{N_p-L+1}$ with $\mathbf{I}_j$ being an identity matrix of order j. Then (7.3) can be approximated by

$$\begin{aligned} \mathbf{y}_m &\approx \sum_{n=1}^{N} \mathbf{P}_n \left[e^{j\phi_{n,m}(I)}\mathbf{h}_{n,m}\right] + \mathbf{v}_m \\ &= \mathbf{P}\mathbf{h}_m + \mathbf{v}_m. \end{aligned} \tag{7.6}$$

where $\mathbf{P} = [\mathbf{P}_1, \mathbf{P}_2, \cdots, \mathbf{P}_N]$ and $\mathbf{h}_m = \left[e^{j\phi_{1,m}(I)}\mathbf{h}_{1,m}^t, e^{j\phi_{2,m}(I)}\mathbf{h}_{2,m}^t, \cdots, e^{j\phi_{N,m}(I)}\mathbf{h}_{N,m}^t\right]^t$. From (7.6), the minimum mean square error (MMSE) estimation of $\mathbf{h}_m$ is given by

$$\hat{\mathbf{h}}_m = \left(\mathbf{P}^h\mathbf{P} + \sigma_v^2\mathbf{I}_{NL}\right)^{-1}\mathbf{P}^h\mathbf{y}_m \tag{7.7}$$

where $(\cdot)^h$ denotes matrix Hermitian transpose. The estimation in (7.7) is performed on all M hydrophones to obtain MIMO channel estimation. It is noted that to guarantee the system equation (7.6) not to be under-determined, a minimum of $N_p \geq (N+1)L-1$ pilot symbols are required for each of the N transducers. Last, the same channel estimation procedure discussed above will also be adopted in the decision-directed mode, where the previously detected symbols instead of the pilot symbols are used for channel estimation.

7.4 New Equalization Scheme for MIMO UWA Communication

A new equalization scheme is discussed in this section, where the conventional equalization is first adopted to cancel the space-time interference among transmitted symbols, and then a novel phase estimation and compensation method is applied to remove the phase rotations in the equalized symbols. The layered receiver structure adopting the proposed equalization scheme is then demonstrated.

7.4.1 MIMO Equalization for Space-Time Interference Cancelation

With the estimated MIMO channel, MIMO equalization can be performed. MIMO linear equalizer is adopted in this chapter. In this case, the k-th equalized symbol of the n-th transmission stream (from the n-th transducer), is given by

$$\hat{x}_n(k) = \sum_{m=1}^{M} \sum_{q=-K_1}^{K_2} c_{n,m}^{(q)}\, y_m(k-q) \tag{7.8}$$

where K_1, K_2 are nonnegative integers, and $c_{n,m}^{(q)}$ denotes the q-th linear equalizer coefficient corresponding to the received sample of the m-th hydrophone for equalizing symbols of the n-th stream. Without loss of generality, the same values of K_1, K_2 are used for all (n, m) pairs, resulting in $N \times M \times (K_1+K_2+1)$ equalizer taps in total.

Collecting the equalized symbols at time k, $\{\hat{x}_n(k)\}_{n=1}^{N}$, of all N streams in a vector,

leads to the matrix-form equalization model as

$$\hat{\mathbf{x}}(k) = \mathbf{C}\mathbf{y} \tag{7.9}$$

where $\hat{\mathbf{x}}(k) = [\hat{x}_1(k), \cdots, \hat{x}_N(k)]^t \in \mathcal{C}^{N\times 1}$, $\mathbf{y} = [\mathbf{y}^t(k-K_2), \cdots, \mathbf{y}^t(k), \cdots, \mathbf{y}^t(k+K_1)]^t \in \mathcal{C}^{M(K_1+K_2+1)\times 1}$ and $\mathbf{C} = \left[\mathbf{c}^{(K_2)}, \mathbf{c}^{(K_2-1)}, \cdots, \mathbf{c}^{(-K_1)}\right] \in \mathcal{C}^{N\times M(K_1+K_2+1)}$ with $\mathbf{y}(k-q) \in \mathcal{C}^{M\times 1}$ and $\mathbf{c}^{(q)} \in \mathcal{C}^{N\times M}$ defined, respectively, as

$$\mathbf{y}(k-q) = [y_1(k-q), y_2(k-q), \cdots, y_M(k-q)]^t \tag{7.10a}$$

$$\mathbf{c}^{(q)} = \begin{bmatrix} c_{1,1}^{(q)} & c_{1,2}^{(q)} & \cdots & c_{1,M}^{(q)} \\ c_{2,1}^{(q)} & c_{2,2}^{(q)} & \cdots & c_{2,M}^{(q)} \\ \vdots & \vdots & \cdots & \vdots \\ c_{N,1}^{(q)} & c_{N,2}^{(q)} & \cdots & c_{N,M}^{(q)} \end{bmatrix}. \tag{7.10b}$$

To solve the equalizer matrix $\mathbf{C}$ in (7.9), the mean squared error (MSE) is applied leading to the cost function defined as follows

$$J(\mathbf{C}) = \mathbb{E}\left[\|\mathbf{x}(k) - \hat{\mathbf{x}}(k)\|^2\right] \tag{7.11}$$

where $\|\mathbf{a}\|$ is the Euclidean norm of vector $\mathbf{a}$, and $\mathbb{E}[\cdot]$ denotes mathematical expectation. By minimizing $J(\mathbf{C})$ in (7.11), the MMSE MIMO LE matrix is solved as

$$\mathbf{C}_{\text{MMSE}} = \mathbb{E}\left[\mathbf{x}(k)\mathbf{y}^h\right]\left\{\mathbb{E}\left[\mathbf{y}\mathbf{y}^h\right]\right\}^{-1} \tag{7.12}$$

which is further simplified as

$$\begin{aligned} \mathbf{C}_{\text{MMSE}} &= \mathbf{R}^h\mathbf{H}^h\left(\mathbf{H}\mathbf{H}^h + \frac{1}{\beta}\mathbf{I}_{M(K_1+K_2+1)}\right)^{-1} \\ &= \mathbf{R}^h\left(\mathbf{H}^h\mathbf{H} + \frac{1}{\beta}\mathbf{I}_{N(K_1+K_2+L)}\right)^{-1}\mathbf{H}^h \end{aligned} \tag{7.13}$$

where the derivation details are referred to the Appendix. In (7.13), the definitions of the channel matrix $\mathbf{H}$, the normalized transmission symbol correlation matrix $\mathbf{R}$, and the signal-to-noise ratio (SNR), are referred to (B.4), (B.6b), and (B.7), respectively. Since $\mathbf{R}$ is constant, the MIMO LE matrix only depends on the knowledge of MIMO channel and SNR.

Remark: in (7.13), two alternative solutions for the MIMO LE matrix $\mathbf{C}$ are provided. In the first solution (first equality), matrix inversion of order $M(K_1+K_2+1)$ is required. In the second solution, matrix inversion of order $N(K_1+K_2+L)$ is involved. Since matrix inversion is the main source of the computational complexity, the solution with smaller-order matrix inversion is always favored in practical MIMO systems.

With the designed LE matrix in (7.13), equalization can then be performed. Substituting (7.2) into (7.9), the equalized symbol of the n-th stream (or the n-th element in $\hat{\mathbf{x}}(k)$) is expressed as

$$\hat{x}_n(k) = \sum_{m=1}^{M} \left[\sum_{q=-K_1}^{K_2} \sum_{i=1}^{N} \sum_{l=0}^{L-1} c_{n,m}^{(q)} h_{i,m}(k-q,l) x_i(k-q-l) e^{j\phi_{i,m}(k-q)} \right] + \eta_n(k) \qquad (7.14)$$

where $\eta_n(k) = \sum_{m=1}^{M} \sum_{q=-K_1}^{K_2} c_{n,m}^{(q)} v_m(k-q)$ is the collection of additive noise $\{v_m(k)\}_{m=1}^{M}$ in the equalized symbol. As we can see from (7.14), the triple summation in the square bracket is the m-th hydrophone's contribution to the equalized symbol of the n-th stream. Therefore, we have the following definition

$$\alpha_{n,m}(k)x_n(k) + \xi_{n,m}(k) \triangleq \sum_{q=-K_1}^{K_2} \sum_{i=1}^{N} \sum_{l=0}^{L-1} c_{n,m}^{(q)} h_{i,m}(k-q,l) x_i(k-q-l) e^{j\phi_{i,m}(k-q)} \qquad (7.15)$$

where $\alpha_{n,m}(k)$ denotes the scaling factor which is usually a complex value closely related to the equalizer taps $c_{n,m}^{(q)}$ and instantaneous phase rotation $e^{j\phi_{i,m}(k-q)}$, and $\xi_{n,m}(k)$ denotes residual interference from symbols other than $x_n(k)$. With above definition, (7.14) is simplified as

$$\begin{aligned} \hat{x}_n(k) &= \sum_{m=1}^{M} \alpha_{n,m}(k) x_n(k) + \xi_n(k) + \eta_n(k) \\ &= |\gamma_n(k)|\, e^{j\angle\gamma_n(k)} x_n(k) + \zeta_n(k) \end{aligned} \qquad (7.16)$$

where $\gamma_n(k) = \sum_{m=1}^{M} \alpha_{n,m}(k)$ is the diversity combining gain of M hydrophones, $\xi_n(k) = \sum_{m=1}^{M} \xi_{n,m}(k)$ is the overall residual interference, and $\zeta_n(k) = \xi_n(k) + \eta_n(k)$ is the effective noise consists of the residual interference and additive noise in the equalized symbol. Obviously, regardless of the effective noise, the equalized symbol $\hat{x}_n(k)$ in (7.16), is an

amplitude-scaled and phase-rotated version of the original symbol $x_n(k)$. The phase rotation $\angle\gamma_n(k)$ is a complicated term caused by phase drift $\phi_{n,m}(k)$. For systems employing coherent modulation schemes like phase shift keying (PSK), the phase rotation is hostile and must be compensated, which is the topic of the next subsection.

7.4.2 Group-wise Phase Estimation and Compensation

The group-wise phase estimation and correction method proposed in [110] is adopted to handle the phase rotations in the equalized symbol $\hat{x}_n(k)$, as shown in (7.16). The motivation for the group-wise phase estimation and correction method comes from the fact that the instantaneous phase drift $\phi_{n,m}(k)$ changes gradually while not arbitrarily from time to time due to the nature of ocean waters. In other words, the rotating phase $\angle\gamma_n(k)$ tends to be a constant over a small group of N_s consecutive equalized symbols. The procedure for performing the group-wise phase estimation and compensation algorithm is presented in the following.

Initialization: For the equalized data block of size N_b, designate the first N_{ts} symbols $\{x_n(k)\}_{k=1}^{N_{ts}}$ as the training symbols for phase reference and determine the initial phase $\psi_n(0)$ by

$$\psi_n(0) = \frac{1}{N_{ts}} \sum_{k=1}^{N_{ts}} \left[\angle\hat{x}_n(k) - \angle x_n(k)\right]. \tag{7.17}$$

Then, partition the remaining $N_b - N_{ts}$ symbols into N_g groups, each having N_s symbols, except that the N_g-th group may have less than N_s symbols. Further, for a M-ary PSK (MPSK) modulation constellation $\mathcal{S}_M = \left\{\exp\left[\frac{j(m-1)2\pi}{M}\right]\right\}_{m=1}^{M}$, define a phase quantization function $\mathbb{Q}[\cdot]$ as follows

$$\mathbb{Q}[\phi] = \frac{2(m-1)\pi}{M}, \qquad \begin{matrix}\frac{(2m-3)\pi}{M} \le \phi < \frac{(2m-1)\pi}{M} \\ m = 1, 2, \cdots, M.\end{matrix} \tag{7.18}$$

Set $g = 1$.

Step 1: Compensate the phase of the g-th group data by $e^{-j\psi_n(g-1)}$, yielding

$$\hat{x}_n(g,k) = \hat{x}(N_{ts} + (g-1)N_s + k)e^{-j\psi_n(g-1)}, \;\; k = 1, 2, \cdots, N_s. \tag{7.19}$$

Step 2: For each symbol in the g-th group, calculate its phase deviation from the corresponding nominal phase as

$$\varphi_n(g,k) = \angle\hat{x}_n(g,k) - \mathbb{Q}\left[\angle\hat{x}_n(g,k)\right], \quad k = 1, 2, \cdots, N_s. \tag{7.20}$$

Step 3: Calculate the average phase deviation and estimate the rotating phase, respectively, for the g-th group as

$$\Delta\psi_n(g) = \frac{1}{N_s}\sum_{k=1}^{N_s}\varphi_n(g,k) \tag{7.21}$$

$$\psi_n(g) = \psi_n(g-1) + \Delta\psi_n(g). \tag{7.22}$$

Step 4: Increment g by 1, repeat Step 1 – 3 till $g = N_g$.

After estimating the phases for the N_g groups, we can compensate the phase rotation in the equalized symbols on group basis as

$$\check{x}_n(g,k) = \hat{x}_n(g,k)e^{-j\psi_n(g)}, \quad \begin{matrix} k = 1, 2, \cdots, N_s \\ g = 1, 2, \cdots, N_g \end{matrix} \tag{7.23}$$

The phase-compensated symbol $\check{x}_n(g,k)$ is then ready for detection. It is pointed out that if the last group has less than N_s symbols, then the calculation through (7.19)–(7.23) needs to be carried out based on the actual number of symbols. Finally, the group-wise phase estimation method takes the advantage of insensitivity to noise perturbations, due to the averaging operation in (7.21).

7.4.3 Layered Space-Time Processing

Layered space-time processing was first proposed in [113], for frequency-flat fading channels. It was extended to frequency-selective fading channels in [114]. The basic idea of the layered time-space processing is to detect multiple data streams one by one in a specific order [115], so that the overall detection performance of all streams can be improved compared to joint detection.

In [114], the layered time-space processing is operated with the ordered successive interference cancelation (OSIC), where the transmitted streams are detected in an order

that strong streams are detected earlier than weak streams, and each stream is processed with the interference from all previously detected streams already canceled out. For a MIMO UWA communication system using space-time trellis coding (STTC) [116], a layered receiver structure adopting the proposed equalization scheme discussed above is demonstrated in Fig. 7.1, where N stages each detecting one of the N transmission streams, are included. At each stage, channel equalization and phase compensation are operated separately.

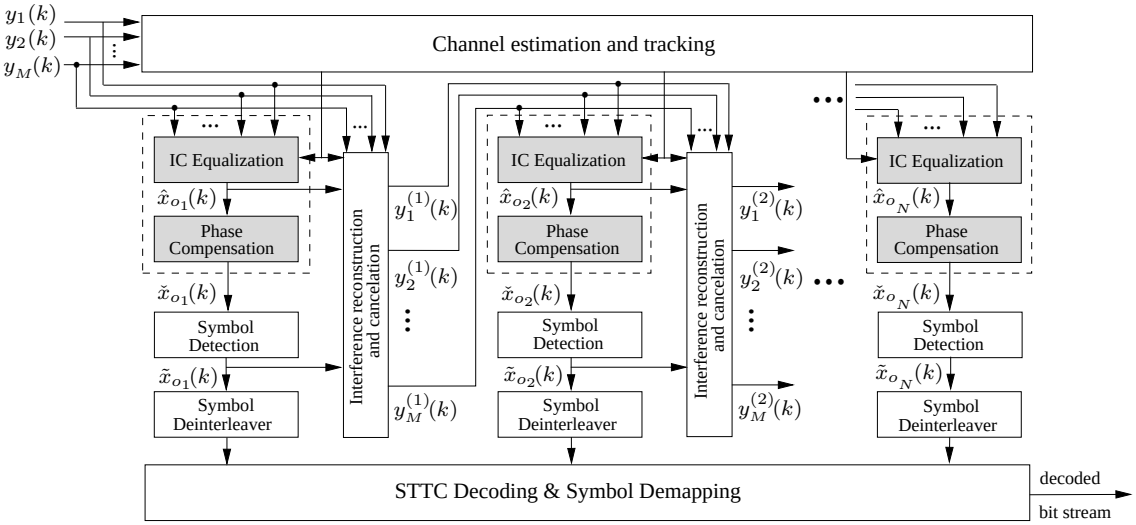

Figure 7.1: Layered MIMO receiver architecture adopting the proposed equalization.

The key for the success of OSIC-based space-time processing lies in the successive interference reconstruction and cancelation. For a detection order $\{o_1, o_2, \cdots, o_N\}$ with o_n denoting the index of the stream detected at stage $n(1 \le n \le N)$, the constructed interference of the o_n-th stream after it is detected, is given as

$$\hat{I}_{o_n,m}(k) = \sum_{l=0}^{L-1} h_{o_n,m}(k,l)\bar{x}_{o_n}(k), \qquad (1 \le m \le M) \tag{7.24}$$

where $\bar{x}_{o_n}(k) = \tilde{x}_{o_n}(k)e^{j[\angle\hat{x}_{o_n}(k) - \angle\tilde{x}_{o_n}(k)]}$ with $\hat{x}_{o_n}(k)$ and $\tilde{x}_{o_n}(k)$ being the equalized symbol and the detected symbol of the o_n-th stream, respectively, as shown in Fig. 7.1. The reconstructed interference of the o_n-th stream is then canceled out as

$$y_m^{(n)}(k) = y_m^{(n-1)}(k) - \hat{I}_{o_n,m}(k), \qquad (1 \le m \le M) \tag{7.25}$$

where $y_m^{(n)}(k)$ denotes the received signal with the interference of the previous n streams already subtracted out, and is ready to be used for detecting the o_{n+1}-th stream. When detecting the o_1-th stream, we have $y_m^{(0)}(k) = y_m(k)$. The procedure in (7.24)–(7.25) is repeated until all streams are detected.

7.5 Experimental Results

The layered receiver structure adopting the proposed equalization scheme as shown in Fig. 7.1, has been tested by two undersea experiments: Makai05 and Unet06. We present the details on data processing for both experiments in this section.

7.5.1 Results of Makai05 Experiment

Single-band (SB) and multi-band (MB) MIMO underwater experiments were conducted off the northwestern coast of Kauai, Hawaii, in September 2005. In MB experiment, six signal bands each having a symbol rate of 2 kilo-symbols per second (ksps) were used. The adoption of MB transmission aims to reduce the equivalent symbol-spaced channel length (thus reduce the equalization complexity), while still achieve a high data rate. Its spectral efficiency, however, is lower than SB transmission due to the insertion of guard bands among multiple signal bands. Signal detection for MB transmission has been presented in [106], and no results for SB transmission has been previously reported yet.

In this chapter, we focus on SB experiment, which further includes low band (LB) transmission and high band (HB) transmission. In LB transmission, the carrier frequency was $f_c = 32$ kHz and the symbol interval was 0.1 ms. The occupied channel bandwidth was $f_b = 14$ kHz due to the use of a pulse shaping filter with roll-off factor 0.4. In HB transmission, the carrier frequency was $f_c = 37.5$ kHz and the symbol interval was 0.05 ms. The occupied channel bandwidth was $f_b = 25$ kHz due to a pulse shaping filter with roll-off factor 0.25. The modulations included BPSK, QPSK and 8PSK for both LB and HB transmissions. The transmitter was a ten-transducer array with 2 meters separation between adjacent transducer elements and was deployed over the side of the Kilo Moana

research vessel. The receiver consisted of eight hydrophones with 2 meters separation between adjacent hydrophone elements, and was allowed to drift freely. The transmission range was 2 kilometers (km).

In Fig 7.2, the signalling for a two-transducer transmission is shown. From the figure,

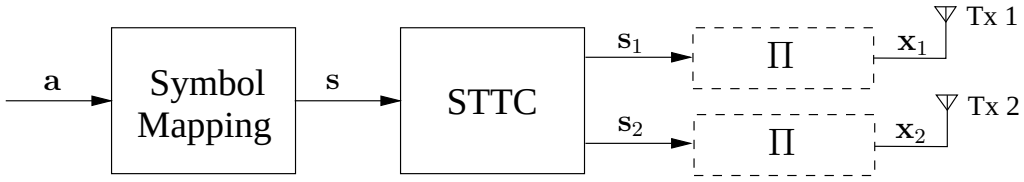

Figure 7.2: Signalling at the transmitter in Makai05 experiment.

the binary stream $\mathbf{a}$ is input to the symbol mapping module with the output modulation symbol stream denoted by $\mathbf{s}$. The symbol stream $\mathbf{s}$ is then encoded by space-time trellis coding, and the encoded stream is de-multiplexed into two sub-streams $\mathbf{s}_1$ and $\mathbf{s}_2$ for two transducers. In this experiment, the four-state BPSK, four-state QPSK, and eight-state 8PSK STTC codes provided in [116] were used, all for two-transducer transmission. Symbol interleavers ($\prod$) were optionally used to transform $\mathbf{s}_1$ and $\mathbf{s}_2$ into $\mathbf{x}_1$ and $\mathbf{x}_2$ ($\mathbf{s}_1 = \mathbf{x}_1$ and $\mathbf{s}_2 = \mathbf{x}_2$ when symbol interleaving was not applied). For the transmission with more than two transducers, the grouped STTC was used, with the details referred to [106].

The symbol stream was transmitted in packets. In Fig. 7.3, the MIMO packet structure is shown. From the figure, the packet consists of three parts: the first part contains

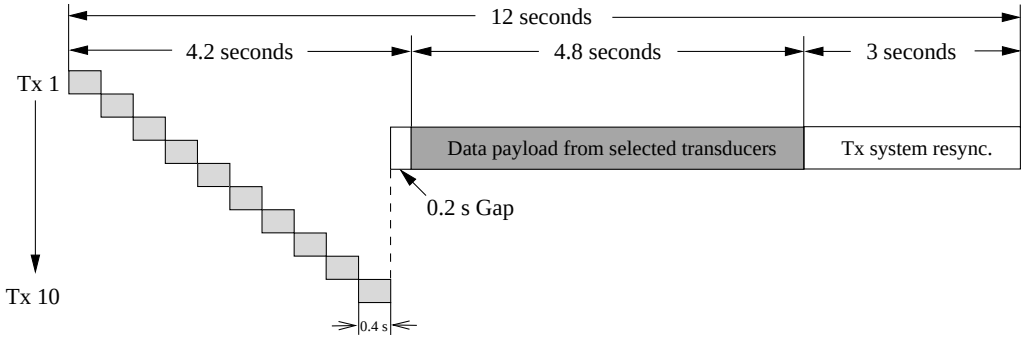

Figure 7.3: MIMO packet structure in Makai05 experiment.

a sequence of probe signals transmitted by transducer one to transducer ten, plus a 0.2-

second clear time. Each probe signal has a duration of 0.4 seconds and contains a linear frequency modulation (LFM) signal for synchronization. The second part contains data payload transmitted simultaneously by designated transducers depending on the experimental configuration. It has a time duration of 4.8 seconds. At the receiver side, part of the transmitted symbols will be used as pilot symbols for channel estimation, which will become evident shortly. The last part is a 3-second clear time used for transmission system re-synchronization. The whole packet has a time duration of 12 seconds.

The signal detection procedures for LB transmission and HB transmission are similar, and we present the details for LB transmission without loss of generality. As mentioned above, the LFM signal contained in the probe signal is used for packet synchronization due to its good correlation property. Moreover, the channel length L can also be estimated with the LFM signals by measuring the span of the significant LFM correlation [100]. In Fig. 7.4, an example of the normalized LFM correlation is depicted. It's clearly shown that there

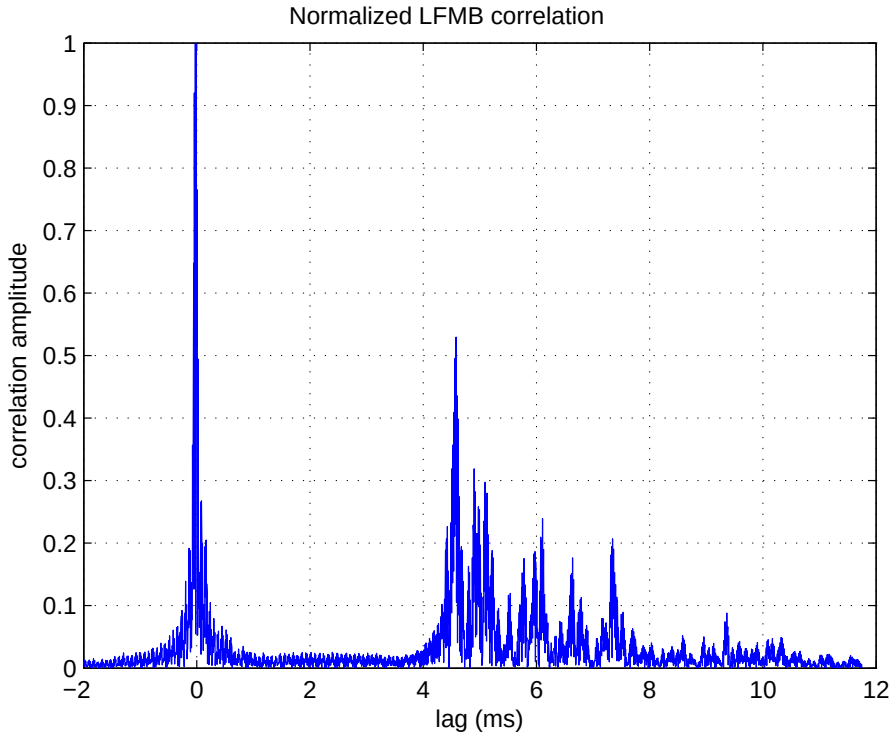

Figure 7.4: An example of normalized LFM correlation.

exists a correlation peak indicating the synchronization point. The significant correlation

spans a range about 10 ms, over which most of the channel energy is concentrated. The channel length is thus estimated as $L = 100$, in terms of LB symbol interval $T_s = 0.1$ ms.

Once the packet synchronization was achieved, the MIMO channel was initially estimated using pilot symbols located at the front of the data payload with the method described in Section 7.3. For the channel length of $L = 100$ requiring a minimum training length of 299 with two-transducer MIMO transmission, a larger pilot length $N_p = 600$ was selected so as to obtain an accurate channel estimation and also mitigate the effect of additive noise. Such choice of pilot length corresponds to a time duration of 60 ms, which is less than the channel coherence time about 200 ms corresponding to a maximum Doppler spread between $2 \sim 3$ Hz in this experiment. The approximation of phase drift in (7.6) is also appropriate in this case, since the maximum possible differential phase drift is less than $\frac{\pi}{8}$. Figs. 7.5 and 7.6 show two examples of the estimated channel impulse responses (CIRs) for the two-transducer eight-hydrophone MIMO transmissions with BPSK and QPSK modulations, respectively. Obviously, all subchannels are sparse with two

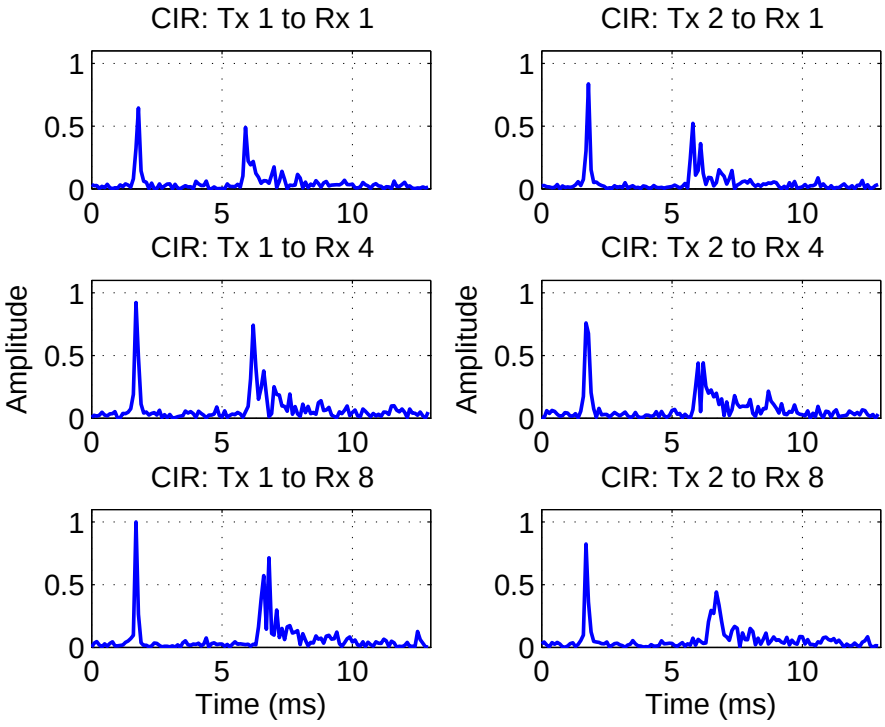

Figure 7.5: Estimated channel impulse responses for 2×8 MIMO with BPSK modulation.

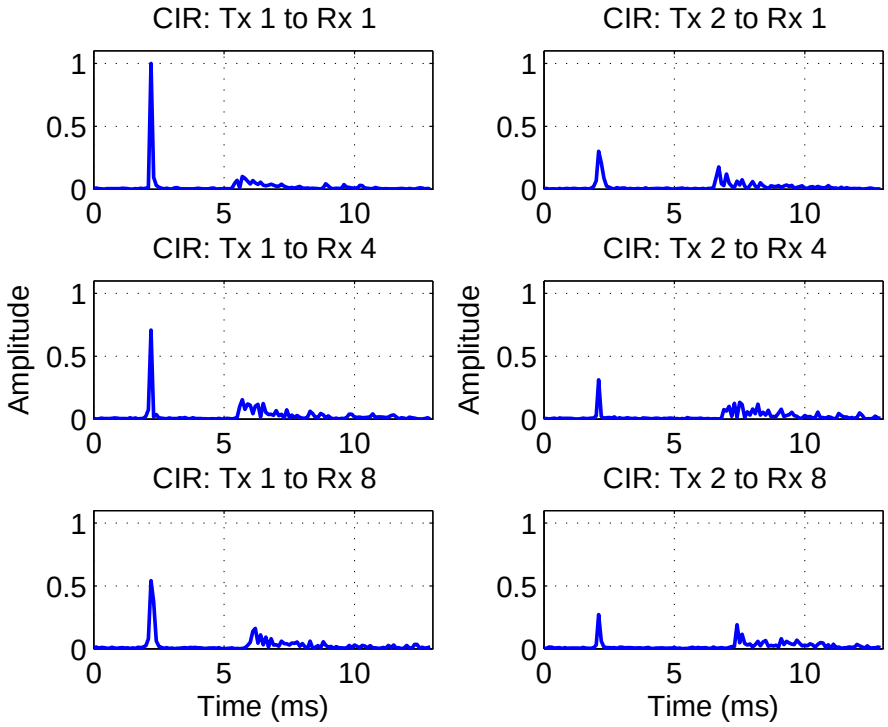

Figure 7.6: Estimated channel impulse responses for 2×8 MIMO with QPSK modulation.

distinct peaks over the depicted delay spread. The estimated MIMO channel with 8PSK modulation was similar to that depicted in Fig. 7.6, and is not shown for brevity. The estimated channel was also used to determine the detection order in the layered space-time processing. For each stream (transducer), its *related channel energy* is defined as the summation of all related subchannel energies. Then a simple ordering criteria is to compare the *related channel energies* among streams, and the stream having larger *related channel energy* is detected earlier.

Periodic pilot sequences were inserted to divide the data payload into frames, and each frame was artificially partitioned into blocks for processing, as shown in Fig 7.7. We chose the block size $N_b = 200$, corresponding to 20 ms. The initial MIMO channel estimation was employed to detect the block following the first pilot sequence, using the layered detection scheme. In each layer, N_b symbols of the corresponding stream were first equalized. The LE parameters K_1 and K_2 in (7.8), were selected as $K_1 = K_2 = L-1$. An interesting observation was that using smaller $K_2 < L$ only slightly degraded the equalization performance while

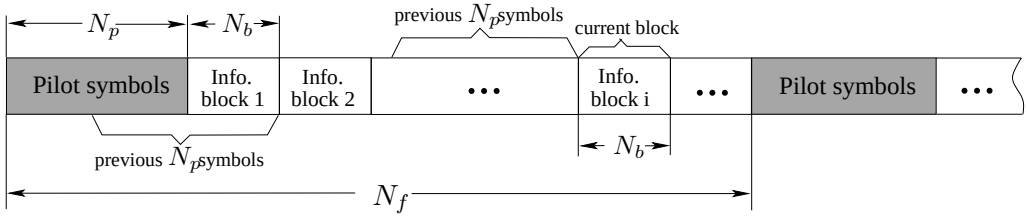

Figure 7.7: Partition of the transmitted data payload for block detection at the receiver.

decreased the computational complexity considerably. The N_b equalized symbols were then fed into the phase compensation unit, as shown in Fig. 7.1. In the operation of group-wise phase estimation and correction, the group size $N_s = 20$ was used, and there were $N_g = 10$ groups in one block. After phase compensation, the N_b symbols were detected. The detected symbols together with the equalized symbols were also used to construct the interference of the detected stream, which was subtracted out of the received signal for detecting the next stream. The block processing was finished when all N streams were detected. To effectively track the time variation of MIMO channel, N_p previously detected symbols (part of them could be pilot symbols) of all streams were used to re-estimate the channel, as shown in Fig 7.7. The updated channel was then used to detect the current data block in a similar way mentioned above. The channel re-estimation and detection procedure continued until the next pilot sequence started. The insertion of periodic pilot sequences aimed to combat possible error propagation of decision-directed channel re-estimation, and the new frame was processed in the same way as the previous one. The frame size was selected to achieve a tradeoff between detection performance and training overhead. In the processing, we selected $N_f = 16,000$ which incurred only 5% overall training overhead, comparing to 20% training overhead with conventional algorithms [106,117]. Once an entire packet was detected, the N symbol streams were de-interleaved (if the symbol interleaver was used) and then sent to the STTC decoding and symbol demapping module to produce the decoded information bit stream, as shown in Fig. 7.1. The STTC decoding was easily implemented with Viterbi algorithm.

In Fig. 7.8, the sequence of estimated CIRs obtained during packet detection are de-

picted, where the temporal variations of the four subchannels are clearly shown over the depicted time interval within one packet. In Fig. 7.9, the scatter plot shows two chan-

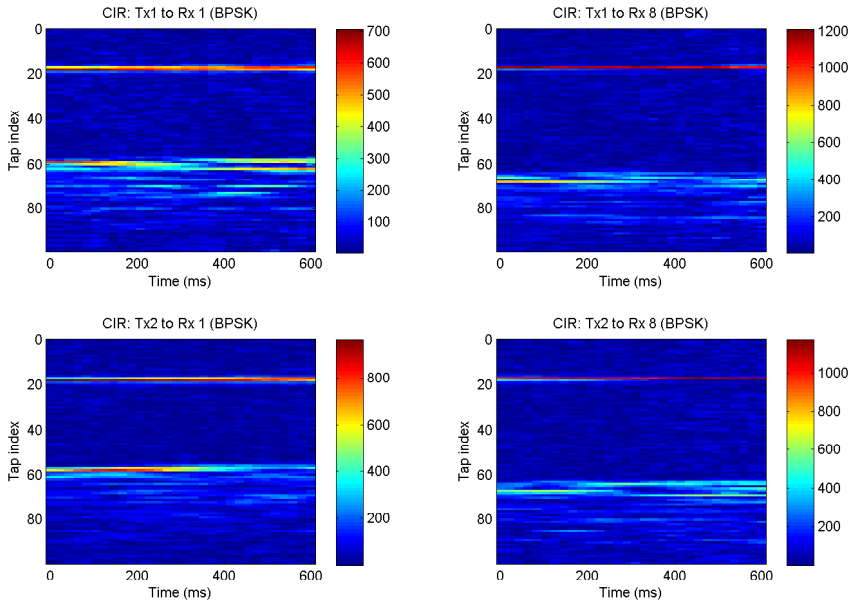

Figure 7.8: Demonstration of channel variation within one packet.

nels (hydrophone one and hydrophone eight) of received baseband signal, and the equalized and phase-corrected BPSK symbols of transducer one for a 2×8 MIMO packet. In the bottom-left subfigure, the phase rotations in the equalized symbols are obvious when comparing with the phase-corrected symbols shown in the bottom-right subfigure. The phase-corrected symbols have been properly classified into two clusters centered at the two nominal BPSK modulation symbols -1 and $+1$. Similar observations are found with the equalized and phase-corrected QPSK and 8PSK symbols, as depicted in Fig. 7.10. All demonstrations have therefore verified the necessity and effectiveness and of the phase compensation operation.

From the available experimental data, we had eight 2×8 BPSK packets, three 2×8 QPSK packets, and two 2×8 8PSK packets for LB transmission. We processed all these packets with the proposed detection scheme, and the bit error rate (BER) results for the 2×8 MIMO transmission with BPSK, QPSK and 8PSK modulations are listed in

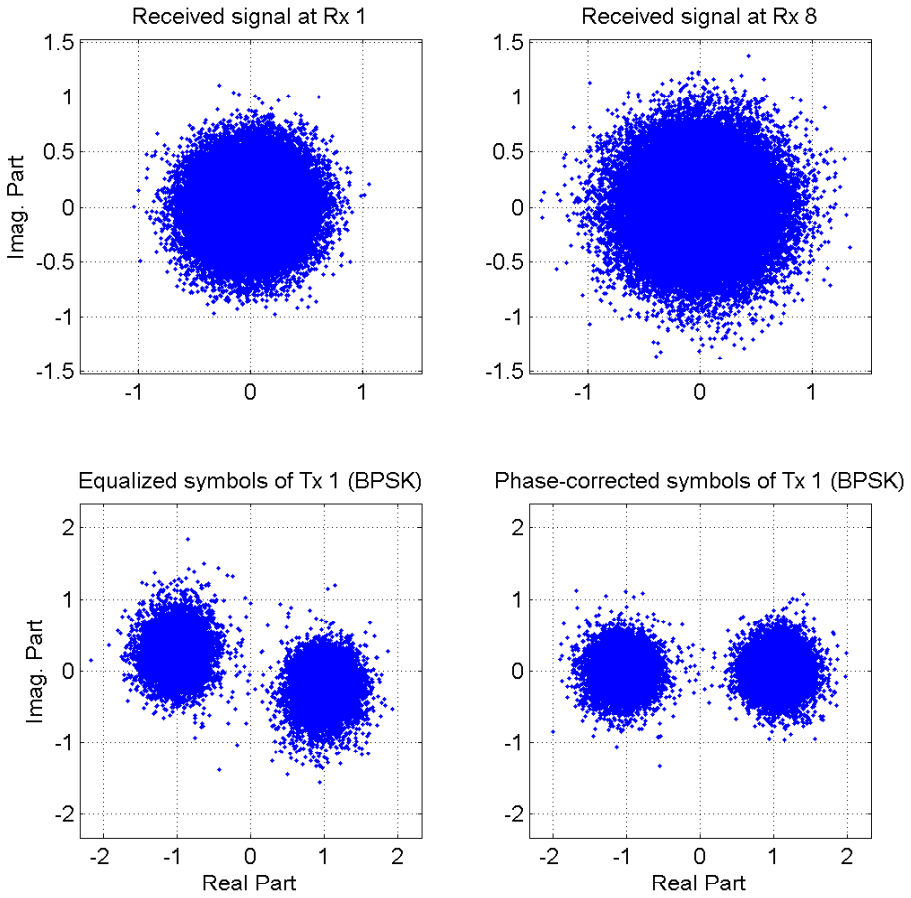

Figure 7.9: Received baseband signal, equalized and phase-corrected BPSK symbols

Table 7.1 through Table 7.3. It is noted that symbol interleaving was applied only to even-indexed packets in all three tables. From these tables, we make three observations. First, the BER performance degrades when the size of the constellation size increases, by comparing the average uncoded BERs listed in the last lines of the three tables. Second, the average uncoded BERs of the two streams are comparable with BPSK modulation, while the first stream has better average uncoded BER than that of the second stream with QPSK and 8PSK modulations. This phenomenon is well explained by the fact that the two streams have similar *related channel energy* in BPSK case as shown in Fig 7.5. In contrast, stream one has a larger *related channel energy* than stream two in QPSK case, as shown in Fig. 7.6. Third, the BER performance of all packets are improved with STTC decoding. The even-indexed packets has more significant improvement after STTC

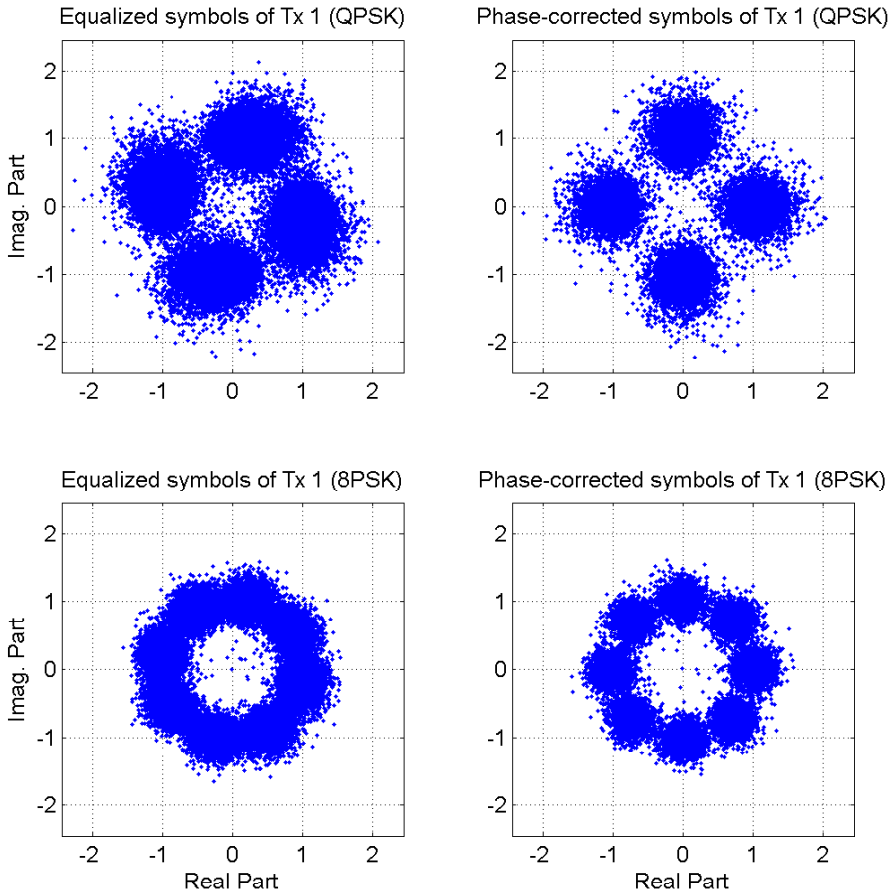

Figure 7.10: Equalized and phase-corrected QPSK and 8PSK symbols

decoding than the odd-indexed packets, due to the use of symbol interleaving.

We finally presented the results for HB transmission. The channel length was measured as $L = 150$ compared to $L = 100$ with LB transmission, due to the smaller symbol interval in this case. The BER results for HB transmission is shown in Table 7.4 with BPSK modulation. The average uncoded BER is on the order of 5×10^{-3}, which is not as good as that of Table 7.1 due to the increased transmission rate.

7.5.2 Results of Unet06 Experiment

SIMO UWA communication experiments with both moving-source transmission and fixed-source transmission were conducted at Saint Margaret's Bay, Nova Scotia, Canada, in May

Table 7.1: BER of LB 2×8 MIMO with BPSK modulation

Packet index	Uncoded BER of Tx 1	Uncoded BER of Tx 2	Uncoded BER of Tx 1&2	BER after STTC decoding
1	2.800e-3	4.178e-3	3.489e-3	2.000e-4
2	4.237e-4	1.695e-4	2.966e-4	0
3	1.556e-3	9.333e-4	1.244e-3	1.111e-4
4	1.316e-4	5.482e-4	3.399e-4	0
5	2.412e-4	1.096e-4	1.695e-4	6.579e-5
6	4.240e-5	1.271e-4	8.475e-5	0
7	8.114e-4	5.044e-4	6.579e-4	6.579e-5
8	1.059e-4	6.360e-5	8.475e-5	0
Mean	7.645e-4	8.294e-4	7.954e-4	5.533e-5

Table 7.2: BER of LB 2×8 MIMO with QPSK modulation

Packet index	Uncoded BER of Tx 1	Uncoded BER of Tx 2	Uncoded BER of Tx 1&2	BER after STTC decoding
1	1.656e-3	1.756e-1	8.863e-2	6.984e-2
2	1.126e-4	1.707e-2	8.592e-3	1.374e-3
3	1.351e-4	1.498e-3	8.164e-4	2.252e-5
Mean	6.346e-4	6.472e-2	3.268e-2	2.375e-2

Table 7.3: BER of LB 2×8 MIMO with 8PSK modulation

Packet index	Uncoded BER of Tx 1	Uncoded BER of Tx 2	Uncoded BER of Tx 1&2	BER after STTC decoding
1	8.213e-3	1.614e-1	8.481e-2	2.508e-2
2	1.669e-2	1.199e-1	6.831e-2	1.265e-2
Mean	1.245e-2	1.407e-1	7.656e-2	1.887e-2

Table 7.4: BER of HB 2×8 MIMO with BPSK modulation

Packet index	Uncoded BER of Tx 1	Uncoded BER of of Tx 2	Uncoded BER of of Tx 1&2	BER after STTC decoding
1	1.190e-4	1.212e-3	6.656e-4	1.082e-4
2	9.740e-5	7.359e-4	4.167e-4	0
3	1.840e-4	1.190e-3	6.872e-4	7.576e-5
4	7.325e-3	7.993e-3	7.659e-3	1.064e-3
5	6.494e-5	1.027e-2	5.168e-3	4.361e-3
6	1.447e-2	2.103e-2	1.775e-2	2.597e-4
Mean	3.710e-3	7.072e-3	5.391e-3	9.781e-4

2006. For moving-source transmission, the transmitter was deployed 21 meters deep in the water and towed at a speed up to 4 knots. The communication distance was ranging from 1 km to 3 km. For fixed-source transmission, the transmitter was suspended in water at 21 meters depth and 44 meters above the sea bottom, and the transmission range was fixed as 3.06 km. The receiver consisted of eight hydrophones arranged unequally on a 1.86-meters vertical array, which was suspended 30 meters deep in the water. QPSK modulation was used with a symbol rate of 4 ksps. The carrier frequency was $f_c = 17$ kHz.

The structure of the transmission packet is depicted in Fig. 7.11. It starts with a LFM

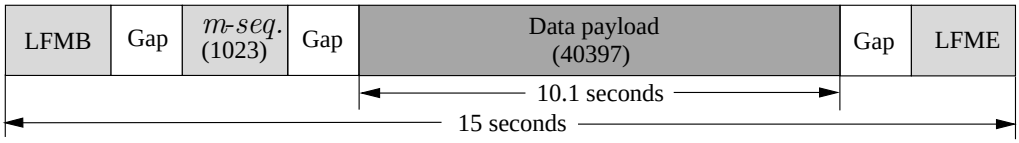

Figure 7.11: SIMO packet structure in Unet06 experiment.

signal named LFMB, and ends with another LFM signal called LFMB. A m-sequence of length 1023 is embedded in the packet, and the data payload carries 40397 symbols. The whole packet has a time duration of 15 seconds.

Without loss of generality, the processing details on moving-source packets are presented. As before, packet synchronization was achieved and the channel length L was estimated, both with the help of LFMB signal. The equivalent symbol-spaced channel length was estimated as $L = 20$ in moving-source transmission. The LFMB signal together with the LFME signal determined the received packet duration, which was used to estimate the average Doppler shift [111]. In Table 7.5, Doppler shift estimations are listed for seven moving-source packets. For each packet, the estimation was performed independently on each of the eight channels (hydrophones). Obviously, the Doppler shift is non-negligible compared to the carrier frequency of 17 kHz. The visual demonstration of the Doppler effect resorts to the channel scattering function, which was estimated with the m-sequence attributing to its sensitivity to Doppler spread. In the left subfigure of Fig. 7.12, the scattering function of the first moving-source packet in Table 7.5 is demonstrated. It is obvious

Table 7.5: Doppler shift estimation in moving-source transmission (Hz)

Channel \ Packet	1	2	3	4	5	6	7
1	15.98	15.71	12.44	10.80	10.79	11.25	8.29
2	15.98	15.71	12.44	10.80	10.79	11.25	8.38
3	15.98	15.71	12.44	10.80	10.79	11.25	8.02
4	15.98	15.71	12.44	10.80	10.79	11.25	8.02
5	15.98	15.71	12.44	10.80	10.79	11.25	8.46
6	16.16	15.71	12.44	10.89	10.79	11.25	8.36
7	15.98	15.71	12.44	10.80	10.79	11.25	8.26
8	15.98	15.71	12.44	10.80	10.79	11.25	8.29

that the Doppler spectrum centers around the average Doppler shift. For comparison, the scattering function for a fixed-source packet is also shown in the right subfigure. Since there is no relative transceiver motion, the Doppler spectrum centers around zero in this scenario. The average Doppler shift was compensated in the moving-source packet before detection started.

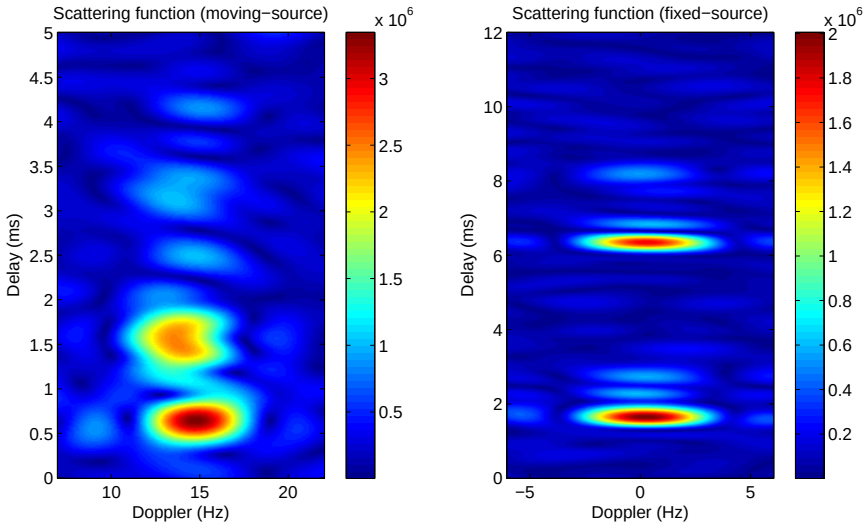

Figure 7.12: Channel scattering functions.

For the channel length of $L = 20$ requiring a minimum training length of 39 with SIMO transmission, a larger training length $N_p = 200$ was selected. This choice of training length corresponds to a time duration of 50 ms, which is less than the channel coherence time about

200 ms for a maximum Doppler spread between $2 \sim 3$ Hz, as shown in Fig. 7.12 (in moving-source case, the Doppler shift demonstrated in the left subfigure will be compensated). The maximum differential phase drift in this case is less than $\frac{\pi}{8}$ and the approximation for phase drift in (7.6) is appropriate. Similar to MIMO case, the received packet was partitioned into blocks for processing with a block size of $N_b = 400$, which is 0.1 seconds of time duration. Only one pilot sequence at the head of the data payload was used to obtain the initial MIMO channel, and the last $N_p = 200$ symbols in the previously-detected block was used to re-estimate the channel, leading to the partition structure shown in Fig. 7.13. In

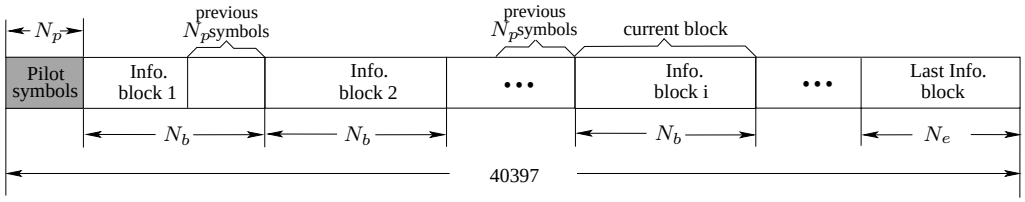

Figure 7.13: Partition of the transmitted data payload for block detection at the receiver.

the group-wise phase estimation and compensation, the group size of $N_s = 40$ was selected, and there were $N_g = 10$ groups in one block.

The scatter plots in Fig. 7.14 and Fig. 7.15 demonstrates the equalized and phase-corrected QPSK symbols for moving-source packet. From Fig. 7.14, the phase rotations in

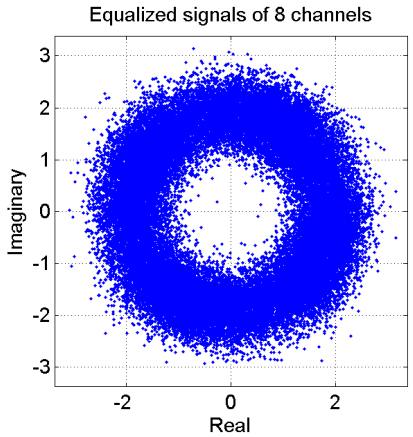

Figure 7.14: Equalized QPSK symbols using eight channels in Unet06 experiment.

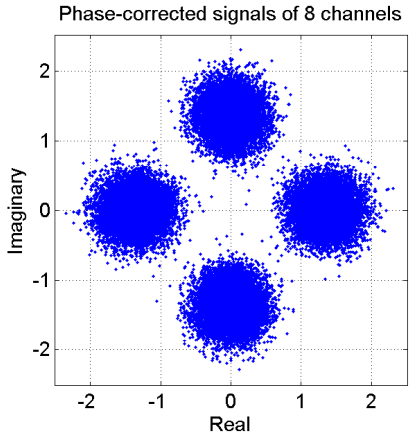

Figure 7.15: Phase-corrected QPSK symbols using eight channels in Unet06 experiment.

Table 7.6: Average uncoded BER for Unet06 experiment

Number of combining channels	Moving Source	Fixed Source
1	3.027e-1	3.135e-1
2	2.778e-1	2.139e-1
3	2.083e-2	1.064e-2
4	1.017e-2	1.740e-3
5	3.455e-3	1.490e-4
6	7.399e-4	1.366e-4
7	7.222e-4	6.621e-5
8	6.248e-4	3.104e-5

the equalized symbols are even more significant compared to the MIMO results shown in Fig. 7.9 and Fig. 7.10. Regardless of the different experimental environments, the reason lies in the adoption of larger block size of $N_b = 400$, compared to $N_b = 200$ used in MIMO case, during detection. The selection of larger block size decreases the complexity for channel adaption, while increases the accumulation of phase rotations in the equalized symbols. From Fig. 7.15, the symbols are well classified after phase correction, which indicates that the adopted phase estimation and compensation algorithm is effective and robust under different channel conditions.

The uncoded BER results for UNet06 experiment are listed in Table 7.6. In total, seven moving-source packets and six fixed-source packets were processed. The processing procedure for fixed-source packets was similar to that of moving-source packet, except that the channel length was $L = 60$ in this case. The listed BERs are averaged ones over all packets. To demonstrate the diversity gain, the results corresponding to different number of combining channels, are all shown. Two observations are made. First, the fixed-source transmission has better uncoded BER performance than the moving-source transmission, due to the absence of Doppler shift in the received signal. Second, it is obvious that the uncoded BER decreases when the number of channels used increases due to the increased diversity gain. When all eight channels are used, the best uncoded BER is achieved for both transmissions.

7.6 Conclusion

We have demonstrated a new time-domain MIMO equalization scheme for high data rate single-carrier underwater acoustic communications, where the separate interference cancelation and phase compensation operations has been performed during detection. MIMO linear equalization was operated in an ordered successive interference cancelation fashion to achieve enhanced performance. A novel group-wise phase estimation and compensation algorithm was used to remove the phase distortion in the equalized symbols. MIMO channel was estimated with pilot symbols in training mode and was tracked using previously-detected symbols in decision-directed mode, incurring no more than 5% training overhead, compared to $20\% \sim 30\%$ in existing receiver designs. The proposed equalization scheme was tested by extensive experimental data measured off the northwestern coast of Kauai, Hawaii, in September 2005, and at Saint Margaret's Bay, Nova Scotia, Canada, in May 2006. Processing results has shown the effectiveness and robustness of the proposed new equalization scheme under different UWA transmission conditions.

Chapter 8

Turbo Detection for MIMO Underwater Acoustic Communications

8.1 Introduction

The advent of turbo decoding [118] and turbo equalization [67] technologies enable powerful receiver design. Compared to non-turbo methods, turbo decoding and equalization significantly improve the detection performance via iterative operations. Turbo equalization for underwater acoustic communications has been first proposed in [119], where a joint maximum *a posteriori* probability (MAP) tubo equalizer and turbo decoder has been adopted for signal detection. The scheme has been tested by experimental data with a symbol rate of 2.5 kilo-symbols per second (ksps), for both BPSK and QPSK modulations. The MAP turbo equalization has a high complexity even using complexity-reducing technology like per-survivor processing (PSP), then a low-complexity turbo decision-feedback equalizer (DFE) has been proposed and tested by a short-range multichannel UWA transmission with 5 kHz channel bandwidth [120]. Turbo DFE has also been studied in [98] recently, for short-range, high carrier frequency, high data rate UWA communications. This design circumvents channel estimation and updates the equalizer taps adaptively for every symbol using least mean square (LMS) algorithm. Turbo DFE for MIMO systems has been proposed in [106], for a multi-band transmission. Turbo equalization using linear equalizer (LE) [72] has also been applied to UWA communications [107], [121] – [124]. In [121], the

turbo LE has been applied to long-range UWA communications, where QPSK modulation has been used with a rate of 4 ksps. In [123], long-term experimental testing with abundant experimental results has been reported to verify the effectiveness of the turbo LE scheme. In [107], turbo LE for MIMO UWA communications has also been proposed, while its application to mobile scenarios is studied in [124].

Block decision-feedback equalizer (BDFE), which provides better equalization performance than its conventional DFE counterpart, has been proposed in [125] for SISO systems. It is especially suitable for communications over fast time-variant channels, where the channel is treated as time invariant only over a short period of transmission block, *i.e.*, the channel is block fading. The turbo versions of BDFE has also been developed in [126] and [127] (also refer to Chapter 6) for SISO and MIMO systems, respectively. In this chapter, the turbo BDFE is applied to MIMO UWA communications, which leads to a robust iterative receiver structure with two unique features. First, with proper cancelation of inter-block interference (IBI), the operation of the turbo BDFE doesn't require a real *block* transmission, so guard intervals among blocks are avoided to achieve high data transmission efficiency. Moreover, the BDFE is operated with overlapped blocks, *i.e.*, the equalized symbols at the tail of previous block is equalized again in the current block. In this way, performance degradation in the equalized symbols at the end of each block is prevented. Second, block-wise channel adaptation has been proposed, using either pilot-aided channel estimation method or decision-directed channel tracking method. Compared to the symbol-wise adaptive channel estimation methods in [106], [123], the fine tuning of adaptive parameters is avoided and robust channel estimation can be obtained under different UWA transmission environments. The proposed receiver design is tested by extensive undersea field trial data collected in the SPACE08 experiment conducted at Martha's Vineyard, Edgartown, MA, in October 2008 and in the GOMEX08 experiment launched at the Gulf of Mexico in July 2008, respectively.

8.2 Transmitter Design and Data Structure

Consider an $N \times M$ MIMO underwater acoustic communication system, with N and M as the number of transmit transducers and receive hydrophones, respectively. At the transmitter side, N bit streams are independently encoded, interleaved, modulated and then transmitted by the N transducers. Fig. 8.1 depicts the signalling on the n-th transmit branch, with $a_{n,k}$, $b_{n,k}$, $c_{n,k}$, and $s_{n,k}$ being the information bit, the encoded bit, the interleaved bit and the modulation symbol, respectively.

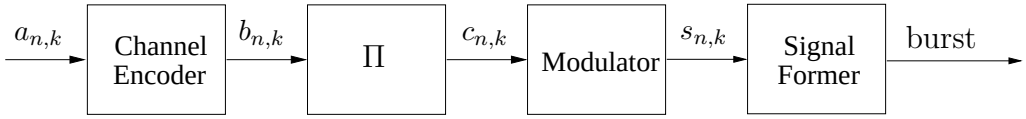

Figure 8.1: Transmit signalling for the n-th transducer.

Convolutional channel encoder and random interleaver (Π) are used throughout this chapter. The modulator employs QPSK, 8PSK and 16QAM modulation schemes, with the constellation sizes being 4, 8 and 16, respectively. For a constellation set $\mathcal{S} = \{\chi_q\}_{q=1}^{Q}$ of size Q, every $\log_2 Q$ coded bits are mapped onto one modulation symbol, *i.e.*, the group of coded bits, $\{c_{n,(k-1)\log_2 Q+p}\}_{p=1}^{\log_2 Q}$, are mapped to the modulation symbol $s_{n,k}$. The signal former unit assembles the input modulation symbols with auxiliary signals, and sends out transmission bursts in specific format. Without loss of generality, a transmission burst of the SPACE08 experiment, is demonstrated in Fig. 8.2. From the figure, the burst begins

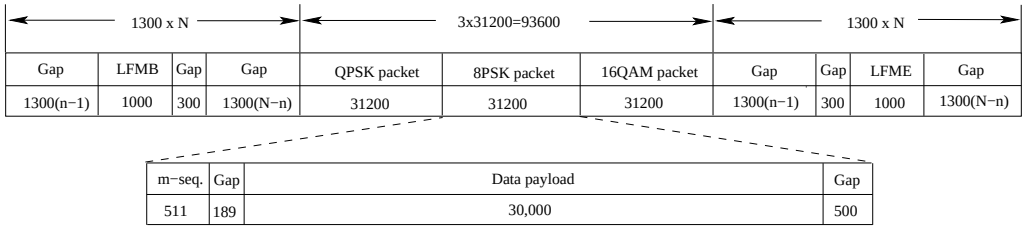

Figure 8.2: The burst structure of the n-th transmit branch in SPACE08 experiment.

with a head linear frequency modulation (LFM) signal named LFMB, followed by three packets with QPSK, 8PSK and 16QAM modulations, and ends with a tail LFM signal named LFME. The LFM signals (LFMB and LFME) serve multiple purposes including

coarse synchronization, Doppler shift estimation and channel length measurement on the receiver side, attributing to their unique correlation properties. Each packet includes a m-sequence of length 511, and a data payload consists of 30,000 modulation symbols. The m-sequence is sensitive to Doppler spread, thus can be used for evaluating the channel scattering function. The structure of the data payload will be evident in the next section. The format of the transmission burst used in GOMEX08 experiment is similar to that shown in Fig. 8.2, except that each burst contains length-variable packets of the same modulation.

8.3 MIMO Receiver Architecture

In UWA communications, front-end preprocessing including synchronization, Doppler shift estimation and compensation, and waveform re-sampling, is usually required before signal detection can be performed [111]. After preprocessing, the discrete-time baseband signal received at the m-th hydrophone is expressed by

$$y_{m,k} = \sum_{n=1}^{N} \sum_{l=0}^{L-1} h_{m,n}(k,l) s_{n,k-l} + v_{m,k} \tag{8.1}$$

where $s_{n,k-l}$ is the transmitted symbol of the n-th transducer, $h_{m,n}(k,l)$ is the l-th coefficient of the subchannel between the n-th transducer and the m-th hydrophone at time k, and $v_{m,k}$ is the zero-mean additive white Gaussian noise (AWGN) sample on the m-th hydrophone with power σ_v^2. For a packet-wise channel encoding, a whole packet of received samples of all M hydrophones, are collected in a vector $\mathbf{y}$ for detection.

Fig. 8.3 depicts the structure of the proposed MIMO receiver, where the soft-decision MIMO BDFE iteratively exchanges soft log-likelihood ratio (LLR) information with N maximum *a posteriori* (MAP) decoders, each corresponding to one transducer, through the interleavers (Π) and the de-interleavers (Π^{-1}). In the current iteration, the MIMO BDFE performs block-wise equalization, and outputs the bit LLRs, $\{\Lambda(c_{n,k})\}_{n=1}^{N}$, for a whole packet, which are further de-multiplexed onto N branches. On the n-th branch, the extrinsic LLR $\Lambda_e(c_{n,k})$ is obtained by subtracting the *a priori* LLR $\Lambda_e^D(c_{n,k})$ (provided by

the n-th MAP decoder in previous iteration) out of $\Lambda(c_{n,k})$. The extrinsic LLR $\Lambda_e(c_{n,k})$ is de-interleaved into $\Lambda_e(b_{n,k})$, which is then delivered to the n-th MAP decoder as its *a priori* LLR input. The LLR feedforward process is represented in the compact mathematical form as $\Lambda_e(b_{n,k}) = \Pi^{-1}\left[\Lambda(c_{n,k}) - \Lambda_e^D(c_{n,k})\right]$. The n-th MAP decoder generates the current LLR $\Lambda^D(b_{n,k})$ using the classic BCJR algorithm [70]. To start the next iteration, the feedback LLR is generated as $\Lambda_e^D(c_{n,k}) = \Pi\left[\Lambda^D(b_{n,k}) - \Lambda_e(b_{n,k})\right]$, similar to the generation of feedforward LLR. The LLRs $\{\Lambda_e^D(c_{n,k})\}_{n=1}^N$ of N branches are finally multiplexed and sent to the MIMO BDFE for the next iteration of equalization. Detection performance is gradually improved over iterations and the final hard decisions $\{\hat{a}_{n,k}\}_{n=1}^N$ are made after convergence.

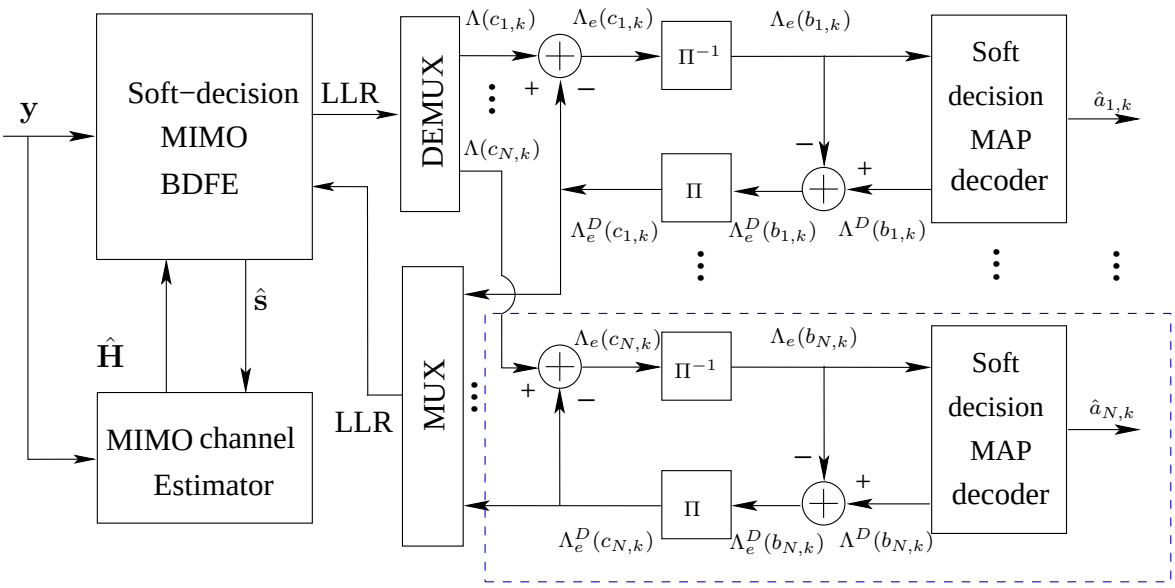

Figure 8.3: MIMO receiver using turbo BDFE.

As shown above, the mechanism of MIMO BDFE requires the received packet to be partitioned into blocks for equalization. A specific partition of the received packet is determined by the structure of the transmitted data payload, as shown in Fig. 8.2. To guarantee signal detection under harsh UWA channel conditions, several features have been introduced in the partition scheme, leading to the partition structure illustrated in Fig. 8.4. First, N_p pilot symbols are inserted periodically for every N_f symbols, where N_f

is properly selected so that tradeoff between the detection performance and the training overhead $\eta = \frac{N_p}{N_f} \times 100\%$ is achieved; Second, to account for the signal-to-noise ratio (SNR) degradation in the equalized symbols at the tail of each block [125], the overlapped block partition is adopted, for which N_{ovlp} symbols at the tail of previous block will be equalized again in the current block; Third, to effectively track the time variation of the channel, N_p previously detected symbols are used to perform decision-directed (DD) channel tracking. The length N_p is selected so that accurate channel estimation or tracking is obtained while the corresponding time duration doesn't exceed the channel coherence time.

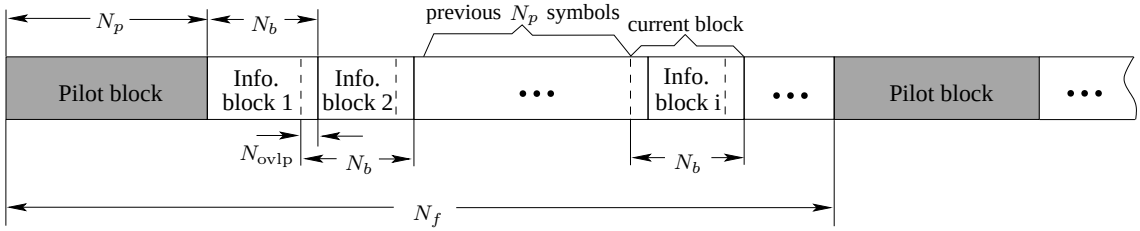

Figure 8.4: The partition structure of the transmitted data payload.

8.4 Experimental Results

The proposed MIMO receiver using turbo BDFE was tested by two undersea trials of UWA communications. The first trial named SPACE08, was conducted at the coast of Martha's Vineyard, Edgartown, MA, in October 2008. The second trial named GOMEX08, was conducted at the Gulf of Mexico, in July 2008.

8.4.1 Results of SPACE08 Experiment

In this experiment, QPSK, 8PSK and 16QAM were used with a symbol interval of 0.1024 milliseconds (ms). The carrier frequency was $f_c = 13$ kHz. The transmit filter was a square-root raised cosine filter with roll-off factor $\beta = 0.2$, thus the occupied channel bandwidth was 11.7188 kHz. The transmitting equipment consisted of four transducers, numbered 0 through 3. Transducer 0 was fixed on a stationary tripod, and was about 4 meters above

the sea bottom. Transducers 1–3 were evenly mounted on a vertical array with the inter-transducer spacing being 50 centimeters (cm). The top transducer in the array was about 3 meters above the sea bottom. The receiving equipment consisted of six sets of hydrophone arrays, which were placed at six different locations. A detailed description about the six hydrophone arrays, is given in Table 8.1. It is noted that for the two cross arrays S1 and S2, each "leg" of the cross consists of 16 hydrophones. The top hydrophone of each array was approximately 3.3 meters (m) above the sea bottom. Finally, the water depth of this experiment was about 15 meters.

Table 8.1: Description on hydrophone arrays

Array Name/Type	Range (m)	Orientation	Number of hydrophones	Hydrophone spacing (cm)
S1/Cross	60	Southeast	16	3.75
S2/Cross	60	Southwest	16	3.75
S3/Vertical	200	Southeast	24	5
S4/Vertical	200	Southwest	24	5
S5/Vertical	1000	Southeast	12	12
S6/Vertical	1000	Southwest	12	12

Fig. 8.5 demonstrates a complete "burst" received at the first hydrophone of array S6 in the top half, with the segment of QPSK packet zoom out in the bottom half. The waveforms contain transmitted signals from two transducers. From the figure, bursty interferences can be observed in the received signal. The power spectrum density (PSD) of the received QPSK packet, is depicted in Fig. 8.6. Obviously, the dynamic range of the PSD is very large (more than 30dB), over the channel bandwidth of about 12 kHz centered at the carrier frequency $f_c = 13$ kHz. This observation verifies the serious frequency-dependent attenuation of UWA channels on received signals. The bursty interference in the time domain and the uneven signal attenuations in the frequency domain, both make the signal detection very challenging.

As mentioned before, coarse synchronization can be achieved by detecting the LFM correlation peaks. The channel length L is estimated by measuring the span of the signif-

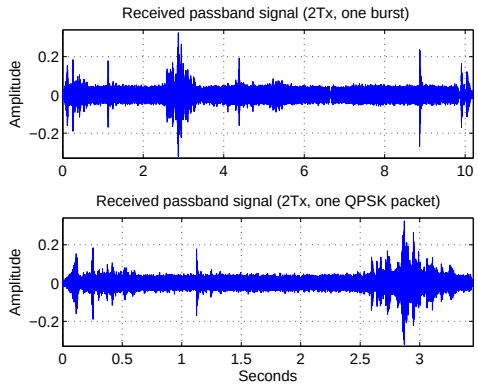

Figure 8.5: An example of received passband signal.

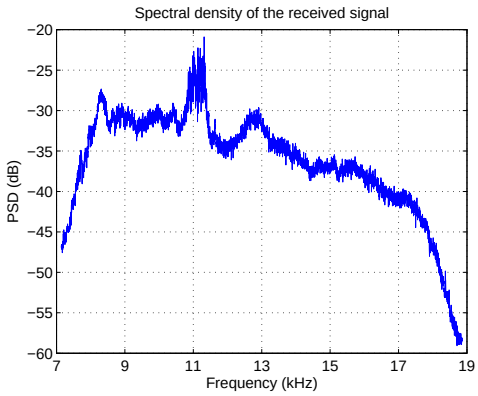

Figure 8.6: Power spectrum density of received signal.

icant LFM correlation [100]. The LFMB signal used in this experiment was a down-chirp with initial and final frequencies being 18 kHz and 8 kHz, respectively. The LFME signal was a up-chirp with reverse initial and final frequencies of LFMB. Either LFMB signal or LFME signal can be used for synchronization. In Fig. 8.7, an example of normalized LFM correlation is demonstrated for a two-transducer 1000 m transmission. It's clearly shown that there are two separate correlation ridges corresponding to the two transducers, and both peaks can be used for coarse synchronization. The first correlation ridge is zoom out in the subfigure, and the time span of the significant correlation is about 10 ms. In other words, most of the channel energy is concentrated within 10 ms corresponding to a channel length of $L \approx 100$ in terms of the symbol interval $T_s = 0.1024$ ms.

The channel estimation example is shown in Fig. 8.8, for a two-transducer 200 m transmission with QPSK modulation. It is shown that the impulse responses (IRs) of the subchannels are sparse and nonhomogeneous, and some are non-minimum phase. The observation verifies the previous claim that UWA channels are very difficult for robust communications.

When synchronization and channel estimation are obtained, signal detection can be performed. The choices of those parameters illustrated in Fig. 8.4 including the block size N_b, the pilot block size N_p, and the block overlapping size N_{ovlp}, are critical for successful detection. An analysis of the channel scattering function obtained with m-sequence, reveals

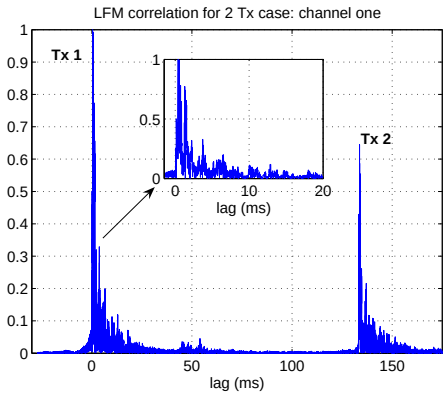

Figure 8.7: LFM correlation example.

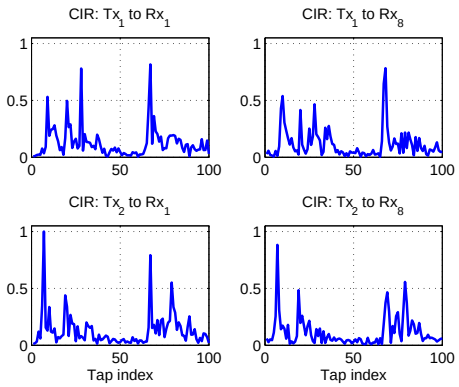

Figure 8.8: Estimated channel.

that the maximum Doppler spread is about 5 Hz corresponding to a channel coherence time about 100 ms. Accordingly, the parameters has been chosen as $N_b = 200$, $N_{\text{ovlp}} = 50$ and $N_p = 600$, during the detection. Such choice of N_b and N_p doesn't violate the time-invariant assumption on the channel. The frame size N_f will be discussed shortly. Before the detection results are listed, the visual demonstrations of the turbo equalization with 8PSK and 16QAM modulations, are first provided in Fig. 8.9 and Fig. 8.10, respectively. In both figures, the soft-decision symbols at the outputs of the equalizer and the MAP decoder, are plotted. It is obvious that the performance is increasingly improved when iterations progress, for both equalizer and decoder. At each iteration, the MAP decoding further improves the equalization performance.

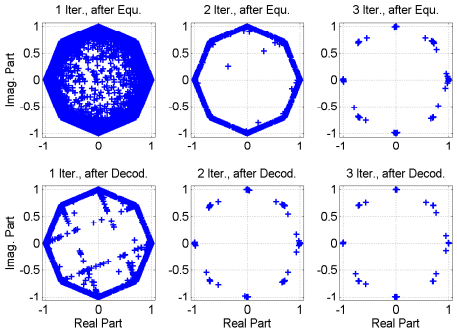

Figure 8.9: Demonstration of turbo equalization over iterations (8PSK modulation)

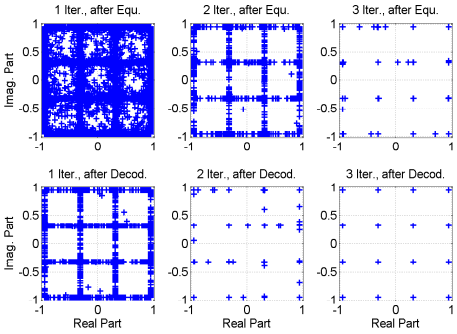

Figure 8.10: Demonstration of turbo equalization over iterations (16QAM modulation)

For 200 m transmission, thirty S3 files and fifteen S4 files recorded in two days, has been

obtained during the SPACE08 experiment. Each file contains four bursts, corresponding to 1×12, 2×12, 3×12 and 4×12 MIMO transmissions. Each burst consists of three packets with QPSK, 8PSK, and 16QAM modulations, as shown in Fig. 8.2. All forty-five 2×12 packets with QPSK and 8PSK modulations, have been processed. For QPSK packets, $N_f = 4500$ has been used, incurring a training overhead of 14%. For 8PSK packets, $N_f = 3000$ leading to a training overhead of 20%, has been applied. The detection results are listed in Table 8.2. From the table, all forty-five QPSK packets have achieved zero bit error rate (BER), requiring no more than four iterations. For 8PSK modulation, twenty-five packets have achieved zero BER within five iterations, and the average BERs for the remaining twenty packets are 7.071×10^{-4} and 7.522×10^{-4}, respectively, for the first transducer and the second transducer.

Table 8.2: Results of 2×12 MIMO (200 m)

Number of iterations to achieve zero BER	Number of packets (QPSK)	Number of packets (8PSK)
1	20	0
2	15	6
3	6	7
4	4	6
5	-	6

For 1000 m transmission, fifteen valid files (five S5 files and ten S6 files) has been recorded. For the remaining nineteen files, four of them has been corrupted by very strong interference and the other fifteen ones have too weak signal to be detected (due to possible transducer malfunction). We have selected $N_f = 3000$ incurring 20% training overhead, for both QPSK and 8PSK modulations. The results are listed in Table 8.3. From the table, all QPSK packets have achieved zero BER, as 200 m transmissions. Five 8PSK packets have achieved zero BER, and the average BERs for the remaining ten 8PSK packets are 1.003×10^{-4} and 1.489×10^{-3}, respectively, for the first and second transducers. Next, an example of detecting 16QAM packet is presented in Table 8.4. Zero BER has been achieved after three iterations. Last, the results for the 3×12 and 4×12 packets with

QPSK modulation, are given in Table 8.5 and Table 8.6. The training overhead are 24% and 34.7%, respectively. In both cases, zero BERs are achieved after three iterations.

Table 8.3: Results of 2×12 MIMO (1000 m)

Number of iterations to achieve zero BER	Number of packets (QPSK)	Number of packets (8PSK)
1	9	0
2	5	2
3	1	3

Table 8.4: BER of 2×12 MIMO (1000 m, 16QAM)

Transducer	Iter. 1	Iter. 2	Iter. 3	Iter. 4
1	1.298e-2	5.556e-5	0	0
2	3.296e-2	4.981e-3	0	0

Table 8.5: BER of 3×12 MIMO (1000 m, QPSK)

Transducer	Iter. 1	Iter. 2	Iter. 3	Iter. 4
1	9.333e-4	0	0	0
2	3.053e-2	2.333e-4	0	0
3	8.927e-2	1.800e-3	0	0

Finally, some interesting results for 60 m transmission are reported. At this communication range, the richest multipath happens compared to the other two ranges, due to the physical geometry. The signal detection is thus the most difficult in this case, in terms of channel conditions. Due to the tough channel condition, a training overhead of 28% with $N_f = 2100$ has been adopted. In Table 8.1, it is shown that cross arrays have been deployed in this scenario, so packets received by horizontal and vertical hydrophone arrays are both available. For convenience, we call the two types of packets as horizontal packet and vertical packet, respectively. From the point view of physics, signal reception using horizontal hydrophone array is extremely difficult, if not impossible, given that the acoustic signals are transmitted from vertical transducer array through horizontal communication

Table 8.6: BER of 4×12 MIMO (1000 m, QPSK)

Transducer	Iter. 1	Iter. 2	Iter. 3	Iter. 4
1	1.318e-3	0	0	0
2	1.600e-2	1.364e-4	0	0
3	6.577e-2	1.455e-3	0	0
4	1.100e-2	0	0	0

channels. However, the proposed turbo equalization still works with horizontal packets, with the BER results listed in Table 8.7. From the table, all three horizontal packets (two S1 packets and one S2 packet) with QPSK modulation, achieve BER in the order of 10^{-4} to 10^{-3}. Compared with horizontal packets, vertical packets are easier for detection. For the five (two S1 packets and three S2 packets) processed vertical packets, four packets have achieved zero BER and the remaining one has obtained a BER in the order of 10^{-4}, with five iterations.

Table 8.7: BER of 2×12 MIMO with horizontal hydrophone array (60 m, QPSK)

Packet	Tx 1	Tx 2
1	4.167e-4	9.259e-4
2	1.852e-4	3.796e-3
3	4.991e-3	4.861e-3

8.4.2 Results of GOMEX08 Experiment

In this experiment, the transmission distance was 1.7 to 2 kilometers (km) and the symbol interval was 0.25 ms. The occupied channel bandwidth is 4.8 kHz, due to the use of a transmit filter with roll-off factor $\beta = 0.2$. The carrier frequency was $f_c = 17$ kHz. The transmitting equipment was a one-meter linear array consisted of four equally-spaced transducers, and was located about 50 m deep in the sea. The receiving equipment was a two-meter linear array consisted of eight unequally spaced hydrophones, and was fixed 50 m deep in the sea. The number of packets in one transmission burst was 48, 24 and 12, corresponding to packet sizes of 1024, 2048 and 4096, respectively.

The channel length was measured as $L = 80$ in this trial, and a block size of $N_b = 150$ was adopted during detection. The overlapping length was selected as $N_{\text{ovlp}} = 40$. An example of the estimated channel is demonstrated in Fig. 8.11. The channel characteristics shown in Fig. 8.8, is again observed in this experiment.

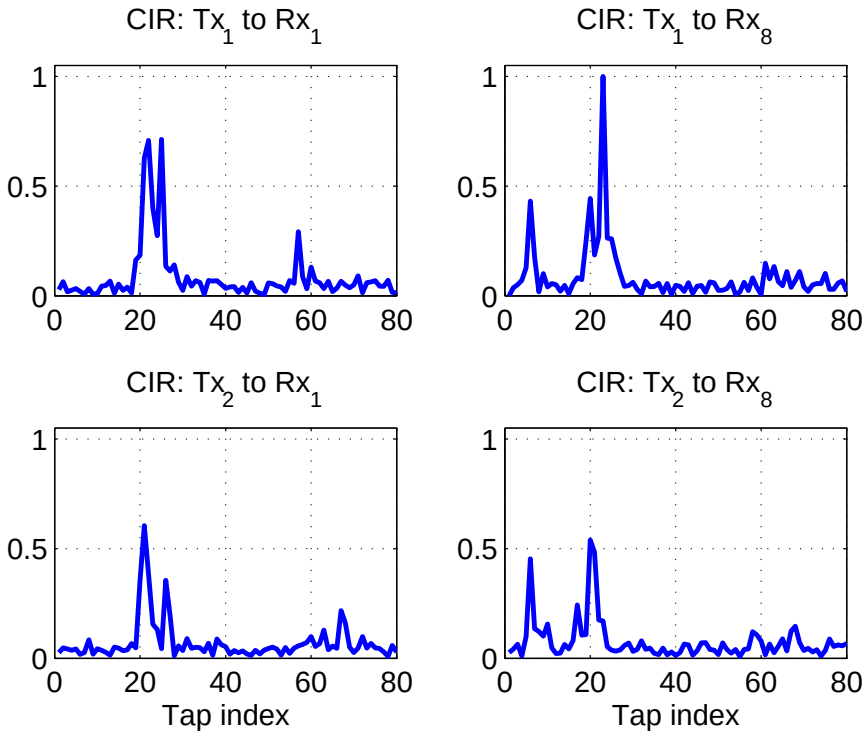

Figure 8.11: Estimated channel impulse responses for GOMEX08 experiment.

The experimental results for 2×8 MIMO transmission with QPSK modulation, are presented. For three bursts with packet size 2048 and three bursts with packet size 4096, the number of turbo iterations for achieving zero BER, are given in Table 8.8 and Table 8.9, respectively. From both tables, most of the packets require no more than three iterations to achieve zero BER. The proposed turbo receiver is thus robust to different transmission environments.

8.4.3 Comparison with Existing Approach

Without loss of generality, we compare the proposed MIMO BDFE with the conventional MIMO DFE, which has been adopted in [106]. Both simulation and experimental com-

Table 8.8: Num. of iter. for achieving zero BER (2×8, QPSK, packet size = 2048)

Pkt idx / Burst idx	1	2	3	4	5	6	7	8	9	10	11	12
1	1	2	1	1	1	1	2	1	1	1	1	1
2	1	1	1	1	1	1	1	1	1	1	3	2
3	1	2	1	1	1	1	1	1	2	3	1	1
Pkt idx / Burst idx	13	14	15	16	17	18	19	20	21	22	23	24
1	1	1	1	1	1	1	1	1	2	1	1	1
2	1	1	1	1	1	4	1	1	1	1	1	2
3	1	1	3	3	1	1	1	1	1	1	1	1

Table 8.9: Num. of iter. for achieving zero BER (2×8, QPSK, packet size = 4096)

Packet index / Burst index	1	2	3	4	5	6	7	8	9	10	11	12
1	4	2	1	1	4	3	1	4	2	1	1	3
2	1	2	3	2	2	1	1	1	3	3	1	2
3	1	1	1	1	2	5	3	2	2	1	2	1

parisons are provided. In the simulation, a 2×4 MIMO system is considered. Each packet carries $N_{\text{pkt}} = 10,000$ information bits, which are encoded by a rate 1/2 non-systematic convolutional encoder with a constraint length 4 and a generator polynomial $[G_1, G_2] = [17, 13]_{\text{oct}}$. After QPSK symbol mapping, the whole packet is divided into blocks of size $N_{\text{sym}} = 100$ for transmission. The eight subchannels are randomly generated and normalized, with a channel length of $L = 20$. The simulation result comparison, is demonstrated in Fig. 8.12. It is obvious that the proposed MIMO BDFE outperforms both conventional MIMO LE and MIMO DFE, and the observation is consistent with that demonstrated in [125] for SISO systems. The experimental result comparison is shown in Fig. 8.13, where the BER with the first iteration of equalization is compared. Obviously, MIMO BDFE consistently produces better BER than MIMO DFE, for the ten 2×12 SPACE08 packets with QPSK modulation.

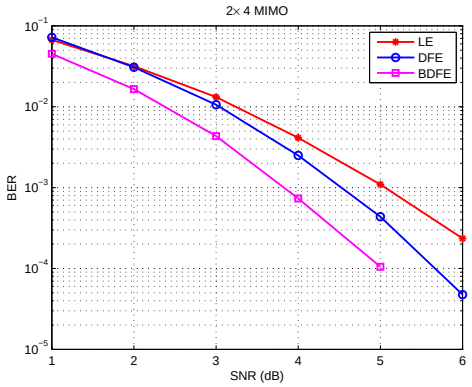

Figure 8.12: Simulation result comparison.

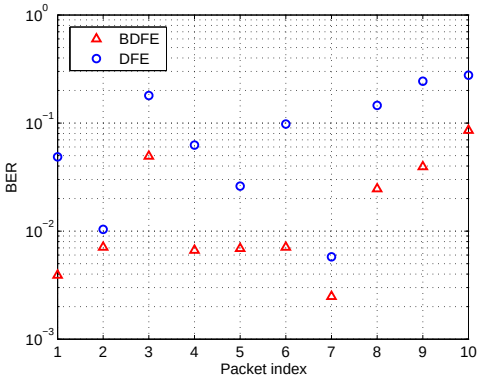

Figure 8.13: Experimental result comparison

8.4.4 Complexity Discussion

The primary design goal for the receiver lies in its robustness, it is also important to consider the detection complexity though. For the proposed receiver scheme, there are two main complexity sources: the MIMO channel estimation, and the calculation of BDFE equalizer matrices.

For both computational sources, the complexity can be considerably reduced by using fewer hydrophones for diversity combining. To demonstrate that, we have reprocessed all forty-five 200 m packets with two transducers and QPSK modulation, using four and six hydrophones for diversity combining, respectively. In each case, two sets of results corresponding to 14% and 20% training overheads, are presented, as shown in Table 8.10. From the table, most packets still require no more than three iterations to achieve zero BER for all four sets of results, as Table 8.2. In this sense, using fewer channels of received signal maintains the same detection performance while reduces the detection complexity dramatically. All fifteen 1000 m packets with two transducers and QPSK modulation, have also been reprocessed using six-hydrophone combining and 20% training overhead as in Table 8.3. The new detection results are listed in Table 8.11. From the table, similar conclusion can be drawn as the 200 m case. Last, the four-transducer packet in Table 8.6 has also been reprocessed with six-hydrophone combining, and the BER results are listed

in Table 8.12. Obviously, the BER performance only degrades slightly in the first two iterations, and zero BER is again achieved after three iterations for all transducers.

Table 8.10: Results for 2×6 and 2×4 MIMO (200 m, QPSK)

Number of iter. to achieve zero BER	# of packets (6 Rx)		# of packets (4 Rx)	
	14% ovhd	20% ovhd	14% ovhd	20% ovhd
1	5	19	0	0
2	30	16	13	31
3	4	4	25	7
4	5	5	6	6
5	1	1	1	1

Table 8.11: Results for 2×6 MIMO (1000 m, QPSK)

Number of iterations to achieve zero BER	Number of packets
1	6
2	6
3	2
4	1

Table 8.12: BER of 4×6 MIMO (1000 m, QPSK)

Transducer	Iter. 1	Iter. 2	Iter. 3	Iter. 4
1	1.773e-3	9.091e-5	0	0
2	2.414e-2	1.864e-3	0	0
3	7.823e-2	8.318e-3	0	0
4	1.627e-2	2.273e-4	0	0

The complexity of the MIMO channel estimation, determined by the channel length L and the frequency of channel adaptation, can also be reduced. A close observation on the estimated channels shown in Figs. 8.8 and 8.11, reveals the sparse property of the channel impulse response, thus the time-varying sparse channel estimation method proposed in [128] can be adopted, incurring a computational complexity of $\mathcal{O}((NL)^2)$. On the other hand, the channel adaptation can be performed for every several consecutive blocks instead of

for every block or every symbol, when the channel coherence time is larger than the block period.

8.5 Conclusion

A new MIMO receiver has been proposed for high data-rate single-carrier underwater acoustic communications. The new scheme has powerful detection capability with high transmission efficiency, attributing to the superior equalization performance and flexible operation of the proposed turbo block decision-feedback equalizer. It is also robust to different UWA channel conditions, in light of the adopted block-wise channel adaptation method. The merits of the proposed scheme have been tested by extensive undersea trial data, measured in two different UWA experiments SPACE08 and GOMEX08. Experimental results for transmission ranges including 60 m, 200 m, 1000 m, and $1.7 \sim 2$ km, are all reported. It has been shown that most of the experimental packets required no more than three iterations of turbo equalization to achieve error-free detection, rendering the proposed MIMO turbo receiver a good candidate in high-performance UWA applications. Moreover, interesting results with vertical-array transducers and horizontal-array hydrophones UWA communications have also been presented to demonstrate its practical feasibility.

Chapter 9

Conclusion

This dissertation focuses on the robust receiver designs for future wireless RF communications and wireless UWA communications. This final chapter summarizes its main contributions and briefly discusses the future works.

9.1 Contribution

Main contributions for wireless RF communications are summarized as follows:

- First, this dissertation points out that the assumption of separability property on equivalent discrete-time channel model is invalid, which has been commonly overlooked in existing literature. The conditions under which the separability property approximately holds, is then provided based on both theoretical analysis and numerical simulations. Separability property enables usage of efficient channel simulators.

- Second, a new Doppler estimation algorithm is proposed for broadband mobile OFDM systems. The new estimator belongs to the class "method of moments" and estimates Doppler spread based on the fourth-order statistics of the received time-domain OFDM signal. Compared to existing Doppler estimation algorithms, which rely either on pilot symbols or special structure of OFDM symbol, the new estimation method can make use of all transmitted data including pilot symbols and unknown information symbols. It provides good performance with low estimation latency even

under very low SNR. It also works with OFDM systems undergoing Rician fading, which to the best of our knowledge, has not been investigated before.

- Third, channel estimation and carrier frequency offset (CFO) estimation for OFDM systems with phase noise is studied. The CFO is estimated utilizing time-frequency property of OFDM symbols, and is then compensated before channel estimation. The channel is jointly estimated in the form of transfer function with the phase noise, using MAP criterion. The frequency-domain channel estimator has much simpler form than time-domain estimator, while maintains the same performance.

- Finally, turbo equalization for MIMO systems is extensively studied. Two MIMO turbo equalization schemes have been proposed. The first scheme enhances existing MIMO LMMSE turbo equalizer by incorporating *a posteriori* information of already equalized symbols into the equalization of remaining symbols yet to be equalized. Under the new equalization framework, the degree-of-freedom of detection order can be utilized. A novel reliability-based detection ordering scheme is proposed to further improve the performance of the new LMMSE equalization method. The second scheme adopts non-linear block decision feedback filter (BDFE), which provides extra gain over linear equalization by relying on successive soft interference cancelation (SSIC). Similar to the enhanced LMMSE equalization, a reliability-based group-wise detection ordering is also proposed for the MIMO BDFE, to minimize the negative effects of error propagation during SSIC.

Main contributions for wireless UWA communications are summarized as follows:

- First, a new time-domain MIMO equalization scheme has been proposed for high data rate single-carrier underwater acoustic communications. The new scheme performs separate interference cancelation and phase compensation operations. MIMO linear equalization was operated in an ordered successive interference cancelation fashion to achieve enhanced performance. A novel group-wise phase estimation and

compensation algorithm was used to remove the phase distortion in the equalized symbols. MIMO channel was estimated with pilot symbols in training mode and was tracked using previously-detected symbols in decision-directed mode, requiring smaller training overhead compared to existing receiver designs. The proposed equalization scheme was tested by extensive experimental data measured off the northwestern coast of Kauai, Hawaii, in September 2005, and at Saint Margaret's Bay, Nova Scotia, Canada, in May 2006.

- Second, a MIMO turbo receiver has been proposed for high data-rate single-carrier underwater acoustic communications. The new scheme has adopted the MIMO turbo BDFE equalization proposed in Chapter 6. The merits of the proposed scheme have been tested by extensive undersea trial data, measured in two different UWA experiments SPACE08 and GOMEX08. Experimental results for different transmission ranges are all reported. The demonstrated good performance of the turbo receiver renders it a good candidate in high-performance UWA applications.

9.2 Future Works

Based on the presented work in this dissertation, new research directions in the future are briefly introduced.

First, parallel to single-carrier systems, turbo equalization for multicarrier OFDM systems will also be investigated, especially for emergent fractional sampling (FS) OFDM systems.

Second, MIMO-OFDM UWA communication will be another research topic worthy of study. Due to the harsh UWA channel conditions, OFDM symbol detection is expected to encounter new challenges.

Appendix A

Proof of (3.8) and (3.9)

The auto-correlation function of the received time domain OFDM signal is calculated as

$$
\begin{aligned}
& R_{yy}(s,u,n,m) = \mathbb{E}\left\{y^{(s)}(n+m)\left[y^{(u)}(n)\right]^*\right\} \\
&= \mathbb{E}\left\{\left[\frac{1}{\sqrt{1+K}}\sum_{l_1=-L_1}^{L_2} h^{(s)}(n+m,l_1)x^{(s)}(n+m-l_1)+\sqrt{\frac{K}{1+K}}h^{(s)}_{LOS}(n+m)\sum_{p_1=-P_1}^{P_2}\sigma_{p_1}x^{(s)}(n+m-p_1)+\right.\right. \\
& \left.\left. v^{(s)}(n+m)\right]\left[\frac{1}{\sqrt{1+K}}\sum_{l_2=-L_1}^{L_2} h^{(u)}(n,l_2)x^{(u)}(n-l_2)+\sqrt{\frac{K}{1+K}}h^{(u)}_{LOS}(n)\sum_{p_2=-P_1}^{P_2}\sigma_{p_2}x^{(u)}(n-p_2)+v^{(u)}(n)\right]^*\right\} \\
&= \frac{1}{1+K}\sum_{l_1=-L_1}^{L_2}\sum_{l_2=-L_1}^{L_2}\mathbb{E}\left\{h^{(s)}(n+m,l_1)\left[h^{(u)}(n,l_2)\right]^* x^{(s)}(n+m-l_1)\left[x^{(u)}(n-l_2)\right]^*\right\}+ \\
& \frac{K}{1+K}\sum_{p_1=-P_1}^{P_2}\sum_{p_2=-P_1}^{P_2}\sigma_{p_1}\sigma^*_{p_2}\mathbb{E}\left\{h^{(s)}_{LOS}(n+m)\left[h^{(u)}_{LOS}(n)\right]^* x^{(s)}(n+m-p_1)\left[x^{(u)}(n-p_2)\right]^*\right\}+ \\
& \mathbb{E}\left\{v^{(s)}(n+m)\left[v^{(u)}(n)\right]^*\right\} \\
&= \left[\frac{1}{N(1+K)}\sum_{l_1=-L_1}^{L_2}\sum_{l_2=-L_1}^{L_2}\sum_{k=0}^{N-1} C_{l_1,l_2}J_0(2\pi f_d m T_s)e^{j\frac{2\pi(l_2-l_1+m)k}{N}}+\right. \\
& \left.\frac{K}{N(1+K)}\sum_{p_1=-P_1}^{P_2}\sum_{p_2=-P_1}^{P_2}\sum_{k=0}^{N-1}\sigma_{p_1}\sigma^*_{p_2}e^{j2\pi f_d m T_s\cos\theta_0}e^{j\frac{2\pi(p_2-p_1+m)k}{N}}+\sigma^2\delta(m)\right]\delta(s-u) \qquad \text{(A.1)}
\end{aligned}
$$

where $x^{(i)}(n)$ defined in (3.1) is used in the derivation of the last equality, thus (3.8) is proved.

The proof of equation (3.9) relies on the two identities: $\mathbb{E}\{v_1v_2v_3\}=0$ and $\mathbb{E}\{v_1v_2v_3v_4\} = \mathbb{E}\{v_1v_2\}\mathbb{E}\{v_3v_4\}+\mathbb{E}\{v_1v_3\}\mathbb{E}\{v_2v_4\}+\mathbb{E}\{v_1v_4\}\mathbb{E}\{v_2v_3\}$, where v_1, v_2, v_3 and v_4 are zero-mean Gaussian random variables. With the identities, (3.9) can be derived based on the definition of auto-covariance function. The details are omitted here for brevity.

Appendix B

Calculation of MIMO LE Matrix

The MIMO LE matrix given in (7.12) has implicit forms which are difficult for evaluation. Therefore, it is desirable to provide explicit solutions directly relating to the channel knowledge. To achieve that, we first represent $\mathbf{y}(k-q)$ of (7.10a) in the following form

$$\mathbf{y}(k-q) = \sum_{l=0}^{L-1} \mathbf{H}(l)\mathbf{x}(k-q-l) + \mathbf{v}(k-q) \tag{B.1}$$

where $\mathbf{x}(k-q-l) = [x_1(k-q-l), \cdots, x_N(k-q-l)]^t$, $\mathbf{v}(k-q) = [v_1(k-q), \cdots, v_M(k-q)]^t$, and

$$\mathbf{H}(l) = \begin{bmatrix} \check{h}_{1,1}(l) & \check{h}_{2,1}(l) & \cdots & \check{h}_{N,1}(l) \\ \check{h}_{1,2}(l) & \check{h}_{2,2}(l) & \cdots & \check{h}_{N,2}(l) \\ \vdots & \vdots & \cdots & \vdots \\ \check{h}_{1,M}(l) & \check{h}_{2,M}(l) & \cdots & \check{h}_{N,M}(l) \end{bmatrix} \tag{B.2}$$

with $\check{h}_{n,m}(l) = h_{n,m}(l)e^{j\phi_{n,m}(I)}$ being the effective channel coefficient combining the fading tap with phase drift. Herein, the index I is determined as $I = \lceil (2k + K_1 - K_2)/2 \rceil$ similar to that in (7.5), and the approximation leading to (7.6) is also used to validate (B.1). Then, we are able to express $\mathbf{y} \in \mathcal{C}^{M(K_1+K_2+1)\times 1}$ in (7.9) as

$$\mathbf{y} = \mathbf{H}\mathbf{x} + \mathbf{v} \tag{B.3}$$

where $\mathbf{H} \in \mathcal{C}^{M(K_1+K_2+1)\times N(K_1+K_2+L)}$ is given in the following

$$\mathbf{H} = \begin{bmatrix} \mathbf{H}(L-1) & \mathbf{H}(L-2) & \cdots & \mathbf{H}(0) & \mathbf{0} & \mathbf{0} & \cdots & \mathbf{0} \\ \mathbf{0} & \mathbf{H}(L-1) & \mathbf{H}(L-2) & \cdots & \mathbf{H}(0) & \mathbf{0} & \cdots & \mathbf{0} \\ \vdots & \vdots & \ddots & \ddots & \ddots & \ddots & \vdots & \vdots \\ \mathbf{0} & \mathbf{0} & \cdots & \mathbf{0} & \mathbf{H}(L-1) & \mathbf{H}(L-2) & \cdots & \mathbf{H}(0) \end{bmatrix} \tag{B.4}$$

and $\mathbf{x} = [\mathbf{x}^t(k-K_2-L+1), \mathbf{x}^t(k-K_2-L+2), \cdots, \mathbf{x}^t(k+K_1)]^t \in \mathcal{C}^{N(K_1+K_2+L)\times 1}$ is a vector containing transmission symbols of all N transducers during the period $[k-K_2-L+1, k+K_1]$, and the noise vector is defined as $\mathbf{v} = [\mathbf{v}^t(k-K_2), \cdots, \mathbf{v}^t(k+K_1)]^t \in \mathcal{C}^{M(K_1+K_2+1)\times 1}$. Now, by substituting $\mathbf{y}$ in (7.12) with (B.3), we obtain

$$\mathbf{C}_{\text{MMSE}} = \mathbb{E}\left[\mathbf{x}(k)\mathbf{x}^h\right]\mathbf{H}^h\left\{\mathbf{H}\mathbb{E}\left[\mathbf{x}\mathbf{x}^h\right]\mathbf{H}^h + \mathbb{E}\left[\mathbf{v}\mathbf{v}^h\right]\right\}^{-1} \tag{B.5}$$

In (B.5), we still need to evaluate $\mathbb{E}\left[\mathbf{x}\mathbf{x}^h\right]$, $\mathbb{E}\left[\mathbf{x}(k)\mathbf{x}^h\right]$. Herein, the assumption that the transmitted symbols are uncorrelated both spatially and temporally, is used. In this case, we have $\mathbb{E}[x_i(k)x_j(l)] = \sigma_x^2\delta(i-j)\delta(k-l)$ with σ_x^2 being the power of transmission symbol $x_n(k)$, and

$$\mathbf{R}_x \triangleq \mathbb{E}\left[\mathbf{x}\mathbf{x}^h\right] = \sigma_x^2\mathbf{I}_{N(K_1+K_2+L)} \in \mathcal{C}^{N(K_1+K_2+L)\times N(K_1+K_2+L)} \tag{B.6a}$$

$$\mathbf{R}^h \triangleq \frac{1}{\sigma_x^2}\mathbb{E}\left[\mathbf{x}(k)\mathbf{x}^h\right] = \left[\begin{array}{ccc} \mathbf{0}_{N\times(K_2+L-1)N} & \mathbf{I}_N & \mathbf{0}_{N\times K_1 N} \end{array}\right] \in \mathcal{C}^{N\times N(K_1+K_2+L)} \tag{B.6b}$$

Defining the SNR β as

$$\beta = \frac{\sigma_x^2}{\sigma_v^2} \tag{B.7}$$

and combining (B.6), we finally express the LE matrix in (B.5) as follows

$$\begin{aligned} \mathbf{C}_{\text{MMSE}} &= \mathbf{R}^h\mathbf{H}^h\left(\mathbf{H}\mathbf{H}^h + \frac{1}{\beta}\mathbf{I}_{M(K_1+K_2+1)}\right)^{-1} \\ &= \mathbf{R}^h\left(\mathbf{H}^h\mathbf{H} + \frac{1}{\beta}\mathbf{I}_{N(K_1+K_2+L)}\right)^{-1}\mathbf{H}^h \end{aligned} \tag{B.8}$$

Bibliography

[1] J. D. Parsons, *The Mobile Radio Propagation Channel*, 2nd Ed., John Wiley & Sons, 2000.

[2] P. A. Bello, "Measurement of random time-variant linear channels," *IEEE Trans. Inform. Theory*, vol.IT-15, pp.469-475, Jul. 1969.

[3] P. A. Bello, "Characterization of randomly time-variant linear channels," *IEEE Trans. Commun. Syst.*, vol.CS-11, pp.360-393, Dec. 1963.

[4] R. H. Clarke, "A statistical theory of mobile-radio reception," *Bell Syst. Tech. J.*, pp.957-1000, Jul.-Aug. 1968.

[5] Y. R. Zheng and C. Xiao, "Improved models for the generation of multiple uncorrelated Rayleigh fading waveforms," *IEEE Commun. Letters*, vol.6, pp.256-258, June 2002.

[6] C. Xiao, Y. R. Zheng and N. C. Beaulieu, " Statistical simulation models for Rayleigh and Rician fading," in *Proc. IEEE ICC'03*, Anchorage, AK, pp.3524-3529, May 2003.

[7] Y. R. Zheng and C. Xiao, "Simulation models with correct statistical properties for Rayleigh fading channels," *IEEE Trans. Commun.*, vol.51, pp.920-928, June 2003.

[8] P. Hoeher, "A statistical discrete-time model for the WSSUS multipath channel," *IEEE Trans. Veh. Technol.*, vol.41, pp.461-468, Nov. 1992.

[9] C. Xiao, J. Wu, S.-Y. Leong, Y. R. Zheng, and K. B. Letaief, "A discrete-time model for triply selective MIMO Rayleigh fading channels," *IEEE Trans. Wireless Commun.*, vol.3, pp.1678-1688, Sept. 2004.

[10] G. Matz and F. Hlawatsch, "Time-frequency transfer function calculus (symbolic calculus) of linear time-varying systems (linear operators) based on a generalized underspread theory," *J. Math. Phys., Special Issue on Wavelet and Time-Freq. Analysis*, vol. 39, no. 8, pp. 40414070, Aug. 1998.

[11] S. Kwon and D. R. Fuhrmann, " Sampling theorems for linear time-varying systems with bandlimited inputs," in *Proc. IEEE ICASSP'99*, Phoenix, AZ, pp.1385-1388, March 1999.

[12] 3GPP TS 25.104, " Base Station (BS) radio transmission and reception (FDD)," V6.3.0, Sept. 2003.

[13] ITU-T Recommendation G.992.1, "Asymmetric digital subscriber line (ADSL) transceivers," June 1999

[14] ETSI, "Digital video broadcasting (DVB): framing structure, channel coding and modulation for digital terrestrial television (ETSI standard EN 300 744)," V1.4.1, Jan. 2001.

[15] IEEE Std 802.11g-2003, "IEEE standard for wireless LAN medium access control (MAC) and physical layer (PHY) specifications," June, 2003

[16] ETSI EN 302 304, "Digital video broadcasting (DVB): transmission system for handheld terminals (DVB-H)," Nov. 2004.

[17] IEEE Std 802.16e-2005, "IEEE standard for local and metropolitan area networks - part 16: air interface for fixed and mobile broadband wireless access systems," Feb. 2006

[18] T. Zahariadis "Trends in the path to 4G," *IEEE Commun. Engineer*, vol.14, pp.12-15, Feb. 2003

[19] R. Prasad, *OFDM for Wireless Communication Systems.* Artech House, 2004

[20] A. Stamoulis, S. N. Diggavi and N. Al-Dhahir "Intercarrier interference in MIMO OFDM," *IEEE Trans. Signal Processing*, vol.50, pp.2451-2464, Oct. 2002.

[21] M. Speth, S. A. Fechtel, G. Fock and H. Meyr "Optimum receiver design for wireless broad-band systems using OFDM - Part I," *IEEE Trans. Commun.*, vol.47, pp.1668-1677, Nov. 1999.

[22] P. Schniter "Low-complexity equalization of OFDM in doubly selective channels," *IEEE Trans. Signal Processing*, vol.52, pp.1002-1011, Apr. 2004.

[23] C. Tepedelenlioglu, A. Abdi, G. Giannakis, and M. Kaveh, "Estimation of Doppler spread and signal strength in mobile communications with applications to handoff and adaptive transmission," *Wireless Commnunication and Mobile Computing*, vol.1, pp.221-242, March 2001.

[24] J. Zhang, Q. Zhang, B. Li, X. Luo, and W. Zhu, "Energy-efficient routing in mobile ad hoc networks: mobility-assisted case," *IEEE Trans. Veh. Technol.*, vol.55, pp.369-379, Jan. 2006.

[25] A. D. Assouma, R. Beaubrun, and S. Piere, "Mobility management in heterogeneous wireless networks," *IEEE J. Selected Areas Commun.*, vol.24, pp.638-648, Mar. 2006.

[26] P. N. Pathirana, A. V. Savhin, and S. Jha, "Location estimation and trajectory prediction for cellular networks with mobile base stations," *IEEE Trans. Veh. Technol.*, vol.53, pp.1903-1913, Nov. 2004.

[27] H. Schober, F. Jondral, R. Stirling-Gallacher and Z. Wang, "Adaptive channel estimation for OFDM based high speed mobile communication systems," in *Proc. IEEE International Conference on 3rd Generation Wireless and Beyond*, San Francisco, USA, Jun. 2001, pp.392-397

[28] R. C. Cannizzaro, P. Banelli and G. Leus "Adaptive channel estimation for OFDM systems with Doppler spread ," in *Proc. IEEE SPAWC'06*, July 2006, pp.1-5

[29] J. Oh and J. M. Cioffi, "Sub-band rate and power control for wireless OFDM systems," in *Proc. IEEE VTC'04*, Sept. 2004, pp.2011-2014

[30] K. B. Song, A. Ekbal, S. T. Chung and J. M. Cioffi, "Adaptive modulation and coding (AMC) for bit-interleaved coded OFDM (BIC-OFDM)," *IEEE Trans. Wireless Commun.*, vol.5, pp.1685-1694, July 2006.

[31] M. D. Austin and G. L. Stuber, "Velocity adaptive handoff algorithms for microcellular systems," *IEEE Trans. Veh. Technol.*, vol.43, pp.549-561, Aug. 1994.

[32] R. Narasimhan and D. C. Cox, "Speed estimation in wireless systems using wavelets," *IEEE Trans. Commun.*, vol.47, pp.1357-1364, Sept. 1999.

[33] C. Xiao, K. D. Mann, and J. C. Olivier, "Mobile speed estimation for TDMA-based hierachical cellular systems," *IEEE Trans. Veh. Technol.*, vol.50, pp.981-991, July 2001.

[34] C. Xiao, "Estimating velocity of bobiles in EDGE systems," in *Proc. IEEE ICC'02*, Apr. 2002, pp.3240-3244.

[35] G. Azemi, B. Senajij, and B. Boashash, "Mobile unit velocity estimation based on the instantaneous frequecny of the received signal," *IEEE Trans. Veh. Technol.*, vol.53, pp.716-724, May 2004.

[36] L. Zhao and J. W. Mark, "Mobile speed estimation based on average fade slope duration," *IEEE Trans. Commun.*, vol.52, pp.2066-2069, Dec. 2004.

[37] G. Park, S. Nam, T. Yu, D. Hong, and C. Kang, "A modified covariance-based mobile velocity estimation method for Rician fading channels," *IEEE Commun. Lett.*, vol.9, pp.706-708, Aug. 2005.

[38] S. Mohanty, "VEPSD: a novel velocity estimation algorithm for next-generation wireless systems," *IEEE Trans. Wireless Commun.*, vol.4, pp.2655-2660, Nov. 2005.

[39] K.E. Baddour and N.C. Beaulieu, "Robust Doppler spread estimation in nonisotropic fading channels," *IEEE Trans. Wireless Commun.*, vol.4, pp.2677-2682, Nov. 2005.

[40] Y. R. Zheng, C. Xiao "Mobile speed estimation for broadband wireless communications," in *Proc. IEEE WCNC'07*, March 2007, pp.2420-2425.

[41] H. Schober and F. Jondral, "Velocity estimation for OFDM based communication systems," in *Proc. IEEE VTC'02*, Sept. 2002, pp.715-718

[42] T. Yucek, R. M. A. Tannious and H. Arslan, "Doppler spread estimation for wireless OFDM systems," in *Proc. IEEE/Sarnoff Symposium on Advances in Wired and Wireless Communication*, Apr. 2005, pp. 233-236

[43] J. Cai, W. Song, and Z. Li "Doppler spread estimation for mobile OFDM systems in Rayleigh fading channels," *IEEE Trans. Consumer Electron.*, vol. 49, pp. 973-977, Nov. 2003

[44] A. Doukas and G. Kalivas, "Doppler spread estimation in frequency selective Rayleigh channels for OFDM systems," in *Proc. 5th International Symposium in Communication Systems, Networks and Digital Signal Processing*, Patras, Greece, July 2006

[45] A. J. Paulraj, R. Nabar, and D. Gore, *Introduction to Space-Time Wireless Communications*, Cambridge Univ. Press, 2003

[46] C. Xiao, Y. R. Zheng, and N. C. Beaulieu, "Novel sum-of-sinusoids simulation models for Rayleigh and Rician fading channels," *IEEE Trans. Wireless Commun.*, vol.5, pp.3667-3679, Dec. 2006.

[47] L. Piazzo and P. Mandarini, "Analysis of phase noise effects in OFDM modems," *IEEE Trans. Commun.*, vol. 50, pp. 1696-1705, Oct. 2002.

[48] P. H. Moose, "A technique for orthogonal frequency division multiplexing frequency offset correction," *IEEE Trans. Commun.*, vol. 42, pp. 2908-2914, July 1994

[49] T. M. Schmidl and D. C. Cox, "Robust frequency and timing synchronization for OFDM," *IEEE Trans. Commun.*, vol. 45, pp. 1613-1621, Dec. 1997

[50] J. J. van de Beek, M. Sandell and P. O. Borjesson, "ML estimation of time and frequency offset in OFDM systems," *IEEE Trans. Signal Processing*, vol. 45, pp. 1800-1805, July 1997

[51] T. Lv, H. Li and J. Chen, "Joint estimation of symbol timing and carrier frequency offset of OFDM signals over fast time-varying multipath channels," *IEEE Trans. Signal Processing*, vol. 53, pp. 4526-4535, Dec. 2005

[52] D. Huang, K. B. Letaief, "Carrier frequency offset estimation for OFDM systems using null subcarriers," *IEEE Trans. Commun.*, vol. 54, pp. 813-823, May 2006

[53] J. Zhu and W. Lee, "Carrier frequency offset estimation for OFDM systems with null subcarriers," *IEEE Trans. Veh. Technol.*, vol. 55, pp. 1677-1690, Sept. 2006

[54] M. S. El-Tanany, Y. Wu and L. Hazy, "Analytical modeling and simulation of phase noise interference in OFDM-based digital television terrestrial broadcasting systems," *IEEE Trans. Broadcasting*, vol. 47, pp. 20-31, March 2001.

[55] S. Wu and Y. Bar-Ness, "A phase noise suppression algorithm for OFDM-based WLANs," *IEEE Commun. Letters*, vol. 6, pp. 535-537, Dec. 2002

[56] S. Wu, P. Liu and Y. Bar-Ness, "Phase noise estimation and mitigation for OFDM systems," *IEEE Trans. Wireless Commun.*, vol. 5, pp. 3616-3625, Dec. 2006

[57] D. D. Lin, Y. Zhao, and T. J. Lim, "OFDM phase noise cancellation via approximate probabilistic inference," in *Proc. IEEE WCNC'05*, Mar. 2005, vol. 1, pp. 27-32

[58] S. Wu and Y. Bar-Ness, "OFDM channel estimation in the presence of frequency offset and phase noise," in *Proc. IEEE ICC'03*, May 2003, vol. 5, pp. 3366-3370

[59] X. Ma, M. Oh, G. B. Giannakis and D. Park, "Hopping pilots for estimation of frequency-offset and multiantenna channels in MIMO-OFDM," *IEEE Trans. Commun.*, vol. 53, pp. 162-172, Jan. 2005

[60] M. Pun, M. Morelli and C. C. J. Kuo, "Maximum-likelihood synchronization and channel estimation for OFDMA uplink transmissions," *IEEE Trans. Commun.*, vol. 54, pp. 726-736, Apr. 2006

[61] D. D. Lin, R. A. Pacheco, T. J. Lim and D. Hatzinakos, "Joint estimation of channel response, frequency offset, and phase noise in OFDM," *IEEE Trans. Signal Processing*, vol. 54, pp. 3542-3554, Sept. 2006

[62] J. R. Barry and E. A. Lee, "Performance of coherent optical receivers," *Proceedings of the IEEE*, vol. 78, pp. 1369-1394, Aug. 1990.

[63] A. Mehrotra, "Noise analysis of phase-locked loops," *IEEE Trans. Circ. Sys.*, vol. 49, pp. 1309-1315, Sept. 2002

[64] S. M. Kay, *Fundamentals of Statistical Signal Processing: Estimation Theory*, Prentice-Hall, 1993

[65] J. Wu, C. Xiao, and K. B. Letaief, "Multiuser channel estimation for CDMA systems over Doubly Selective fading channels," *IEEE Trans. Wireless Commun.*, vol. 4, pp. 1724-1736, July 2005.

[66] O. Edfors, M. Sandell, J. J. van de Beek, S. K. Wilson and P. O. Borjesson, "Analysis of DFT-based channel estimators for OFDM," *Wireless Personal Communications*, 12, pp. 55-70, 2000

[67] C. Douillard, M. Jezequel, C. Berrou, A. Picart, P. Didier, and A. Glavieux, "Iterative correction of intersymbol interference: turbo-equalization," *Eur. Trans. Telecomm.*, vol. 6, pp. 507-511, Sept.-Oct. 1995.

[68] G. Bauch, H. Khorram, and J. Hagenauer, "Iterative equalization and decoding in mobile communications systems," in *Proc. EPMCC'97*, September/October 1997, pp. 307-312

[69] J. Hagenauer and P. Hoher, "A Viterbi algorithm with soft-decision outputs and its applications," in *Proc. Globecom'89*, November 1989, pp. 1680-1686.

[70] L. Bahl, J. Cocke, F. Jelinek, and J. Raviv, "Optimal decoding of linear codes for minimizing symbol error rate," *IEEE Trans. Inform. Theory*, vol. IT-20, pp. 284-287, March 1974.

[71] X. Wang and H. V. Poor, "Iterative (turbo) soft interference cancellation and decoding for coded CDMA," *IEEE Trans. Commun.*, vol. 47, pp. 1046-1061, July 1999.

[72] M. Tuchler, R. Koetter, and A. C. Singer, "Turbo equalization: principles and new results," *IEEE Trans. Commun.* vol. 50, pp. 754-767, May 2002.

[73] M. Tuchler, A. C. Singer, and R. Koetter, "Minimum mean square error equalization using *a priori* information," *IEEE Trans. Sig. Processing*, vol. 50, pp. 673-683, March 2002.

[74] Z. Wu and J. Cioffi, "Low-complexity iterative decoding with decision-aided equalization for magnetic recording channels," *IEEE J. Sel. Areas Commun.*, vol. 19, no. 4, pp. 699-708, April 2001.

[75] C. Laot, A. Glavieux and J. Labat, "Turbo equalization: adaptive equalization and channel decoding jointly optimized," *IEEE J. Sel. Areas Commun.*, vol. 19, no. 9, pp. 1744-1752, Sept. 2001.

[76] C. Laot, R. L. Bidan, and D. Leroux, "Low-complexity MMSE turbo equalization: a possible solution for EDGE," *IEEE Trans. Wireless Commun.*, vol. 4, no. 3, pp. 965-974, May 2005.

[77] T. Abe and T. Matsumoto, "Space-time turbo equalization in frequency selective MIMO channels," *IEEE Trans. Veh. Technol.*, vol. 52, pp. 469-475, May 2003.

[78] T. Abe, S. Tomisato, and T. Matsumoto, "A MIMO turbo equalizer for frequency-selective channels with unknown interference," *IEEE Trans. Veh. Technol.*, vol. 52, pp. 476-482, May 2003.

[79] G. Bauch and N. Al-dhahir, "Reduced-complexity space-time turbo-equalization for frequency-selective MIMO channels," *IEEE Trans. Wireless Commun.*, vol. 1, pp. 819-828, Oct. 2002

[80] P. W. Wolniansky, G. J. Foschini, G. D. Golden, and R. A. Valenzuela, "V-BLAST: an architecture for realizing very high data rates over the rich-scattering wireless channel," in Proc. ISSSE-98, Pisa, Italy, Sept. 29, 1998.

[81] S. W. Kim and K. P. Kim, "Log-likelihood-ratio-based detection ordering in V-BLAST," *IEEE Trans. Commun.*, vol. 54, pp. 302-307, Feb. 2006.

[82] J. G. Proakis and M. Salehi, *Digital Communication*, 5th Ed. Upper Saddle River, NJ: McGraw-Hill, 2008.

[83] S. L. Ariyavisitakful and Y. Li, "Joint coding and decision feedback equalization for broadband wireless channels," *IEEE J. Sel. Areas Commun.*, vol. 16, no. 9, pp. 1670-1678, Dec. 1998.

[84] R. R. Lopes and J. R. Barry, "The soft-feedback equalier for turbo equalization of highly dispersive channels," *IEEE Trans. Commun.*, vol. 54, no. 5, pp. 783-788, May 2006.

[85] J. Wu and Y. R. Zheng, "Low complexity soft-input soft-output block decision feedback equalization," *IEEE J. Sel. Areas Commun.*, vol. 26, pp. 281-289, Feb. 2008.

[86] G. K. Kaleh, "Channel equalization for block transmission systems," *IEEE J. Sel. Areas Commun.*, vol. 13, pp. 110-121, Jan. 1995.

[87] R. Koetter, A.C. Singer, and M. Tuchler, "Turbo equalization," IEEE Signal Processing Mag., vol. 21, no. 1, pp. 67-80, Jan. 2004.

[88] A. Stamoulis, G. B. Giannakis, and A. Scaglione, "Block FIR decision-feedback equalizers for filterbank precoded transmissions with blind channel estimation capabilities," *IEEE Trans. Commun.*, vol. 49, pp. 69-83, Jan. 2001.

[89] N. Al-Dhahir and A. H. Sayed, "The finite-length multi-input multi-output MMSE-DFE," *IEEE Trans. Sig. Processing*, Vol. 48, No. 10, pp. 2921-2936, Oct. 2000

[90] D. B. Kilfoyle and A. B. Baggeroer, "The state of the art in underwater acoustic telemetry," *IEEE J. Ocean. Eng.*, vol. 25, pp. 4-27, Jan. 2000.

[91] D. J. Garrood, "Application of the MFSK acoustical communication system," in *Proc. MTS/IEEE OCEANS conference*, Boston, MA, 1981, pp. 67-71.

[92] M. Stojanovic, J. Catipovic, and J. Proakis, "Adaptive multichannel combining and equalziation for underwater acoustic communications," *J. Acoust. Soc. Amer.*, vol. 94, pp. 1621-1632, Jan. 1993.

[93] D. Rouseff, D. R. Jackson, W. L. J. Fox, C. D. Jones, J. A. Ritcey, and D. R. Dowling, "Underwater acoustic communication by passive-phase conjugation: theory and experimental results," *IEEE J. Ocean Eng.*, vol. 26, pp. 821-831, 2001.

[94] G. F. Edelmann, T. Akal, W. S. Hodgkiss, K. Seongil, W. A. Kuperman, and S. Hee Chun, "An initial demonstration of underwater acoustic communication using time reversal," *IEEE J. Ocean Eng.*, vol. 27, pp. 602-609, 2002.

[95] T. C. Yang, "Differences between passive-phase conjugation and decision-feedback equalizer for underwater acoustic communications," *IEEE J. Ocean Eng.*, vol. 29, no. 2, pp. 472-487, April 2004.

[96] M. Stojanovic, J. Catipovic, and J. Proakis, "Phase-coherent digital communicaitons for underwater acoustic channels," *IEEE J. Ocean Eng.*, vol. 19, pp. 100-111, Jan. 1994.

[97] S. Roy, T. M. Duman, V. McDonald, and J. Proakis, "Enhanced underwater acoustic communication performance using space-time coding and processing," in *Proc. MTS/IEEE OCEANS conference*, 2004.

[98] J. W. Choi, R. J. Drost, A. C. Singer, and J. Preisig, "Iterative multi-channel equalization and decoding for high frequency underwater acoustic communications," in *Proc. 5th IEEE Sensor Array and Multichannel Signal Processing Workshop*, July 2008, pp. 127-130.

[99] T. C. Yang, "Correlation-based decision-feedback equalizer for underwater acoustic communications," *IEEE J. Ocean Eng.*, vol. 30, pp. 865-880, Oct. 2005.

[100] J. Tao, Y. R. Zheng, C. Xiao, T. C. Yang, and W. B. Yang, "Channel estimation, equalization and phase correction for single carrier underwater acoustic communications," in *Proc. MTS/IEEE OCEANS conference*, Kobe, Japan, April 2008, pp. 1-6.

[101] Y. R. Zheng, C. Xiao, T. C. Yang, and W. B. Yang, "Frequency-domain channel estimation and equalization for shallow-water acoustic communications," *Elsevier Journal of Physical Communication*, accepted for publication.

[102] M. Stojanovic, "Low complexity OFDM detector for underwater acoustic channels," in *Proc. MTS/IEEE OCEANS conference*, Sept. 2006, pp. 1-6.

[103] B. Li, S. Zhou, M. Stojanovic, L. Freitag, and P. Willett, "Multicarrier communication over underwater acoustic channels with nonuniform Doppler shifts," *IEEE J. Ocean. Eng.*, vol. 33, no. 2, pp. 198-209, April 2008.

[104] D. B. Kilfoyle, J. C. Preisig, and A. B. Baggeroer, "Spatial modulation expreiments in underwter acoustic channel," *IEEE J. Ocean. Eng.*, vol. 30, pp. 406-415, April 2005.

[105] H. C. Song, P. Roux, W. S. Hodgkiss, W. A. Kuperman, T. Akai, and M. Stevenson, "Multiple-input-multiple-output coherent time reversal communications in a shallow-water acoustic channel," *IEEE J. Ocean. Eng.*, vol. 31, no. 1, pp. 170-187, Jan. 2006.

[106] S. Roy, T. M. Duman, V. McDonald, and J. Proakis, "High rate communication for underwater acoustic channels using multiple transmitters and space-time coding: receiver structures and experimental results," *IEEE J. Ocean. Eng.*, vol. 32, pp. 663-688, July 2007.

[107] M. L. Nordenvaad and T. Oberg, "Iterative reception for acoustic underwater MIMO communications," in *Proc. MTS/IEEE OCEANS conference*, Sept. 2006, pp. 1-6.

[108] J. Zhang, Y. R. Zheng and C. Xiao, "Frequency-domain equalization for single-carrier MIMO underwater acoustic communications," in *Proc. MTS/IEEE OCEANS conference*, Sept. 2008.

[109] B. Li, J. Huang, S. Zhou, K. Ball, M. Stojanovic, L. Freitag, and P. Willett, "MIMO-OFDM for high rate underwater acoustic communications," *IEEE J. Ocean. Eng.*, vol. 34, no. 4, pp. 634-644, Oct. 2009.

[110] C. Xiao and Y. R. Zheng, "Channel equalization and symbol detection for single carrier broadband MIMO systems with multiple carrier frequency offsets" in *Proc. IEEE ICC*, Beijing, China, May 2008, pp. 4316-4320.

[111] B. S. Sharif, J. Neasham, O. R. Hinton, and A. E. Adams, "A computationally efficient Doppler compensation system for underwater acoustic communications," *IEEE J. Ocean Eng.*, vol. 25, pp. 52-61, Jan. 2000.

[112] T. H. Eggen, A. B. Baggeroer, and J. C. Preisig, "Communication over Doppler spread channels – part I: channel and receiver presentation," *IEEE J. Ocean Eng.*, vol. 25, pp. 62-71, Jan. 2000.

[113] G. J. Foschini, "Layered space-time architecture for wireless communication in a fading environment when using multiple antennas," *Bell Labs Technical Journal*, vol. 1, no. 2, pp. 41-59, Autumn 1996.

[114] A. Lozano and C. Papadias, "Layered space-time receivers for frequency-selective wireless channels," *IEEE Trans. on Commun.*, vol. 50, pp. 65-73, Jan. 2002.

[115] P. W. Wolnainsky, G. J. Foschini, G. D. Golden, and R. A. Valenzuela, "V-BLAST: an architecture for achieving very high data rates over the rich-scattering wireless channel," in *Proc. ISSSE'98*, Pisa, Italy, 1998.

[116] V. Tarokh, N. Seshadri, and A. Calderbank, "Space-time codes for high data rate wireless communications: performance criterion and code construction," *IEEE Trans. Info. Theory*, vol. 44, pp. 744-765, March 1998.

[117] M. V. Clark, "Adaptive frequency-domain equalization and diversity combining for broadband wireless communications," *IEEE J. Select. Areas Commun.*, vol. 16, pp. 1385-1395, Oct. 1998.

[118] C. Berrou, A. Glavieux, and P. Thitimajshima, "Near shannon limit error ccorrecting and decoding: turbo codes (1)," in *Proc. IEEE ICC'93*, May 1993.

[119] E. Sozer, J. Proakis, and F. Blackmon, "Iterative equalization and decoding techniques for shallow wateracoustic channels" in *Proc. MTS/IEEE OCEANS Conf.*, Nov. 2001, vol. 4, pp. 2201-2208.

[120] F. Blackmon, E. Sozer, and J. Proakis, "Iterative equalization, decoding, and soft diversity combining for underwater acoustic channels," in *Proc. MTS/IEEE OCEANS Conf.*, Oct. 2002, vol. 4, pp. 2425-2428.

[121] E. Sangfelt, M. L. Nordenvaad, N. Olofsoon, B. Nilsson, P. Walreeb, and T. Oberg, "Underwater commnunication in the Baltic sea using iterative equalization," in *Proc. 2nd International Conference Exhibition on "Underwater Acoustic Measurements: Technologies Results"*, 2006, pp. 617-624.

[122] J. F. Sifferlen, H. C. Song, W. S. Hodgkiss, W. A. Kuperman, and J. M. Stevenson, "An iterative equalization and decoding approach for underwater acoustic communication," *IEEE J. Ocean Eng.*, vol. 33, no. 2, pp. 182-197, April 2008.

[123] R. Otnes, T. H. Eggen, "Underwater acoustic communications: long-term test of turbo equalization in shallow water," *IEEE J. Ocean Eng.*, vol. 33, no. 3, pp. 321-334, July 2008.

[124] J. Tao, Y.R. Zheng, and C. Xiao, "Turbo detection for mobile MIMO underwater acoustic communications," in *Proc. MTS/IEEE OCEANS Conf.*, Sydney, Australia, May 24-27, 2010.

[125] G. K. Kaleh, "Channel equalization for block transmission systems," *IEEE J. Sel. Areas Commun.*, vol. 13, no. 1, pp. 110-121, Jan. 1995.

[126] J. Wu and Y. R. Zheng, "Low complexity soft-input soft-output block decision feedback equalization," *IEEE J. Sel. Areas Commun.*, vol. 26, no. 2, pp. 281-289, Feb. 2008.

[127] J. Tao, J. Wu, and Y. R. Zheng, "Low-complexity turbo block decision feedback equalization for MIMO systems," in *Proc. IEEE ICC'10*, pp. 1-5.

[128] W. Li and J. C. Preisig, "Estimation of rapidly time-varying sparse channels," *IEEE J. Ocean. Eng.*, vol. 32, no. 4, pp. 927-939, Oct. 2007.

VITA

Jun Tao was born on January 28, 1979, in Yancheng, China. He received the B.S. and M.S. degrees both in Electronic Engineering from Southeast University, Nanjing, China, in 2001 and 2004, respectively. He is expecting to receive his Ph.D. degree in Electrical and Computer Engineering from the University of Missouri, Columbia, Missouri in 2010. From 2004 to 2006, he was a system design engineer at the Realsil Microelectronics Inc. (subsidiary of Realtek), Suzhou, China.